Ultrafast charge transfer processes in solution

DISSERTATION

zur Erlangung des akademischen Grades

Dr. rer. nat.
im Fach Chemie

eingereicht an der
Mathematisch-Naturwissenschaftlichen Fakultät I
Humboldt-Universität zu Berlin

von
Dipl.-Chem. Katrin Adamczyk
25.02.1980 in Berlin

Präsident der Humboldt-Universität zu Berlin:
Prof. Dr. Dr. C. Markschies

Dekan der Mathematisch-Naturwissenschaftlichen Fakultät I:
Prof. Dr. L. - H. Schön

Gutachter:
1. Prof. Dr. N. P. Ernsting
2. Dr. E. T. J. Nibbering
3. Prof. Dr. E. Vauthey

eingereicht am: 29.10.2009
Tag der mündlichen Prüfung: 13.04.2010

Aut viam inveniam aut faciam

Abstract

Charge transfer reactions in solution are of fundamental importance in many areas of chemistry and biology. As commonly accepted, electron transfer reaction is regarded as the simplest chemical reaction because of the absence of bond-breaking and bond-forming processes. It plays a key role in biocatalysis and in photosynthesis. On the other hand, neutralisation reactions between Brønsted acids and bases involve proton transfer which is important for other processes as well: for instance the function of enzymes, the transport mechanism in biological membranes and the aforementioned photosynthesis. Research on charge transfer reactions began in the nineteenth century. In the 1950s, the development of concepts started, in order to describe the mechanism on a microscopic level. Based on transition state theory Rudolph A. Marcus proposed a theory which allows a description of electron transfer reactions in such a way as the rate constant could be related to the free energy of reaction. With some modification this theory can be applied to proton transfer reactions as well.

If a charge is transferred from one molecule to another the charge transfer reaction is referred to as intermolecular or bimolecular. The research on the dynamics of fast bimolecular charge transfer reactions in solution is challenging because of the variable distance between the reactants. Consequently, the reaction rate is influenced by their diffusion. A model, which can be traced back to Marian von Smoluchowski, allows to disentangle the intrinsic reaction within an encounter complex from the preceding diffusion of the reactants resulting in the formation of the encounter complex. Considering different encounter complexes/ reactive complexes the application of this model to bimolecular proton transfer reactions yields a reasonable description. In contrast, bimolecular electron transfer reactions can only be described insufficiently. Different explanations are invoked in the literature: first, the electron can be transferred from donor to acceptor over long distances. This leads to a multitude of reactive complexes, within which the reaction proceeds with different characteristic reaction rates. Second, in case excited state products are involved, the free energy of reaction can be smaller than expected. As a result, the obvious relation is shifted relatively to the true relation. Both explanations could neither be proved nor disproved in an experimental way.

Models which are applied to describe reaction dynamics of charge transfer reactions such as the aforementioned Marcus theory assume reactants to be of spherical symmetry. The Smoluchowski model does this as well: the encounter complex is solely characterised by the complex radius. In light of the molecular structure of typical reactants in photoinduced bimolecular charge transfer reactions, which is far from isotropic, such a simplification is inappropriate. An ideal mutual orientation of the reactants leads to a strong interaction and consequently to a fast reaction. This specific mutual orientation depends on the nature of the reaction. A multitude of reactive complexes with different geometries exist in solution.

The motivation of this thesis is to gain an insight into the geometry of molecular reactive complexes and to connect them with the reaction pathways and the corresponding dynamics.

With the appearance of pulsed laser technology, it became possible to follow chemical reactions in real time with ultrafast time resolution. Time-resolved polarisation-sensitive infrared spectroscopy became an important experimental method for studies on ultrafast structural changes because of its chemical specificity and of the possible local nature of vibrational modes.

Electron transfer reaction between two neutral molecules leads to charge separation whereas the back reaction is specified as charge recombination. In the 1990s, a

theory was introduced in order to account for the discrepancy between experimentally observed rate constants for bimolecular charge separation reactions of high exergonicity and rate constants predicted by Marcus theory. Two different kinds of ion pairs as products of charge separation reaction were postulated: "tight" ion pairs display a short and well-defined distance of 3 Å between the ions, whereas the geometry of so-called "loose" ion pairs is controversial. On the one hand, "loose" ion pairs are characterised with a precise distance of 7 - 8 Å between two ions. On the other hand, scientists assume a distribution of different distances between 7 Å and 12 Å. The type of ion pair being formed is strongly correlated to the free energy of charge separation. According to this hypothesis, a threshold value for the free energy of reaction exists. Below that value charge separation leads to the formation of "tight" ion pairs, whereas "loose" ion pairs are generated for a free energy of reaction being larger than the threshold value. So far, no direct proofs for the existence of different kinds of ion pairs have been brought forward.

Experimental results of ultrafast polarisation-sensitive pump-probe-spectroscopy were combined with quantum mechanical calculations to characterise the formed ion pairs with respect of their geometry and dynamics. It could be shown that it is possible to distinguish ion pairs spectroscopically. However, multiple time scales for the formation of "loose" and "tight" ion pairs indicate that a distinction between two kinds of ion pairs with well-defined geometries is a considerable simplification. "Tight" and "loose" ion pairs should rather be regarded as limiting cases, as there is a continuous distribution of different ion pairs between these two limits. In the light of the experimental results, the proposed relation between the nature of the formed ion pair and the free energy of reaction seems questionable. The crucial parameter governing the nature of the ion pairs is the distribution of neutral reaction pairs subsequent to initiation of the reaction. Furthermore, it was possible to gain insight into the mutual spatial arrangement of the ions within "tight" complexes: the planar ions are arranged in a coplanar fashion, hence the molecular planes are parallel to each other. The neutral reaction pairs display the same geometry as the ion pairs which emerge from them upon charge separation. This conclusion can be drawn because charge separation is ultrafast and proceeds faster than the experimental time resolution of 200 fs. Therefore, no change in geometry can occur due to slower processes like rotational and translational diffusion. An ideal coplanar arrangement of the reactants within the reactive complex provides a strong electronic coupling which is of importance for the reaction rate. The slower formation of "loose" ion pairs suggests a suboptimal arrangement. Before charge separation takes place, the reactants have first to diffuse in order to find the mutual orientation that guarantees a sufficiently large electronic coupling. Crucial for the geometry of the reactive complex is that charge separation has to be faster than further diffusion aiming for the optimal geometry. It would be desirable to have a model at hand which describes reaction dynamics considering the structure of molecules and their orientation.

To examine acid-base neutralisation reaction two different bases were chosen to associate with different questions. Protonation of cyanate, OCN^-, in aqueous solution is thought to result in two different products: isocyanic acid, HNCO, and cyanic acid, HOCN. Despite of different acidity constants - cyanic acid is more acidic than isocyanic acid - a transient protonation at the oxygen terminal cannot be safely excluded. The reaction product might lead to conclusion concerning the structure of the reactive complex. Protonation of bicarbonate results into the formation of carbonic acid. Carbonic acid has only been detected as solid existing in ice matrices and in the gas phase, so far. Quantum mechanical calculations revealed that the decomposition of carbonic acid is faster in presence of water. Because of the relevance of carbon dioxide in physiology and geochemistry and because of the

close relation between aqueous chemistry of carbon dioxide and carbonic acid, the question whether carbonic acid exists or not is of fundamental importance.

The proton transfer reaction is initiated by electronic excitation of a photoacid resulting in an increase of its acidity. Transient protonation of bicarbonate allowed the detection of carbonic acid in aqueous solution for the first time. This provided a detailed characterisation of its acid-base-chemistry. Isocyanic acid was detected exclusively in case of the transient protonation of cyanate. For the reactive complexes the following can be concluded: neither cyanate nor bicarbonate form a “tight” complex with the photoacid. In such complex, photoacid and base are directly hydrogen-bonded. This leads to an ultrafast proton transfer on a time scale of less than 150 fs. Other complexes with well-defined geometries such like the “loose” complex which consists of the photoacid and the base bridged by one water molecule, could not be detected as well. This suggests that the encounter complex between photoacid and base, being cyanate or bicarbonate, most likely contains several water solvation shells separating acid and base. The proton transfer reaction proceeds along two reaction paths: on the one hand, the photoacid dissociates and the proton is transferred to solvent, H_2O. After mutual diffusion hydrated proton and base encounter and proton transfer occurs. On the other hand, photoacid and base can directly form an encounter complex in order to transfer the proton. The importance of one proton transfer pathway to another depends on the relative time constants for diffusion and intrinsic reaction within an encounter complex.

Zusammenfassung

Ladungstransferreaktionen in Lösung sind von fundamentaler Bedeutung in vielen Bereichen der Chemie und der Biologie. Die Elektrontransferreaktion wird gemeinhin als die einfachste chemische Reaktion angesehen, da weder Bindungsbrüche noch Bindungsbildungen stattfinden. Sie spielt eine Schlüsselrolle in der Biokatalyse und in der Photosynthese. Neutralisationsreaktionen zwischen Brønsted Säuren und Basen hingegen beruhen auf bimolekularem Protontransfer welcher auch in vielen anderen Prozessen eine Rolle spielt, so beispielsweise in der Funktion von Enzymen und bei Transportmechanismen in biologischen Membranen und ebengenannten Photosystemen. Die Forschung von Ladungstransferreaktionen hat ihren Ursprung im neunzehnten Jahrhundert, wobei die Entwicklung von Konzepten zur mikroskopischen Beschreibung des Mechanismus Mitte des zwanzigsten Jahrhunderts begann. Rudolph A. Marcus stellte eine Theorie zur Beschreibung von Elektrontransferreaktionen auf, die aufbauend auf der Theorie des Übergangszustandes die Geschwindigkeitskonstante in Relation zu der Freien Energie der Reaktion setzt. In abgewandelter Form ist die Theorie auch auf Protontransferreaktionen anwendbar.

Findet die Ladungstransferreaktion zwischen zwei Molekülen statt, so wird von einem intermolekularen oder bimolekularen Ladungstransfer gesprochen. Die Untersuchung der Dynamik schneller bimolekularer Ladungstransferreaktionen in Lösung wird dahingehend erschwert, als dass der Abstand zwischen den Reaktanten variabel ist und somit die Reaktionsgeschwindigkeit von der Diffusion der Reaktanten beeinflußt wird. Ein Modell, das auf Marian von Smoluchowski zurückgeht, ermöglicht es, den intrinsischen Reaktionsschritt innerhalb eines sogenannten “Begegnungskomplexes” von der vorausgehenden Diffusion der Reaktanten und der damit gewährleisteten Bildung des “Begegnungskomplexes” zu trennen. Bimolekulare Protontransferreaktionen können unter Berücksichtigung verschiedener “Begegnungskomplexe” respektive Reaktionskomplexe mit dem Modell adäquat beschrieben werden. Demgegenüber werden bimolekulare Elektrontransferreaktionen nur ungenügend beschrieben. Gründe hierfür werden in der Literatur Verschiedentliche genannt: zum einen kann das Elektron über größere Distanzen vom Donor zum Akzeptor transferriert werden. Das führt zu zahlreichen verschiedenen Reaktionskomplexen, innerhalb derer die Reaktion mit unterschiedlichen Geschwindigkeiten abläuft. Zum anderen kann die angenommene Freie Reaktionsenergie aufgrund der Beteiligung von angeregten Produktzuständen niedriger sein als erwartet und demnach der offenkundige gegenüber dem wahren Zusammenhang verschoben sein. Beide Erklärungen konnten bisher experimentell weder bewiesen noch widerlegt werden.

Modelle, die zur Beschreibung der Reaktionsdynamik von Ladungstransferreaktionen zu Rate gezogen werden wie die erwähnte Marcustheorie, gehen von kugelsymmetrischen Reaktanten aus. Ebenso das Smoluchowski-Modell: der “Begegnungskomplex” wird ausschließlich durch den Komplexradius charakterisiert. Angesichts der molekularen Struktur typischer Reaktanten in photoinduzierten bimolekularen Ladungstransferreaktionen, welche alles andere als isotropisch ist, ist eine solche Vereinfachung unangebracht. Abhängig von der Art der Reaktion gibt es eine optimale Orientierung der Reaktanten zueinander, die zu einer starken Wechselwirkung und folglich zu einer schnellen Reaktion führt. In Lösung liegen die Reaktanten in einer Vielzahl an Reaktionskomplexen mit unterschiedlichsten Geometrien vor.

Die Motivation dieser Arbeit ist es, einen Einblick in die Geometrie von molekularen Reaktionskomplexen zu gewinnen, diese mit den Reaktionspfaden und der damit verbundenen Reaktionsdynamik zu verknüpfen.

Mit dem Aufkommen gepulster Lasertechnologie ist es möglich geworden, chemische Reaktionen in Echtzeit mit ultraschneller Zeitauflösung zu verfolgen. Zeitaufgelöste polarisationsabhängige Infrarotspektroskopie ist wegen ihrer chemischen Spezifität und der möglichen lokalen Natur von Schwingungsmoden eine wertvolle Untersuchungsmethode zur Offenlegung von ultraschnellen Strukturänderungen.

Die Elektrontransferreaktion zwischen zwei ungeladenen Molekülen führt zu einer Ladungstrennung wohingegen die Rückreaktion eine Ladungsrekombination darstellt. In den 90-iger Jahren wurde eine Theorie aufgestellt, die zur Erklärung dient, warum für bimolekulare Ladungstrennungsreaktionen in Lösung mit einer hohen Freien Reaktionsenergie die experimentell gemessenen Geschwindigkeitskonstanten nicht der Marcus-Theorie entsprechen. Zwei Arten von Ionenpaaren als Produkte der Ladungstrennungsreaktion wurden postuliert: "enge" Ionenpaare zeichnen sich durch einen definierten kurzen Abstand von 3 Å zwischen den Ionen aus wohingegen die Geometrie sogenannter "lockerer" Ionenpaare umstritten ist. Zum einen werden "lockere" Ionenpaare mit einem präzisen Abstand von 7 - 8 Å zwischen den Ionen charakterisiert, zum anderen gehen Wissenschaftler von einer Verteilung verschiedener Abstände zwischen 7 Å und 12 Å aus. Die Art des gebildeten Ionenpaares ist eng verbunden mit der Freien Energie der Ladungstransferreaktion. Gemäß der Hypothese gibt es einen Grenzwert für die Freie Reaktionsenergie unterhalb dessen "enge" Ionenpaare und oberhalb dessen "lockere" Ionenpaare gebildet werden. Bisher gibt es für die Existenz verschiedener Ionenpaare keinen direkten Beweis.

Die experimentellen Ergebnisse ultraschneller polarisationsabhängiger Pump-Tast-Spektroskopie wurden mit quantenchemischen Rechnungen kombiniert, um die gebildeten Ionenpaare hinsichtlich ihrer Geometrie und ihrer Bildungs- und Rekombinationsgeschwindigkeiten zu charakterisieren. Es konnte gezeigt werden, dass eine spektroskopische Unterscheidung verschiedener Ionenpaare möglich ist. Allerdings deuten die multiplen Zeitskalen sowohl für die Bildung der "engen" Ionenpaare als auch der "lockeren" Ionenpaare darauf hin, dass eine Unterscheidung in zwei Arten von Ionenpaaren mit wohl-definierter Geometrie eine erhebliche Vereinfachung ist. "Enge" und "lockere" Ionenpaare sind vielmehr als Grenzfälle zu betrachten, zwischen derer eine kontinuierliche Verteilung verschiedener Ionenpaare existiert. Auch lassen die Ergebnisse Zweifel aufkommen, dass die Art des gebildeten Ionenpaares von der Freien Reaktionsenergie abhängt. Vielmehr deuten die experimentellen Resultate darauf hin, dass die Natur der Ionenpaare durch die Verteilung der neutralen Reaktionspaare vor Initiation der Reaktion bestimmt wird. Weiterhin konnte die räumliche Anordnung der Ionen zueinander innerhalb "enger" Paare aufgeklärt werden: es handelt sich um eine koplanare Anordnung, somit liegen die Molekülebenen der Ionen parallel zueinander. Dieselbe geometrische Anordnung besitzen jene reaktiven Komplexe, die durch Ladungstrennung die entsprechenden "engen" Ionenpaare hervorbringen. Dieser Rückschluß kann daher gezogen werden, da die Ladungstrennungsreaktion ultraschnell innerhalb der experimentellen Zeitauflösung von 200 fs vonstatten geht, was eine Veränderung der Geometrie durch langsamere Prozesse wie rotationelle und translationelle Diffusion ausschließt. Eine optimale koplanare Anordnung der Reaktanten innerhalb des reaktiven Komplexes ermöglicht eine starke elektronische Kopplung, die entscheidend ist für die Reaktionsgeschwindigkeit. Die langsamere Bildung von "lockeren" Ionenpaaren deutet auf eine suboptimale Anordnung hin. Bevor die Ladungstrennungsreaktion vonstatten geht, müssen die Reaktanten durch Diffusion eine adäquate Orientierung zueinander finden, die eine ausreichend große elektronische Kopplung gewährleistet. Ausschlaggebend für die Geometrie des reaktiven Komplexes ist, dass die Ladungstrennung schneller ist als die Diffusion hin zu der optimalen Geometrie. Es wäre wünschenswert, die Struktur der Moleküle und ihre Orientierung in Modelle zur Beschreibung der Reaktionsdynamik zu implementieren.

Zur Untersuchung der Säure-Base-Neutralisationsreaktion wurden in Hinblick auf unterschiedliche Fragestellungen zwei verschiedene Basen verwendet. OCN^-, Cyanat, besitzt zwei funktionelle Gruppen, die transient protoniert werden können. Protonierung am Stickstoffende resultiert in Isocyansäure, HNCO, wohingegen Cyansäure, HOCN, entsteht, wenn das Sauerstoffende protoniert wird. Trotz verschiedener Aziditätskonstanten - Cyansäure besitzt eine höhere Azidität verglichen mit Isocyansäure - kann eine transiente Bildung von Cyansäure nicht ausgeschlossen werden. Das Reaktionsprodukt kann Rückschlüsse über die Struktur der reaktiven Komplexe zulassen. Die Protonierung von Hydrogenkarbonat hingegen führt zur Bildung der Kohlensäure, welche bisher lediglich in der Gasphase und als Feststoff in Tieftemperaturmatrizen nachgewiesen werden konnte. Quantenchemische Rechnungen zeigten, dass Kohlensäure durch Anwesenheit von Wasser schneller in Kohlenstoffdioxid und Wasser zerfällt. Aufgrund der Relevanz von Kohlenstoffdioxid in der Physiologie und der Geochemie und dem direkten Zusammenhang zwischen Kohlenstoffdioxid in wäßriger Umgebung und Kohlensäure ist die Frage der Existenz von Kohlensäure von immenser Wichtigkeit.

Initiert wird die Protontransferreaktion durch elektronische Anregung einer Photosäure, welches zu der Erhöhung ihrer Azidität führt. Durch transiente Protonierung von Hydrogenkarbonat konnte erstmalig Kohlensäure in wässriger Lösung nachgewiesen werden. Dies ermöglichte eine detailliertere Charakterisierung ihrer Säure-Base-Chemie. Im Falle der transienten Protonierung von Cyanat konnte ausschließlich Isocyansäure nachgewiesen werden. Zu den reaktiven Komplexen können folgende Aussagen gemacht werden: weder Cyanat noch Hydrogenkarbonat bilden mit der Photosäure einen sogenannten “engen” Komplex, in welchem die Base über eine Wasserstoffbrücke direkt mit der Photosäure verbunden ist. Solche Komplexe führen zu einem ultraschnellen direkten Protontransfer auf einer Zeitskala von weniger als 150 fs. Andere Komplexe mit wohl-definierter Struktur wie beispielsweise dem “lockeren” Komplex mit einem verbrückenden Wassermolekül zwischen Base und Photosäure konnten ebenfalls nicht detektiert werden. Dies deutet darauf hin, dass der “Begegnungskomplex” zwischen Photosäure und Cyanat respektive Hydrogenkarbonat mehrere Wassersolvatationshüllen enthält, die die Photosäure und die Base voneinander trennen. Die Protontransferreaktion verläuft über zwei Reaktionspfade: zum einen kann die Photosäure das Proton an das Lösungsmittel, H_2O, geben. Das solvatisierte Proton und die Base können anschließend nach Diffusion einen “Begegnungskomplex” bilden, innerhalb dessen die Base protoniert wird. Zum anderen können Photosäure und Base durch Diffusion direkt einen “Begegnungskomplex” bilden, um das Proton zu transferrieren. Die Wichtigkeit des einen Reaktionspfades gegenüber des anderen wird von den relativen Zeitkonstanten für Diffusion und für die Reaktion innerhalb des “Begegnungskomplexes” bestimmt.

Acknowledgement
Danksagung

Viele waren an der Forschung, die dieser Doktorarbeit zugrunde liegt, beteiligt. Ich möchte mich deshalb bei all den Menschen ausdrücklich bedanken, die mich die letzten vier Jahre unterstützt haben.

Allen voran möchte ich mich bei Herrn Prof. Dr. Thomas Elsaesser und Dr. Erik T. J. Nibbering bedanken, dass sie es mir ermöglichten, in ihrer Arbeitsgruppe ein ebenso herausforderndes wie interessantes Forschungsgebiet kennenzulernen.

Dr. Erik T. J. Nibbering danke ich außerdem für seine engagierte und manchmal unkonventionelle Betreuung.

Bei Prof. Dr. Nikolaus Ernsting möchte ich mich für seine Bereitschaft bedanken, mich durch das Promotionsverfahren zu geleiten.

Meinen Freunden danke ich für ihre Unterstützung, Rücksichtnahme und Aufmunterung. Allen voran meinen Kommilitonen, Ingo, Ute und Frank, die sich fast täglich die neuesten Geschichten aus dem Applikationslabor anhören mussten. Auch seien Tobias, Annika, Alf, Romy und Wiebke genannt....Dank$^{\infty}$

Ich bedanke mich auch bei zahlreichen Doktoranden und Postdoktoranden für die Zusammenarbeit, die anregenden Diskussionen, die Unterstützung und bei vielen auch für die Freundschaft (in der Reihenfolge wie sie mir in den Sinn kamen): Dr. Nils Huse, Dr. Corneliu-Catalin Neacsu, Dr. Omar Farghaly Mohammed Abdelsaboor, Rene Costard, Mirabelle Prémont-Schwarz, Ming Yang, Łukasz Szyc, Dr. Gianina Gavrila, Dr. Agathe Espagne, Dr. Claus Ropers, Dr. Cynthia Aku-Leh, Marcus Breusing, Dr. Peter Gaal, Dr. Jason R. Dwyer und Dr. Satoshi Ashihara.

Für eine gute und erfolgreiche Zusammenarbeit möchte ich mich bei den Kooperationspartnern bedanken: Prof. Dr. Eric Vauthey, Dr. Bernhard Lang, Dr. Jens Dreyer, Dr. Natalie Banerji, Prof. Dr. Ehud Pines und Dr. Dina Pines.

Der gesamten C1-Gruppe und anderen sei gedankt für die gute Atmosphäre, die netten Gespräche und die technische Unterstützung: Dr. Wolfgang Freyer, Regina Goleschny, Dr. Valeri Kozich, Wolfgang Krüger, Regina Lendt, Hans-Gerd Ludewig, Dr. Frank Noack, Peter Scholze, Brigitte Steinert, Helmut Walz, Dr. Wolfgang Werncke.

Contents

1 Bimolecular charge transfer dynamics

Much research has been devoted to the dynamics of fast bimolecular reactions in solution by both, experimentalists and theoreticians. Intensive studies, in chemical, physical and biological systems, were done on reactions which progresses are influenced by the transport of reactants. Furthermore, investigation of such reactions have included proton [Eigen, 1964] and electron transfer [Kuznetsov and Ulstrup, 1999], ion association-dissociation [Fuoss and Kraus, 1933], excimer formation [Berberan-Santos and Martinho, 1991; Martinho et al., 1992], dynamics of proteins, enzymes, and membranes [Silverman, 2000], and fluorescence quenching [Sikorski et al., 1998; Nemzek and Ware, 1975; Eads et al., 1990; Shannon and Eads, 1995; Nishikawa et al., 1991]. The thesis of this work will contribute to the knowledge that has already been gathered on bimolecular charge transfer dynamics in various solvents. For this purpose femtosecond UV-pump/IR-probe spectroscopy was used to reveal the mechanism of reactions and the microscopic geometries of reactive complexes.

1.1 Introduction

In a bimolecular charge transfer reaction, the charge, electron or proton, is transferred from donor to acceptor molecule. In this case, the word bimolecular indicates an intermolecular chemical exchange process. Intramolecular charge transfer on the other hand takes place within the same molecule. The exchange process occurs amongst one functional group to another. In standard chemistry textbooks, chemical reaction kinetics in solution is described by classical rate equations: the time dependent concentrations of educts and products are often assumed to obey a set of ordinary differential equations with a time independent proportionality factor k, also known as reaction constant or rate constant. Since the distance between reactants of bimolecular reactions is variable, it is widely accepted that the reaction rate might be affected by diffusion of the reactants. General, the rate is determined by two processes: the diffusion of the two reactants to encounter each other and the on-contact reaction. Three different cases can be identified depending on the rate limiting process:

- A bimolecular reaction is called diffusion-controlled when the diffusion of the reactants is much slower than the on-contact reaction.
- On the contrary, a reaction is called reaction-controlled when many collisions between reactants are needed for them in order to react.
- Intermediate cases in which both processes effect the overall reaction rate constant are referred to as diffusion-influenced.

In the first and third case k is time dependent and the term rate coefficient $k(t)$ is more appropriate to use. In the beginning of the reaction, $k(t)$ has its maximum and then, with time, decreases to a steady-state value. This happens due to relaxation of the separating distance distribution between the reactants from its initial to its steady-state value. It is the aim to disentangle those processes and reveal the intrinsic reaction dynamics which are dependent on the reactant's mutual separation and orientation within reactive complexes.

Over 90 years ago, Marian von Smoluchowski proposed the first quantitative description of a diffusion-controlled reaction in order to describe colloidal aggregation [von Smoluchowski, 1917]. It models the non-interacting reactants as symmetric spheres in a dielectric continuum. The reaction proceeds with unit probability and an infinite intrinsic reaction rate constant only upon mutual contact. Peter Debye incorporated the Coulomb potential $U(r)$ into the von Smoluchowski theory. This resulted in the well-known Debye-von Smoluchowski equation (DSE) which is applicable to ionic reactants [Debye, 1942]. Collins and Kimball extended the theory by introducing a finite bimolecular reaction rate upon contact, k_a. This was done to account for the case that both, rate of diffusion and rate of subsequent reaction, would influence the observed rate coefficient [Collins and Kimball, 1949]. With the Smoluchowski-Collins-Kimball (SCK) model it now was possible to derive an exact analytical solution for non-interacting reactants. On the contrary for a known Coulomb potential it is not possible to solve the DSE using the CK boundary condition. In 1989, an analytic approximation for the time dependent rate coefficient was found by Szabo which can be implemented to interpret experimental data [Szabo, 1989].

1.2 The von Smoluchowski theory

Given two reactive species A and B in an inert solvent, the irreversible reaction taking place can be described by two stages: the first one is the mutual approach of A and B to overcome the large separation distance and second the subsequent reaction between A and B at contact distance:

$$\mathrm{A} + \mathrm{B} \underset{k_{-d}}{\overset{k_d}{\rightleftharpoons}} (\mathrm{AB}) \xrightarrow{k_a} \text{Products}, \tag{1.1}$$

k_d and k_{-d} are rate coefficients for the formation and separation of the encounter pair (AB), and k_a is the first-order rate constant for the reaction of (AB) to form the products. Assuming there is a small concentration of encounter pair (AB) and using the steady-state approximation, the overall bimolecular reaction rate coefficient k_r for the formation of products is:

$$k_r = \frac{k_a k_d}{k_a + k_{-d}}. \tag{1.2}$$

Giving the case that the reaction of the encounter pair is fast compared to the diffusive forward and backward processes, the rate of the overall reaction is determined by the rate for the formation of the encounter pair:

$$k_r \approx k_d \qquad (k_a \gg k_{-d}, k_d). \tag{1.3}$$

In contrast, is the reaction rate of the encounter pair slow compared to the separation into A and B, the products are formed at this rate:

$$k_r \approx \frac{k_a k_d}{k_{-d}} \qquad (k_a \ll k_{-d}). \tag{1.4}$$

The von Smoluchowski theory describes diffusion-limited reaction dynamics in solution (1.3). The inert continuum-like solvent contains A and B, one of them - B - will be given in vast excess. A is modeled as a symmetric sphere with a radius of $\sigma \geq R_A + R_B$ (Figure 1.1) and considered to be in a fixed position whereas B diffuses towards A. The irreversible reaction only occurs with an infinite rate constant $k_a(\sigma) = \infty$ at contact distance σ. The analysis of this simple model is based on the first and second law of diffusion defined by Adolf Fick [Fick, 1855]. The disappearance of A and B due to the reaction induces a concentration gradient of B about A. With this concentration gradient it is possible to derive the flux and hence the particle current of B towards A. The reaction rate simply is the current diffusing to encounter each A reactant multiplied by the concentration of A reactants. Fick's first law relates a particle flux, J, through a unit area to the concentration gradient $\partial c/\partial r$:

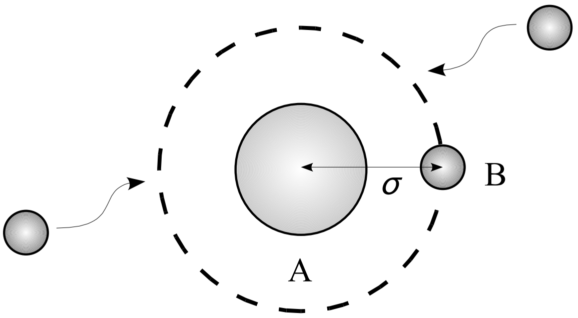

Figure 1.1: Scheme of the so-called target problem for diffusion-limited reactions.

$$J = -D\frac{\partial c}{\partial r}. \tag{1.5}$$

D is the mutual diffusion coefficient, specified in $\mathrm{m^2 s^{-1}}$, and equals to the sum of both reactants, $D = D_\mathrm{A} + D_\mathrm{B}$. It is defined by the Stokes-Einstein equation. D is inversely dependent on the solvent viscosity [Stokes, 1849; Einstein, 1905, 1906]:

$$D = \frac{k_B T}{6\pi\eta a}. \tag{1.6}$$

η is the viscosity of the solvent, specified in $\mathrm{kg{\cdot}m^{-1}s^{-1}}$, and a is the radius of the molecule. The particle current I is the number of particles B arriving per second at the spherical surface of an area of $4\pi\sigma^2$:

$$I(\sigma) = 4\pi\sigma^2 J = -4\pi\sigma^2 D \left|\frac{\partial c}{\partial r}\right|_\sigma. \tag{1.7}$$

To simplify matters, a density distribution of B around A normalised to the initial concentration of reactant B in solution is defined as:

$$\rho(r,t) = \frac{c}{c_0}. \tag{1.8}$$

With this it is possible to extract the rate coefficient:

$$-\frac{d[\mathrm{A}]}{dt} = -\frac{d[\mathrm{B}]}{dt} = k_r[\mathrm{A}][\mathrm{B}]_0 = I(\sigma)[\mathrm{A}]. \tag{1.9}$$

Now, the derivative of the density distribution, with respect to distance, has to be evaluated. The equation of diffusion, also referred to as Fick's second law, can be solved in order to find the expression for $\rho(r,t)$. This equation relates the temporal variation in concentration at a certain position to the spatial variation in concentration at this position:

$$\frac{\partial \rho(r,t)}{\partial t} = D\left[\frac{\partial^2 \rho(r,t)}{\partial r^2} + \frac{2}{r}\frac{\partial \rho(r,t)}{\partial r}\right]. \tag{1.10}$$

Laplace transformation can be used to solve this partial differential equation taking into account the initial conditions:

$$\rho(r,0) = 0 \quad (r \leq \sigma) \tag{1.11}$$

$$= 1 \quad (r > \sigma), \tag{1.12}$$

as well as the condition of inner and outer boundary conditions:

$$\rho(\sigma,t) = 0 \quad (t \geq 0) \tag{1.13}$$

$$\rho(r \to \infty, t) = 1 \quad (t \geq 0). \tag{1.14}$$

This leads to a density distribution given by:

$$\rho(r,t) = 1 - \frac{\sigma}{r}\ erfc\left(\frac{r-\sigma}{\sqrt{4Dt}}\right) \quad \text{with} \quad erfc(x) = \frac{2}{\sqrt{\pi}}\int_x^\infty e^{-z^2}dz, \tag{1.15}$$

in which the function $erfc(x)$ is the complementary error function of argument x. Its limiting values are:

$$erfc(0) = 1 \tag{1.16}$$

$$erfc(\infty) = 0. \tag{1.17}$$

Calculating the derivative of $\rho(r,t)$, in respect of the distance gives:

$$\frac{\partial\rho(r,t)}{\partial r} = \frac{\sigma}{r}\left\{\frac{1}{r} - \frac{1}{r}\ erfc\left(\frac{r-\sigma}{\sqrt{4Dt}}\right)\right.$$

$$\left. + \frac{1}{\sqrt{\pi Dt}}\left(1-\sigma-\frac{(r-\sigma)^2}{2Dt}\right)\ \exp\left(-\left(\frac{r-\sigma}{\sqrt{4Dt}}\right)^2\right)\right\} \tag{1.18}$$

which results into the well-known von Smoluchowski rate coefficient for diffusion-limited reactions:

$$k_r(t) = -4\pi\sigma^2 D\left|\frac{\partial\rho}{\partial r}\right|_{\sigma} = 4\pi\sigma D\left[1+\frac{\sigma}{\sqrt{\pi Dt}}\right]. \tag{1.19}$$

The time-dependence of this rate coefficient is shown in Figure 1.2. In early stages of the reaction a high reaction rate coefficient can be seen due to the density of reactants B in the immediate vicinity of A. As the reaction proceeds the fraction of on-contact pairs have already reacted that reaction can only occur between A molecules which do not have a B molecule nearby. This causes larger diffusion distances for B in order to react. The longer diffusion time is reflected by the decrease of the reaction rate coefficient. During long times ($\geq$ 10 ns) a constant density distribution of reactant B is formed:

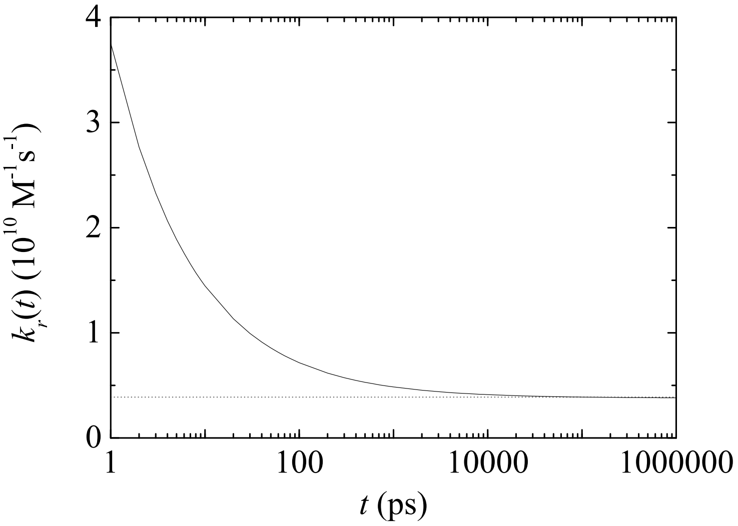

Figure 1.2: The von Smoluchowski rate coefficient for diffusion-limited reaction with the mutual diffusion coefficient $D = 10^{-9}$ m^{2}s^{-1} and a contact distance of $\sigma = 0.5$ nm.

$$\rho(r,\infty) = 1 - \frac{\sigma}{r}. \tag{1.20}$$

Thereby the rate coefficient becomes time-independent and corresponds to the steady-state diffusion rate constant:

$$k_r(\infty) \equiv k_d = 4\pi\sigma D. \tag{1.21}$$

It is important to be aware of the following assumptions of this model:

- The reactants are symmetric spheres.
- The solvent is a dielectric continuum.
- There is no interaction between particles of the same kind.
- The reaction occurs only at one specific contact distance.
- The probability of reaction at contact distance is 1.
- The reaction rate is infinitely high.

Collins-Kimball model

Is the actual reaction comparable or slower than the formation of the encounter pairs by diffusion, it will be unjustified to assume that the reactants can not co-exist within contact distance. A way to overcome this restriction is to replace the inner boundary condition (1.13) by the partially reflecting boundary condition introduced by Collins and Kimball in 1949 [Collins and Kimball, 1949]:

$$k_a \rho(\sigma) = 4\pi\sigma^2 D \left|\frac{\partial\rho}{\partial r}\right|_{\sigma}. \tag{1.22}$$

$\rho(\sigma)$ is the probability that the encounter pair exists. k_a is the second-order rate constant for the reaction of A and B when they are in contact distance σ. As the encounter pair concentration rapidly reaches a steady-state value, the rate of formation and rate of reaction of the encounter pairs may be equated with each other.
In this model the density distribution is given by:

$$\rho(r,t) = 1 - \frac{\sigma}{r}\frac{k_a}{k_a+k_d}\Bigg\{erfc\left(\frac{r-\sigma}{\sqrt{4Dt}}\right) - \exp\left[\frac{(k_a+k_d)(r-\sigma)}{4\pi\sigma^2 D}\right]$$

$$\cdot \exp\left[\frac{(k_a+k_d)^2 t}{(4\pi\sigma^2)^2 D}\right] \cdot erfc\left(\frac{k_a+k_d}{4\pi\sigma^2\sqrt{D/t}} + \frac{r-\sigma}{\sqrt{4Dt}}\right)\Bigg\}. \tag{1.23}$$

Inserting the derivative of the density distribution in respect of the distance in (1.22) leads to the reaction rate coefficient:

$$k_r(t) = k_a\rho(\sigma) = \frac{k_a k_d}{k_a+k_d}\Bigg\{1 + \frac{k_a}{k_d}\exp\left[\frac{Dt}{\sigma^2}\left(1+\frac{k_a}{k_d}\right)^2\right]$$

$$\cdot erfc\left(\frac{\sqrt{Dt}}{\sigma}\left(1+\frac{k_a}{k_d}\right)\right)\Bigg\}. \tag{1.24}$$

With the useful series expansion:

$$e^{x^2} erfc x = \frac{1}{x\sqrt{\pi}} \left(1 - \frac{1}{2x^2} + \frac{3}{4x^4} - ...\right), \tag{1.25}$$

this expression can be simplified to:

$$k_r(t) = \frac{k_a k_d}{k_a + k_d} \left\{ 1 + \frac{k_a}{k_a + k_d} \frac{\sigma}{\sqrt{\pi D t}} \right\}. \tag{1.26}$$

When the contact distance σ in (1.26) is replaced by an effective contact distance:

$$\sigma_{eff} = \sigma \frac{k_a}{k_a + k_d}, \tag{1.27}$$

the reaction rate coefficient becomes:

$$k_r(t) = 4\pi \sigma_{eff} D \left[1 + \frac{\sigma_{eff}}{\sqrt{\pi D t}} \right], \tag{1.28}$$

which is the same as the von Smoluchowski rate coefficient. The incorporation of a finite reaction rate constant into the von Smoluchowski model for diffusion-limited reactions reduces the effective contact distance by a factor of $k_a/(k_d + k_a)$ for the steady-state, as well as the transient term in the rate coefficient.
In Figure 1.3 the von Smoluchowski rate coefficient is shown as dots in comparison to the rate coefficients calculated by using the Collins-Kimball expression (1.26) and three

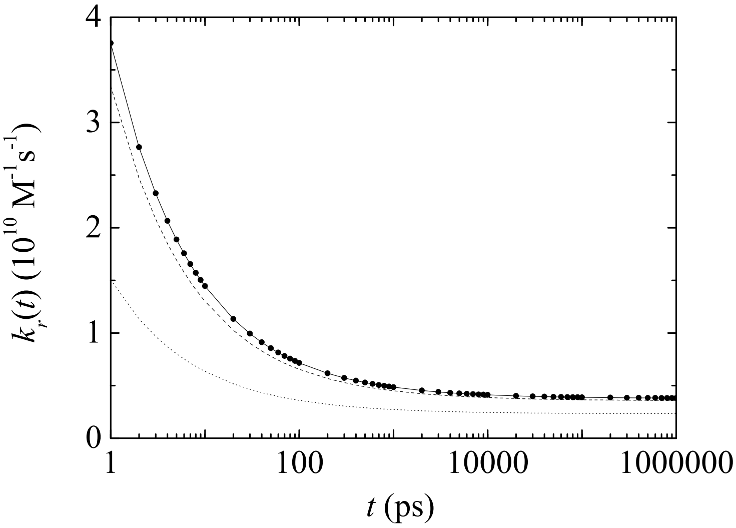

Figure 1.3: The rate coefficient using the partially reflecting boundary condition with $k_a = 10^{-14}$ m^{3}s^{-1} (solid line), $k_a = 10^{-16}$ m^{3}s^{-1}(dashed line) and $k_a = 10^{-17}$ m^{3}s^{-1}(dotted line) compared to the von Smoluchowski rate coefficient for diffusion-limited reaction (dots), ($D = 10^{-9}$ m^{2}s^{-1}, $\sigma = 0.5$ nm).

different values for the reaction rate constant, k_a, at contact distance σ. Obviously, the importance of diffusion on the overall reaction rate decreases when the reaction of the encounter pair becomes slow. Only if $k_a > k_d$ or $k_a \approx k_d$, the overall reaction rate is affected by the rate of the diffusion process. For $k_a \gg k_d$ the Collins-Kimball expression reduces to the Smoluchowski rate coefficient.

At long times the overall time to react is the sum of the time for A and B to diffuse to each other, k_d^{-1}, and then react, k_a^{-1} [Noyes, 1961; Rice, 1985]:

$$\frac{1}{k_r(\infty)} = \frac{1}{k_a} + \frac{1}{k_d}. \tag{1.29}$$

Incorporation of a screened Coulomb potential

The two models, that have been presented so far, describe reaction dynamics between spherical particles diffusing in a dielectric continuum with no forces amongst them. In electrolyte solutions the Coulomb interaction cannot be neglected. Due to Coulomb attraction between oppositely charged ions a crystal-like short-range order is formed. Positively charged ions have a tendency towards an arrangement with spherical symmetry around negatively charged ions and *vice versa*. The thermal motions of the ions counteract against this order. Under thermal equilibrium the ion distribution can be described with Boltzmann statistics. The knowledge of both the ion density and the electrical potential is crucial for the derivation of the reaction rate coefficient between ions. In 1923, Peter Debye and Erich Hückel presented a theory which allows the calculation of the electrical potential at a point in a dilute electrolyte solution in terms of the concentrations and charges of the ions and the properties of the solvent [Debye and Hückel, 1923; Robinson and Stokes, 1959]. It is possible to determine the electrical potential ϕ from the known charge density ρ using the Poisson equation:

$$\nabla^2 \phi = -\frac{4\pi}{\varepsilon}\,\rho, \tag{1.30}$$

where ε is the static dielectric constant of the solvent. In the present case where the distribution of charges possess spherical symmetry at the origin, the electrical potential ϕ depends only on the distance r from the origin. The partial differential operator ∇^2 then reduces to a total differential operator and (1.30) takes the form:

$$\frac{1}{r^2}\frac{\partial}{\partial r}\left(r^2 \frac{\partial \phi}{\partial r}\right) = -\frac{4\pi}{\varepsilon}\,\rho. \tag{1.31}$$

The total charge density is the sum of the charge densities of all constituents:

$$\rho(r) = \sum_i z_i \cdot \mathrm{e} \cdot n_i(r) \tag{1.32}$$

with the number density n_i of constituent i, the elementary charge e and the charge number z_i of constituent i. As already mentioned it is possible to relate the number densities $n_i(r)$ of the constituents at a point to the overall averaged number densities

n_i^0 using the Boltzmann distribution:

$$n_i(r) = n_i^0 \cdot exp\left(-\frac{z_i \cdot \mathrm{e} \cdot \phi(r)}{k_B T}\right), \tag{1.33}$$

where k_B is the Boltzmann constant and T is the absolute temperature. For the charge density, it follows:

$$\rho(r) = \sum_i z_i \cdot \mathrm{e} \cdot n_i^0 \cdot exp\left(-\frac{z_i \cdot \mathrm{e} \cdot \phi(r)}{k_B T}\right). \tag{1.34}$$

For dilute electrolyte solutions the potential energy between the ions is much weaker than the average thermal energy $z_i e \phi(r) \ll k_B T$. Therefore we can use the series expansion and truncate after the second term $e^{-x} \approx 1 - x$ leading to:

$$\rho(r) = -\frac{\mathrm{e}^2 \cdot \phi(r)}{k_B T} \sum_i z_i^2 \cdot n_i^0, \tag{1.35}$$

taking into account that the solution as a whole is electrically neutral:

$$\sum_i z_i \cdot n_i^0 = 0. \tag{1.36}$$

Using the relation $n_i(r) = N_A \cdot c_i(r)$ (N_A is Avogadro's number) and introducing the ionic strength:

$$I = \frac{1}{2} \sum_i z_i^2 \cdot c_i, \tag{1.37}$$

the charge density takes the form:

$$\rho(r) = -\frac{2 N_A \mathrm{e}^2 I}{k_B T}\, \phi(r). \tag{1.38}$$

The general solution of the differential equation:

$$\frac{1}{r^2}\frac{\partial}{\partial r}\left(r^2 \frac{\partial \phi}{\partial r}\right) = \kappa^2 \phi(r) \quad \text{with} \quad \kappa = \sqrt{\frac{8\pi N_A \mathrm{e}^2 I}{\varepsilon\, k_B T}}, \tag{1.39}$$

becomes:

$$\phi(r) = \frac{A}{r}\, e^{-\kappa r} + \frac{B}{r}\, e^{\kappa r}. \tag{1.40}$$

Taking into account the boundary conditions:

$$\lim_{r \to \infty} \phi(r) = 0 \tag{1.41}$$

$$\int_a^\infty 4\pi r^2 \rho dr = -z_j\, \mathrm{e} \tag{1.42}$$

the potential can be written as:

$$\phi(r) = \frac{z_j \, \mathrm{e}}{\varepsilon r} \frac{e^{-\kappa(r-a)}}{1+\kappa a}, \tag{1.43}$$

with a as the radius of the central ion. κ^{-1} is denoted as the Debye length and indicates to what extent the electrical potential of the central ion is screened by the surrounding counterions. With a given potential between two ionic reactants:

$$U(r) = \frac{z_1 z_2 \, \mathrm{e}^2}{\varepsilon r} \frac{e^{-\kappa(r-a)}}{1+\kappa a}, \tag{1.44}$$

it is possible to derive the time-dependent second order rate coefficient $k_r(t)$ using the analytic approximation to the Debye-Smoluchowski-equation:

$$\frac{\partial \rho(r,t)}{\partial t} = \frac{D}{r^2} \frac{\partial}{\partial r} r^2 e^{-\beta U(r)} \frac{\partial}{\partial r} e^{\beta U(r)} \rho(r,t) \tag{1.45}$$

calculated by Szabo [Szabo, 1989] based on the partially reflecting boundary condition and assuming an initial Boltzmann distribution:

$$k_r(t) = \frac{k_d k_a e^{-\beta U(\sigma)}}{k_d + k_a e^{-\beta U(\sigma)}} \left\{ 1 + \frac{k_a e^{-\beta U(\sigma)}}{k_d} \exp\left[\frac{Dt}{\sigma_e^2} \left(1 + \frac{k_a e^{-\beta U(\sigma)}}{k_d} \right)^2 \right] \right.$$
$$\left. \cdot \, erfc \left(\frac{\sqrt{Dt}}{\sigma_e} \left(1 + \frac{k_a e^{-\beta U(\sigma)}}{k_d} \right) \right) \right\} \tag{1.46}$$

with $\beta = 1/k_B T$ and the steady-state diffusion rate constant $k_d = 4\pi D \sigma_e$. The effective radius σ_e is defined as:

$$\frac{1}{\sigma_e} = \int_0^\infty e^{\beta U(\sigma)} r^{-2} dr. \tag{1.47}$$

The first term in (1.46) determines the asymptotic value reached at long times, which presents the steady-state reaction rate constant:

$$k_r(\infty) = \frac{k_d k_a e^{-\beta U(\sigma)}}{k_d + k_a e^{-\beta U(\sigma)}}, \tag{1.48}$$

and the second term describes the transient value of the rate coefficient. Both terms represent bimolecular rate constants.

After this brief presentation of the Debye-von Smoluchowski theory, it is the objective of the following two sections to show if the SCK model provides an adequate description of diffusion-controlled proton transfer and electron transfer reactions. In a first step, basic concepts will be introduced that describe the intrinsic charge transfer step for both proton and electron transfer. The celebrated Marcus theory [Marcus, 1956a,b, 1957a,b, 1982; Marcus and Sutin, 1985] describes electron transfer between two reactants that are kept at a fixed distance. Using Transition State Theory (TST) and approximate models for the solvent the model developed by Rudolph A. Marcus allows a description of weak-overlap electron transfer reactions. It shows the relationship between the rate constant and the free energy of the reaction. Rehm and Weller [Rehm and Weller, 1970] illustrated that the Marcus free energy gap law is insufficient to describe bimolecular electron transfer reactions in solution. Therefore the SCK model has been implemented in order to account for the diffusion influence on the observed reaction rate coefficient. The unsatisfying result made scientists realise that the SCK model is restricted to reactions that occur at one specific contact distance, only [Eads et al., 1990]. Electron transfer, however, might even occur at long distances [Brunschwig et al., 1984] with different distance-dependent rate constants. By contrast, protons are considerably more localised and tunnel over much shorter distances of less than 1 Å[Kuznetsov and Ulstrup, 1999]. That is why there is no long-range proton transfer whatsoever. As a result, time-resolved measurements provided evidence for an adequate description of diffusion-controlled proton transfer reactions by the SCK model.

1.3 Bimolecular electron transfer dynamics

Electron transfer (ET) in solution has been observed for the first time in 1808 when Humphry Davy let potassium react with ammonia which yielded a blue colour [Thomas et al., 2008]. Since this time, a vast number of experimental and theoretical studies have exploited one of the most common chemical reactions [Kuznetsov and Ulstrup, 1999]. Different types of ET exist:

- ET between neutral molecules leads to charge separation (CS) and ionic products:
  $$\mathrm{A + D \rightarrow A^- + D^+}.$$
- ET between two ionic constituents leads to charge recombination (CR):
  $$\mathrm{A^- + D^+ \rightarrow A + D}.$$
  It can occur within a geminate pair and in the bulk between separated ions, the first one is called geminate recombination whereas the latter is called homogeneous recombination.
- When the electron is transferred from an ion to a neutral molecule, the reaction is called charge shift:
  $$\mathrm{A + D^- \rightarrow A^- + D}.$$

ET reactions can be triggered in different ways. There are electrochemical, thermal and photoinduced electron transfer reactions to name a few. This thesis will focus on the last technique. Here ET occurs between an electronically excited and a non-excited molecule.

The classical Marcus theory

In electron transfer reactions an electron is transferred from an orbital of the electron donor (D) to an orbital of the electron acceptor (A). The transition from donor to acceptor occurs within the activated complex. Due to the fact that electronic motions are more rapid than atomic motions, reactant and product have the same nuclear configuration within the activated complex resulting in the conservation of internal energy. Both, reactant and product, have a potential energy which is a function of many intra- and intermolecular nuclear coordinates resulting in a multidimensional potential energy surface. A precise potential energy surface (PES) has to consider the potential energy of each molecule within the system including the surrounding solvent. This results in a large number of coordinates which is impossible to handle. In transition state theory one generalised nuclear coordinate is introduced, the so-called reaction coordinate Q. Therefore the potential energy surface is reduced to an one-dimensional profile with Q representing an average configuration of all molecules of the system. Marcus demonstrated that the system can be presented by Gibbs free energy space. The non-adiabatic free energy profiles are often assumed to be quadratic functions of the reaction coordinate with equal force constants for reactants and products (Figure 1.4). ΔQ represents

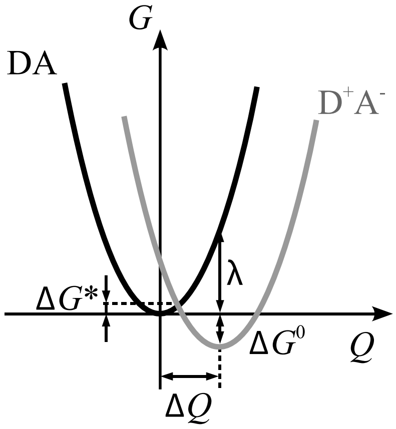

Figure 1.4: Free energy profiles of reactant DA and product D^+A^- along the reaction coordinate Q. ΔG^*: free activation energy, ΔG^0: free energy, λ: reorganisation energy, ΔQ: horizontal displacement.

the displacement of the equilibrium configuration of the product state in respect of the reactant state. The intersection between the two parabolas represents the free activation energy, ΔG^*, which can be calculated in the following way:

$$\Delta G^* = \frac{(\Delta G^0 + \lambda)^2}{4\lambda} \tag{1.49}$$

by using the reorganisation energy λ and the free energy of the reaction ΔG^0. λ is the energy that is needed by reactants and solvent to reach the equilibrium configuration after electron transfer. λ consists of two contributions:

$$\lambda = \lambda_i + \lambda_s. \tag{1.50}$$

λ_i is the intramolecular reorganisation energy which evolves from changes in bond lengths and angles. It represents the change in free energy if the reactant is deformed to the equilibrium configuration of the product without transferring an electron. The solvent reorganization energy, λ_s, is the energy that solvent molecules need to reorient in order to establish an equilibrium with the products. From the dielectric continuum approach, it is possible to express λ_s as follows:

$$\lambda_s = \frac{\mathrm{e}^2}{4\pi\varepsilon_0}\left(\frac{1}{2R_\mathrm{A}} + \frac{1}{2R_\mathrm{D}} - \frac{1}{R_\mathrm{AD}}\right)\left(\frac{1}{\varepsilon_{op}} - \frac{1}{\varepsilon_s}\right). \tag{1.51}$$

In this model, the electron donor and acceptor molecules are respectively approximated with spheres of radii R_D and R_A. The distance between the centers of these two spheres is R_{AD}, ε_{op} and ε_s are the optical and static dielectric constants of the solvent, ε_0 denotes the permittivity of the vaccum and e is the charge that is transferred. It is readily identifiable that, the more polar the solvent, the larger is the solvent reorganization energy. For non-polar solvents, ε_{op} and ε_s are equal and therefore the reorganization energy equals zero.

ΔG^0 is the difference in free energy between the equilibrium configurations of the reactant and product states and therefore the driving force of the reaction. In order to determine if a photoinduced electron transfer reaction is feasible for a donor-acceptor pair Weller proposed the following expression [Rehm and Weller, 1970]:

$$\Delta G^0 = -E_{00} + E(\mathrm{D}^+|\mathrm{D}^0) - E(\mathrm{A}^0|\mathrm{A}^-) + C + S, \tag{1.52}$$

where E_{00} is the difference in energy between the electronic ground state and the electronic excited state of the photo-excited precursor. $E(\mathrm{D}^+|\mathrm{D}^0)$ and $E(\mathrm{A}^0|\mathrm{A}^-)$ are the oxidation and reduction potentials of the donor and acceptor in acetonitrile. The Coulomb term C is only valid for non-contact ions and accounts for the electrostatic interaction between the two ions [Atkins, 1990]:

$$C = -\mathrm{e}^2\frac{1}{4\pi\varepsilon_0\varepsilon_s R_\mathrm{AD}}. \tag{1.53}$$

In case of using another solvent than acetonitrile one has to use the correction term S for the solvation energy:

$$S = -\mathrm{e}^2\frac{1}{8\pi\varepsilon_0}\left(\frac{1}{R_\mathrm{A}} + \frac{1}{R_\mathrm{D}}\right)\left(\frac{1}{\varepsilon_\mathrm{MeCN}} - \frac{1}{\varepsilon_s}\right). \tag{1.54}$$

Within the framework of TST, electron transfer reactions can be qualitatively described in such a way: initially, the system is located at the bottom of the reactants well the donor-acceptor pair is in equilibrium with the surrounding solvent. Due to solvent fluctuations, the system is driven out of the equilibrium and reaches thereby the transition state. Transfer of the electron from donor to acceptor molecule occurs at the intersection of the surfaces of reactant DA and product $\mathrm{D}^+\mathrm{A}^-$. The probability for the transition of the system from reactant to product well, is expressed in the electronic transmission coefficient κ which is given by the Landau-Zener theory [Heitele, 1993]. After the product well is reached the system relaxes quickly to its bottom and an equilibrium with the solvent is established. The electron transfer rate constant, k_{ET}, depends on the free activation energy, ΔG^*, and can be expressed as follows:

$$k_{ET} = \nu_n \kappa \exp\left(-\frac{\Delta G^*}{k_B T}\right) \tag{1.55}$$

with ν_n, the frequency of nuclear passage through the transition state which typically is $10^{13}\,\mathrm{s}^{-1}$ [McManis et al., 1991]. The Landau-Zener theory describes the transition between two intersecting potential surfaces in one dimension [Zener, 1932, 1933; Landau, 1932b,a]. The probability P for the system to stay in the reactant well after one transition through the transition state is given by:

$$P = e^{-\Gamma} \qquad \text{with} \qquad \Gamma = \frac{2\pi}{\hbar v} \frac{|V_{\mathrm{DA}}|^2}{|F_{\mathrm{D}} - F_{\mathrm{A}}|}. \tag{1.56}$$

The Massey-parameter Γ depends on the electronic coupling element V_{DA}, the velocity v at the intersection and the difference in slopes of the free energy surfaces. Finally, the electronic transmission coefficient κ can be calculated in subject to P:

$$\kappa = 1 - P + P(1-P)P + P(1-P)^3 P + P(1-P)^5 P + ... \tag{1.57}$$

The probability for the system to change the free energy surface (FES) during the first passage through the transition state is equal to $1 - P$. In case it stays on the FES of the donor the probability for a change to the FES of the acceptor during the second passage equals $P(1 - P)$. The system can pass the transition state many times before it actually changes the FES as expressed in (1.57).

Of fundamental importance for ET is the electronic coupling V_{DA} between the reactant and product states. With this parameter ET reactions can be distinguished into two classes as shown in Figure 1.5:

1. Is the electronic coupling between the two states weak, they do not interact significantly. Consequently, the free energy surfaces are two separate intersecting surfaces with no deformation near the intersection. The transition from the reactant FES to the product FES only occurs occasionally. κ is approximately:

   $$\kappa \propto |V_{\mathrm{DA}}|^2. \tag{1.58}$$

   The ET reaction is called non-adiabatic.

2. Strong electronic coupling between two states leads to a mechanism called avoided crossing. This results in a splitting of the surfaces in the intersecting region and two new free energy surfaces are formed. ET can be described as a transition from the reactant well to the product well along the lower surface. Therefore the ET reaction is called adiabatic. κ is equal to unity.

The reorganisation of the dielectric polarisation of the surrounding solvent, due to the change in dipole moment when going from reactants to products, is described by the solvent relaxation time τ_s^{-1}. The ratio between the ET rate constant and the inverse solvent relaxation time determines the model for a proper description of the ET reaction. Marcus theory describes non-adiabatic ET reactions which holds for $k_{ET} \ll \tau_s^{-1}$.

For non-adiabatic ET the classical expression for the ET rate constant derived by Marcus

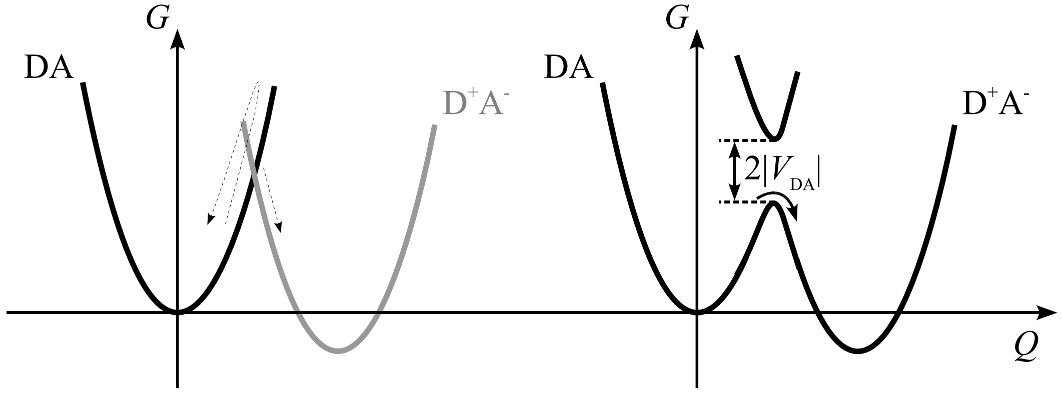

Figure 1.5: Schematic presentation of non-adiabatic (left) and adiabatic (right) ET.

is given as:

$$k_{ET} = \frac{2\pi}{\hbar} \frac{1}{\sqrt{4\pi\lambda k_B T}} |V_{\mathrm{DA}}|^2 \exp\left(-\frac{(\Delta G^0 + \lambda)^2}{4\lambda k_B T} \right). \tag{1.59}$$

Figure 1.6 shows the free energy profiles for the three regimes and the corresponding dependence of the transfer rate on ΔG^0. For convenience ΔQ is kept fixed in all three cases whereas ΔG^0 increases from left to right. The ET rate constant increases with increasing free energy gap (ΔG^0) of the reaction as long as the free energy gap has a lower magnitude than the reorganisation energy. The ET rate constant reaches its maximum value when the free energy gap is equal to the reorganisation energy and a crossover occurs. With a further increase of the free energy gap the rate will decrease. This dependence is known as Marcus free energy gap law. Following three regimes are observed:

1. $-\Delta G^0 < \lambda$: normal regime
2. $-\Delta G^0 = \lambda$: barrierless regime
3. $-\Delta G^0 > \lambda$: inverted regime

According to (1.49) the free activation energy approaches zero when the free energy gap increases until it has the same magnitude as the reorganisation energy. This explains the increase of the ET rate constant. Further increase of the free energy gap leads again to a reaction barrier ΔG^*.

Quantum effects

The classical Marcus theory does not give a adequate description of very exergonic ET reactions [Iwaki et al., 1996]. The predicted rate constants are much smaller than those observed due to disregarded quantum effects. Nuclear tunneling can play an important role in the reaction dynamics since the stationary vibrational wavefunction is not strictly localised on the FES of the reactants but partly reaches into the FES

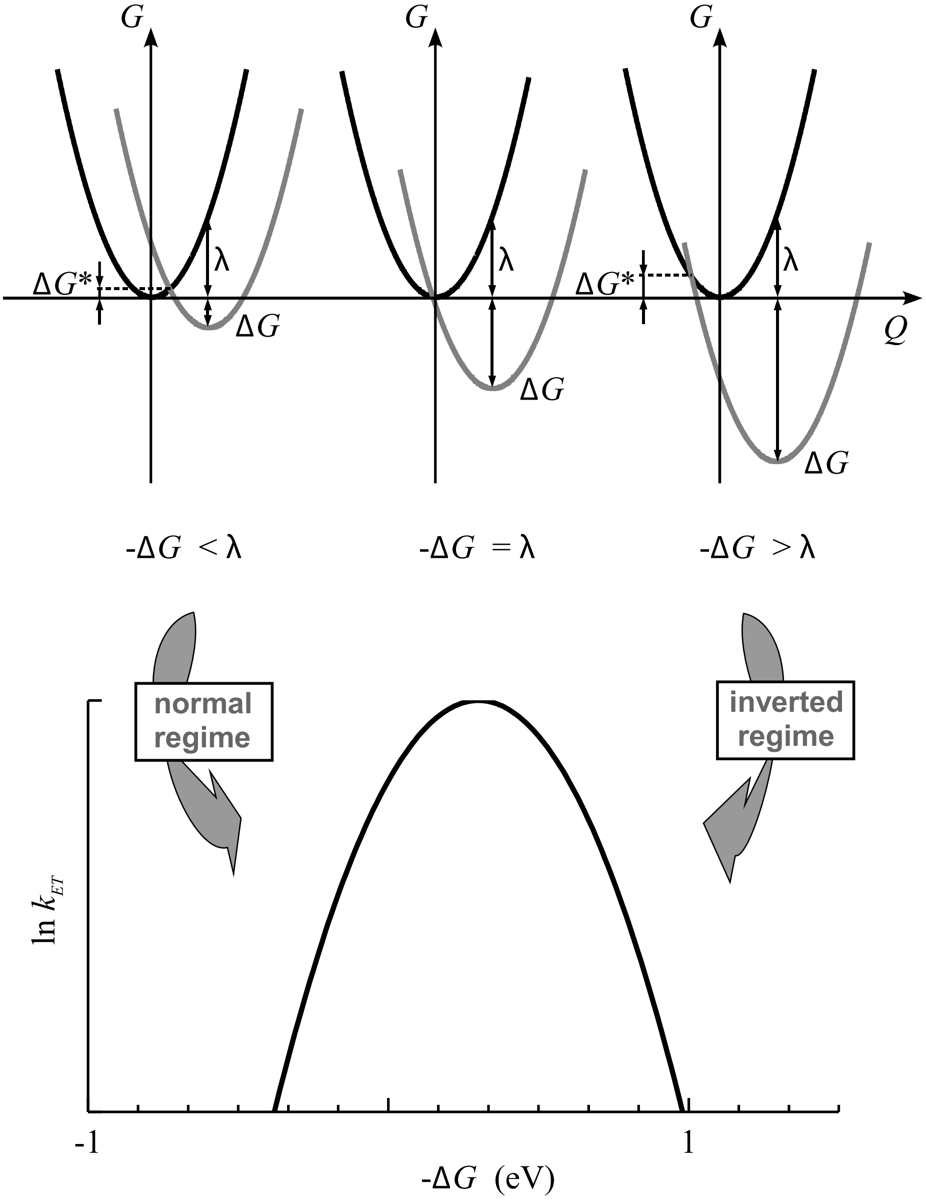

Figure 1.6: Upper Panel: Free energy profiles of reactant (black line) and product (grey line) for non-adiabatic ET to illustrate the free energy regimes after Marcus: normal, barrierless and inverted. Below: Marcus bell-shaped free energy gap law.

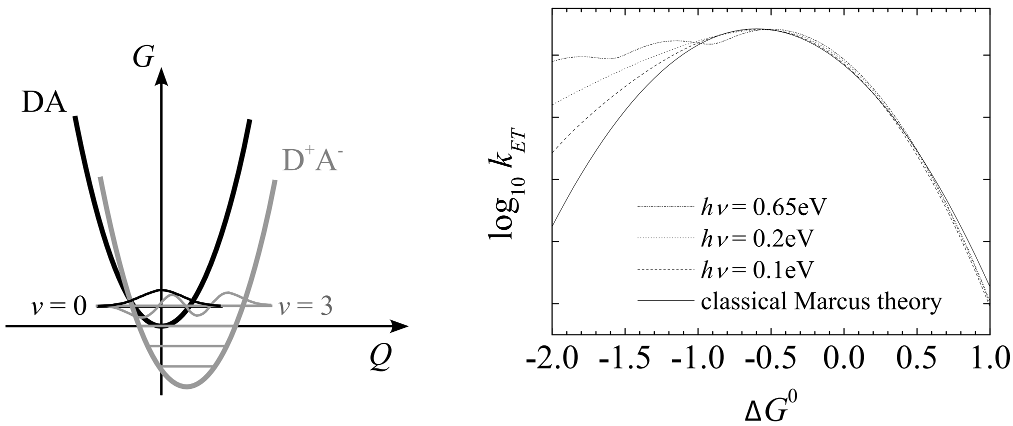

Figure 1.7: Left: schematic presentation of the vibrational overlap between the reactant DA and product D^+A^- vibrational wavefunctions. Right: $\log_{10} k_{ET}$ as a function of ΔG^0 compared between the classical and semiclassical Marcus theory. In the semiclassical Marcus theory the inverted regime becomes less pronounced the higher the vibrational frequency of the involved vibrational state. Parameters: $V_{\mathrm{DA}} = 1.2{\cdot}10^{-3}$ eV, $T = 298$ K, $\lambda_s = 0.5$ eV, $\lambda_i = 0.1$ eV and $v_{max} = 9$.

of the products. The overlap between the vibrational wavefunctions of reactant and product states becomes stronger the higher the exergonicity of the reaction. In the semi-classical Marcus theory ET occurs from the thermally populated vibrational states of the reactant to high frequency vibrational states of the product (Figure 1.7). The first-order rate constant for electron transfer at fixed r is given by:

$$k_{ET} = \frac{2\pi}{\hbar} |V_{\mathrm{DA}}|^2 (F.C.), \tag{1.60}$$

with the Franck-Condon factor $(F.C.)$. $(F.C.)$ is a sum of products of overlap integrals of vibrational and solvational wavefunctions of the reactants with those of the products, suitably weighted by Boltzmann factors. If the energy of the low frequency polarisation modes of the solvent is smaller than the thermal energy ($h\nu_s < k_B T$), one may treat the intramolecular reorganisation energy (λ_i) in a quantum-mechanical way and the solvent reorganisation energy (λ_s) in a classical way, by using the solvent continuum model (1.51). In this case the Franck-Condon factor is given by [Marcus and Sutin, 1985]:

$$(F.C.) = \sum_{v_r, v_p} \frac{1}{\sqrt{4\pi\lambda_s k_B T}} \exp \frac{-(\Delta G^0 + \Delta\varepsilon_v + \lambda_s)^2}{4\lambda_s k_B T} (FC)_v p(v_r). \tag{1.61}$$

$(FC)_v$ is the Franck-Condon factor associated with the vibrational overlap for any given set of vibrational quantum numbers v_r of the reactants' and v_p of the products' system, $p(v_r)$ is the equilibrium probability of finding the system in the vibrational state v_r and the sum is over all v_r and v_p. The quantity ε_v is the vibrational energy of the products minus the one of the reactants for a set of quantum numbers (v_r, v_p). When a single vibration frequency ν is principally involved in the readjustment of nuclear coordinates associated with the electron transfer, (1.61) can be approximated. This leads to the following expression of the rate constant:

$$k_{ET} = \frac{2\pi}{\hbar}\frac{1}{\sqrt{4\pi\lambda_s k_B T}}|V_{\mathrm{DA}}|^2 \sum_{v=0}^{\infty} e^{-S}\frac{S^v}{v!}\exp\left(-\frac{(\Delta G^0 + vh\nu + \lambda_s)^2}{4\lambda_s k_B T}\right) \tag{1.62}$$

with v, the number of vibrational quanta excited in the product state. S is the electron-vibration coupling constant also known as Huang-Rhys factor:

$$S = \frac{\lambda_i}{h\nu}\,. \tag{1.63}$$

Comparing the expressions of the ET rate constant derived by the classical (1.59) and semi-classical (1.62) (Figure 1.7) Marcus theory it is readily apparent that the effect of excited high frequency vibrations in the product state is to absorb amounts of $vh\nu$ of the excess energy. This reduces the exergonicity and consequently makes the reaction faster than predicted by classical Marcus theory with $v = 0$.

Experimental confirmation of Marcus theory

Since theoretical prediction of the bell-shaped free energy gap law by Marcus much experimental effort has been put into testing this theory [Rehm and Weller, 1970; Miller, 1984; Wasielewski et al., 1985; Mataga et al., 1988; Vauthey et al., 1988; Guldi and Asmus, 1997]. Indeed, several approaches confirmed the existence of the three free energy regimes: Miller and coworkers studied the intramolecular charge shift reaction with the help of rigid bichromophoric molecules of well-defined separation distance in solution [Miller, 1984]. By replacing one of the two chromophores they gradually adjusted the driving force from -0.05 eV to -2.4 eV and measured the electron transfer rate. In a similar way Wasielewski *et al.* observed the normal, barrierless and inverted regime by studying photoinduced intramolecular charge separation and charge recombination reactions [Wasielewski et al., 1985]. However, as mentioned before intermolecular charge transfer reactions - like ET - are influenced or even controlled by encounter diffusion of the reaction partners. As a result, Rehm and Weller observed a violation of the free-energy-gap-law [Rehm and Weller, 1970]: in 1970 they measured the fluorescence quenching rate constant of more than 60 electron donor-acceptor pairs in acetonitrile thereby tuning the exergonicity of the ET reaction from +5.7 kcal/mole to -60.8 kcal/mole (+0.25 eV to -2.65 eV). With this they covered the whole range from the normal to the inverted regime. Figure 1.8 shows the observed quenching rate constant k_q as a function of the free energy ΔG^0 of the ET reaction. In the normal regime the experimental results are in good agreement with the predictions of the Marcus theory. For increasing ΔG^0 beyond -15 kcal/mole (-0.65 eV), however, strong deviations are apparent. The inverted regime is obviously absent. This can be explained, at least to some extent, by comparing the observed fluorescence quenching rate with the calculated steady-state diffusion rate constant, $k_d = 2{\cdot}10^{10}\ \mathrm{M}^{-1}\mathrm{s}^{-1}$. In the normal regime the overall reaction kinetics is controlled by electron transfer reaction: the ET rate constant is smaller than the diffusion rate constant. With an increasing ET rate the intrinsic ET reaction can compete with the diffusion and the overall observed rate is the sum of the time for the encounter diffusion and the intrinsic reaction. Once the ET reaction

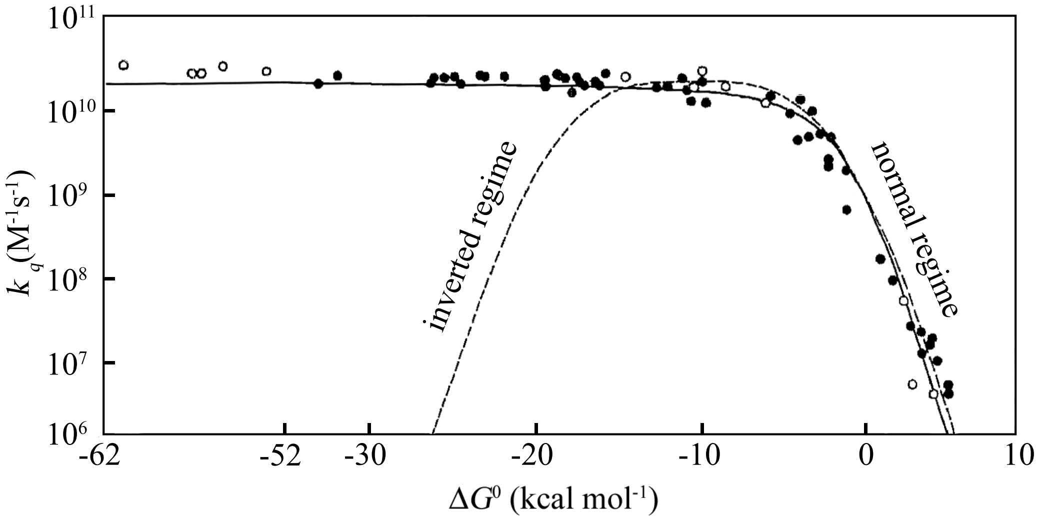

Figure 1.8: Fluorescence quenching rate constant k_q as a function of the free energy ΔG^0 of the ET reaction; black dots: $A^* + D$; open dots: $D^* + A$; dashed line: free energy gap law by Marcus. Taken from [Rehm and Weller, 1970].

becomes faster than the encounter diffusion the overall reaction is diffusion-controlled resulting in an observed fluorescence quenching rate constant that is independent on the exergonicity of the ET reaction. Therefore the barrierless regime cannot be experimentally observed. However, this is different for the inverted regime. According to Marcus theory the ET rate constant is predicted to decrease with increasing exergonicity and as such the intrinsic ET reaction should become again the rate-determining step. As a result, Rehm and Weller should have observed a bell-shaped energy gap law even though diffusion of the reaction partners might modulate the observed rate. Two explanations were proposed in order to address this problem:

(i) The distance between the reactants affects the solvent reorganisation energy, λ_s.

(ii) The photoinduced electron transfer reaction might lead to the formation of products in an electronically excited state.

(i) Distance-dependent electron transfer

One possible explanation is based on the distance dependence of parameters that determine the ET rate constant. The electron transfer reaction is fastest in the barrierless regime, when the exergonicity equals the reorganisation energy ($\Delta G^0 = \lambda$). For polar solvents - like acetonitrile - the solvent reorganisation energy λ_s, as described by (1.51), depends on the distance between the reactants: the larger the distance the larger the solvent reorganisation energy. Due to screening of the Coulomb interaction between the ionic products the distance dependence of the exergonicity of electron transfer reaction is negligible. As a result, the increasing solvent reorganisation energy at greater distances between the reactants serves to shift the maximum ET rate constant towards larger exergonicities. The rate constant will therefore increase until it has reached a plateau which is in accordance with the experimental results of Rehm and Weller. However, the model assumes long-range electron transfer over large distances and neglects the distance dependency of the electronic coupling constant V which is known to decrease exponentially with the interionic distance [Brunschwig et al., 1984]:

$$V(r) = V_0 \exp\left(-\frac{2(r-\sigma)}{L}\right). \tag{1.64}$$

V_0 is the electronic coupling constant at contact distance σ and L is the tunneling length. It is the distance of effective electronic coupling which is usually in the order of a few Angströms [Miller, 1975; Beitz and Miller, 1979]. With this it is possible to write the general distance-dependent rate constant:

$$k_{ET}(r) = V_0^2 \exp\left(-\frac{(r-\sigma)}{L}\right) \sqrt{\frac{\pi}{\lambda(r) k_B T}} \exp\left(-\frac{(\Delta G^0(r) + \lambda(r))^2}{4\lambda(r) k_B T}\right). \tag{1.65}$$

Using the classical SCK model as described in chapter 1.2 has been proven to be inappropriate to reveal the intrinsic ET reaction rate constant. The reaction dynamics of ET cannot be described with a contact model that is based on a hard boundary condition. Fleming and coworkers studied the diffusion-influenced ET reaction between rhodamine B and ferrocyanide using fluorescence upconversion as well as time-correlated single photon counting and concluded that the SCK contact model cannot describe the initial rapid decay and the slower decay consistently [Eads et al., 1990]. The parameters that were extracted from the fit of the short time data give a poor description of the long time decay and *vice versa.* This deficiency is inherent in the contact approximation which completely ignores the static quenching, preceding the diffusional one. Therefore another model was designed that incorporates a distance-dependent rate constant to account for remote electron transfer in liquid solution influenced by the encounter diffusion, the so-called differential encounter theory (DET)[Wilemski and Fixman, 1973; Burshtein, 2000]. It describes the time-dependent rate coefficient by incorporating a simple position-dependent sink model [Wilemski and Fixman, 1973; Burshtein, 2000]. The major difference to the SCK contact model is the definition of the time-dependent rate constant:

$$k_{ET} = \int k(r) \rho(r,t) dV \tag{1.66}$$

with the distance-dependent unimolecular rate constant $k(r)$, the time-dependent radial distribution function $\rho(r,t)$ and the volume element dV. One consequence of a position-dependent rate is the possibility for donor-acceptor pairs to be separated by sufficiently small distances that upon excitation, these pairs will react with a rate dominated by the intrinsic reaction rate which is generally referred to as static quenching. In contrast to the SCK contact model, the temporal variation of the distribution function is now not entirely determined by diffusion but also by the disappearance of reactants upon ET:

$$\frac{\partial \rho(r,t)}{\partial t} = D\left[\frac{\partial^2 \rho(r,t)}{\partial r^2} + \frac{2}{r}\frac{\partial \rho(r,t)}{\partial r}\right] - k(r)\rho. \tag{1.67}$$

With this model at hand Gladkikh *et al.* fitted successfully the entire kinetics of fluorescence quenching due to remote electron transfer in the inverted regime [Pagés et al., 2004]. Their study of the bimolecular charge separation between perylene and tetracyanoethene in acetonitrile covers different time scales from static to stationary quenching. They showed that the fitting of the data is only satisfactory when based on a double-channel model.

(ii) Electronically excited state

In the double-channel model charge separation can either occur to the electronic ground state or to an electronic excited state of the generated radical ionic chromophore. In case the donor molecule is excited, charge separation leads to the radical cation of the excited chromophore. Small cationic aromatic chromophores tend to have relatively low lying excited states. In highly exergonic photoinduced charge separation reactions these states might be lower in energy than the initially excited S_1-state of the chromophore. Fermi golden rule predicts for a nonradiative electronic transition, such as charge separation, a larger transition probability to the energetically closer state, assuming that the transition is allowed and the transition matrix elements are of the same order of magnitude. The exergonicity of charge separation leading to the electronically excited radical cation is smaller than the exergonicity of charge separation that generates the ground state radical cation. Since the energy of photoexcitation is fixed, $E_{00} = E_{\mathrm{D}^*} - E_{\mathrm{D}}$, the exergonicity of charge separation, charge recombination and internal conversion are rigidly tied:

$$E_{00} = \Delta G^0_{\mathrm{CS}} + \Delta G^0_{\mathrm{CR}} + \Delta G^0_{\mathrm{IC}}. \tag{1.68}$$

As a result, depending on the relative time constants for internal conversion and charge recombination the correlation for the exergonicity of charge recombination might be the other way around which is illustrated in Figure 1.9. If charge separation yields an electronically excited radical cation the reaction can be shifted from the inverted to the barrierless regime which results in an increase of the reaction rate constant. This could account for the lack of the inverted regime [Vauthey, 2006].

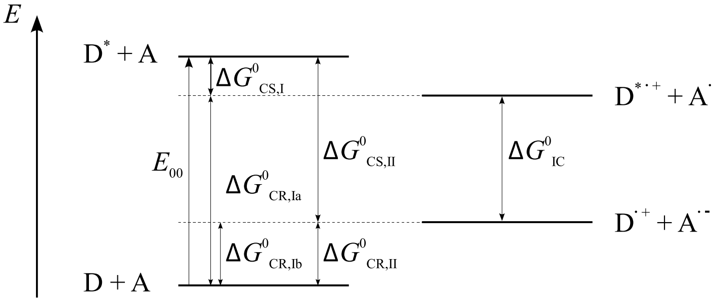

Figure 1.9: Scheme of possible charge separation pathways. I: formation of an excited radical ion pair (weakly exergonic CS); II: formation of a radical ion pair in the ground state (highly exergonic)

1.4 Bimolecular proton transfer dynamics

One particular kind of diffusion-influenced bimolecular reactions of fundamental importance in chemistry and biology is the neutralisation between Brønsted acids and bases. Modern discussions of acid-base reactions which involve proton transfer have evolved from the seminal studies of Eigen and Weller [Weller, 1958, 1961; Eigen, 1964; Eigen et al., 1964]. They proposed a model of an overall three-step reaction scheme to describe reversible acid-base reactions in solution as being diffusion-influenced. The first step is made of diffusional motion, in which acid and base approach each other to form an encounter pair when the mutual distance equals the reaction contact radius. During the second step the intrinsic proton transfer proceeds. The overall reaction is completed by the third step, the subsequent separation of the products by diffusion. Since that time, several groups studied acid-base reactions in the time-domain with different techniques such as time-resolved fluorescence and femtosecond UV-pump/VIS-probe spectroscopy [Pines et al., 1997; Genosar et al., 2000; Cohen et al., 2000, 2001]. Genosar *et al.* have been able to disentangle the two processes and in doing so they revealed an intrinsic bimolecular proton transfer rate of $1.6{\cdot}10^{11}$ $M^{-1}s^{-1}$ and $4{\cdot}10^{10}$ $M^{-1}s^{-1}$ between the photoacid 8-hydroxy-1,3,6-pyrene trisulfonate (HPTS) and the base acetate in H_2O and D_2O, respectively. In order to extract the rate constants they used the analytic approximation of the SCK model for a known Coulomb potential derived by Szabo [Szabo, 1989]. Since these values are about 20 times larger than the corresponding diffusion-limited rate constants it was shown that the overall bimolecular reaction rates are indeed time dependent. In spite of the low time resolution of about 50 ps Cohen *et al.* studied the nature of nonexponential kinetics in acid-base reactions with the photoacid 2-naphthol-6-sulfonate and high concentrations of acetate in a medium of high viscosity thereby slowing down the diffusion. They adequately described the observed nonexponential reaction rate with the SCK model.

Recently Nibbering, Pines and co-workers refined the classic Eigen-Weller model that describes acid-base reactions (Figure 1.10). With femtosecond UV-pump/IR-probe spectroscopy they studied the neutralisation reaction between the photoacid HPTS and the carboxylate base family $CH_{(3-x)}Cl_xCOO^-$ (x = 0 - 3) in aqueous solution. Going from acetate to trichloroacetate they gradually decreased the basicity and in doing so they tuned the overall deuteron transfer reaction from diffusion-control to activation-control. This approach allowed a more profound understanding of the proton transfer mechanism [Rini et al., 2003, 2004; Mohammed et al., 2005b, 2007a,b]:

At the time, the proton transfer reaction is induced with an ultrashort UV pump pulse, the base molecules are distributed around the acid molecules in a certain fashion. One fraction of acid and base molecules are well separated by a large number of water molecules, n. General there are two competing pathways. The acid can give its deuteron to bulk water which is eventually picked up by a base, or acid and base molecules diffuse towards each other before they react. Their mutual approach is accompanied by a gradual desolvation process of both molecules leading to the formation of an encounter pair. Once the encounter pair is formed as a consequence of the diffusional motion of the reactants, further non-diffusional desolvation occurs to either a reactive complex, the solvent switch, which consists of an unspecified number of water molecules ($n \geq 2$) or to the so called loose complex where acid and base are separated by one water molecule ($n = 1$). Complete desolvation can occur leading to directly hydrogen bonded

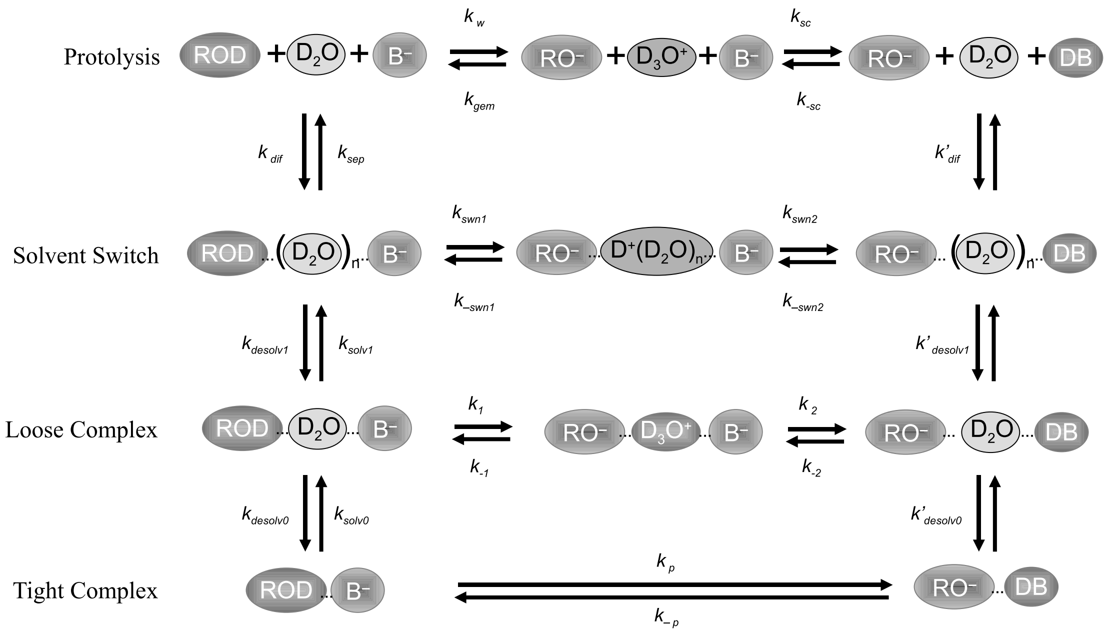

Figure 1.10: Reaction scheme showing the deuteron transfer pathways in the acid-base neutralisation reaction in D_2O, taken from [Mohammed et al., 2007b]. Abbreviations: w: deuteron dissociation to water; gem: geminate recombination; sc: deuteron scavenging; dif: diffusion; sep: separation; swn: switch consisting of n water molecules; (de)solv: (de)solvation; p: direct deuteron between acid and base.

acid-base complexes, also referred to as tight complexes. All of these different kinds of complexes might be present before the reaction is triggered. This allows to extract the intrinsic deuteron transfer time constant corresponding to the particular reactive complex. For tight and loose complexes they found that the first deuteron step happens within their experimental time resolution of 150 fs, independent from the basicity of the base. In tight complexes deuteron transfer proceeds directly to the base whereas in loose complexes the bridging water molecule is deuterated. The second step, the deuteron transfer from the water bridge to the accepting base depends on the basicity of the base: the weaker the base is the slower is the deuteron transfer and *vice versa.* For weak bases they had to consider the backward deuteron transfer reaction. By doing so they concluded for all bases:

- In tight complexes the forward transfer is one order of magnitude faster than the backward transfer.
- The second deuteron transfer step within loose complexes is activated and controlled by the basicity. The weaker the base is the smaller is the forward reaction rate but the larger is the backward rate and *vice versa.*
- Within solvent switches: the first deuteron transfer step, deuteron transfer to the water bridge, is like in the other two complexes insensitive to the base strength although slower than in these. Again the second transfer, final deuteron transfer to

the base, becomes slower with decreasing basicity whereas the backward transfer becomes faster with decreasing basicity. This pathway seems to come into play for weak bases like Cl_3CCOO^-.

Altogether, the actual proton transfer pathway depends on particular acid and base reactivities, reaction rates and (de)solvation energetics and dynamics.

Understanding of proton transfer of an acid-base complex in liquids involves the determination of potential energy surfaces of these complexes taking into account the fluctuation of the solvent. The standard theoretical framework is based on Eyring transition state theory [Eyring, 1935]: an activated complex is located along the proton transfer coordinate through which the system traverses. The transition state model for proton transfer has been modified by Bell to account for the quantum nature of the proton [Bell, 1980]. He implemented the tunnelling correction which serves to enhance the predicted rate of proton transfer. However, TST can only be used under certain constraints:

(i) Thermodynamic equilibrium prevails throughout the entire system for all degrees of freedom. Hence, processes like solvation and vibrational relaxation have to be faster than charge transfer.

(ii) The system crosses the activation barrier once and recrossings are neglected.

In proton transfer reactions these restrictions might not be realistic. Kramers' theory takes into account the effect of the interaction between the system and the solvent on the motion of the reactants on the potential energy surface [Kramers, 1940; Hänggi et al., 1990]. The system moves on the potential energy surface subject to friction and random forces of the surrounding solvent. As a consequence, the system exchanges energy with the environment and the trajectory through the transition state can become random. This leads to a relation between the rate constant for the proton transfer and the dielectric relaxation time of the solvent. These theories have been used with great success to predict reaction rates and yields. Another model emerged from German, Kuznetsov and Dogonadze who proposed that the transition state is to be found in the solvent coordinate rather than the proton transfer coordinate [German et al., 1980; German and Kuznetsov, 1981]. Like in the description of weak-overlap electron transfer, the reaction path involves an initial solvent fluctuation to bring the reactant and product states into resonance. In non-adiabatic proton transfer, the proton tunnels afterwards through the electronic barrier found in the proton transfer coordinate. If there is no electronic barrier in the proton transfer coordinate, the proton will move across the surface on a vibrational motion. This reaction pathway is referred to as adiabatic proton transfer. Hynes and co-workers further investigate this model [Ando and Hynes, 1999; Kiefer and Hynes, 2002, 2007].
Another frequently used model is the Marcus electron transfer model adapted for proton transfer [Marcus, 1968, 1975; Cohen and Marcus, 1968]. It is a Bond-Energy-Bond-Order reaction model which can be applied to proton transfer reactions. It reasons that there is a strong correlation between the changes in the bond that is broken and the bond that is formed. Furthermore, it is assumed that along the minimum-energy path from reactants to products the sum of the bond orders is constantly equal to unity. According

to Marcus, the relation between the activation free energy of the proton transfer reaction, ΔG^*, and the free energy of reaction, ΔG^0, is given by:

$$\Delta G^* = \frac{\lambda}{4} + \frac{\Delta G^0}{2} + \frac{\lambda}{4\ln 2}\ln\cosh\left(\frac{2\ln 2\Delta G^0}{\lambda}\right). \tag{1.69}$$

Although this relation has been derived for ground state proton transfer, it has been used successfully to find a correlation between the free-energy reaction rate of excited state proton transfer and the difference between the pK_a of photoacid and conjugate acid of the base (ΔpK_a) in aqueous solution (Figure 1.11) [Pines and Pines, 2002, 2007].

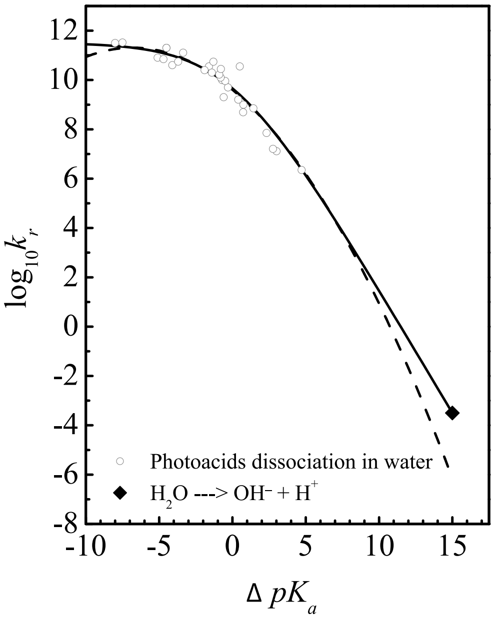

Figure 1.11: Free energy correlation found for proton transfer to water using different photoacids. Solid line is the fit using (1.69) and dashed line the fit using (1.49).

In the free-energy relationship:

$$k_r = k^* \exp\left(-\frac{\Delta G^*}{RT}\right) \tag{1.70}$$

$(k^*)^{-1}$ is the frequency factor of this type of reaction, R is the gas constant and T the absolute temperature. The free energy of reaction can be related to ΔpK_a according to:

$$\Delta G^0 = RT\ln 10\Delta pK_a. \tag{1.71}$$

Figure 1.11 shows the free energy correlation found in photoacid dissociation reactions [Pines and Pines, 2002, 2007]. Solid line is the fit using (1.69) and dashed line the fit using (1.49).

1.5 Geometry of reactive complexes

Existing models that describe charge transfer dynamics such as the presented Marcus theory consider the reactants as symmetric spheres. From a structural point of view the only parameter that affects the reaction rate constant is the distance between the reaction partners. Diffusion-influenced charge transfer reaction theories, that take into account the interplay of diffusional motions and on-contact reaction rates, define a reactive complex which is surely characterised by the complex radius (Figure 1.1). Therefore no information is included on the geometry of these reactive complexes. However, treating molecules as symmetric spheres does not agree with the molecular geometry of many typical reactants. Aromatic molecules, often used in the studies of photoinduced bimolecular charge transfer reactions, have a plane structure of relatively low symmetry such as D_{2h}. The preferred mutual orientation of the reaction partners which leads to a strong interaction is different depending on the nature of the reaction. Intramolecular hydrogen transfer and intermolecular proton transfer processes are mediated by hydrogen bonds and thereby are affected by its strength [Rini et al., 2003]. A hydrogen bond is a weak interaction X-H$\cdots$Y between a functional group XH acting as hydrogen donor and another functional group Y acting as hydrogen acceptor [Latimer and Rodebush, 1920; Pauling, 1928; Bratos et al., 2002]. The strength of the hydrogen bond is determined by the distance between these two functional groups and therefore by the mutual orientation of the two reaction partners. The following correlation was found: the shorter the distance is the higher is the hydrogen bond strength and the faster is the proton transfer reaction. Direct hydrogen-bonded complexes are typical for relatively nonpolar environments. In polar solvents like water both molecules might be solvated and the resulting reactive complex consists of two reactants each retaining its solvation shell. This explains why for a large number of acids and bases the typical reaction contact radius lies between 5 Å and 8 Å[Kosower and Huppert, 1986; Pines et al., 1988; Agmon et al., 1988; Rini et al., 2003, 2004; Mohammed et al., 2005b, 2007b]. In electron transfer reactions the transition occurs generally from the highest occupied molecular orbital (HOMO) of the donor molecule to the lowest unoccupied molecular orbital (LUMO) of the acceptor molecule. The overlap of the two molecular orbitals dictates the kinetics of ET reactions [E. W. Castner et al., 2000]. Since these molecular orbitals are anisotropic the mutual orientation of the reaction partners is crucial for a fast ET reaction.

Rotational relaxation is an ultrafast process characterised by short times (subpicoseconds) between the collisions of the reactants with each other and the surrounding solvent molecules. If reorientation of the asymmetric reactant(s) is faster than the charge transfer reaction between the two reaction partners at optimal mutual orientation, the reactants are spherically averaged and thus isotropic. In the reverse case, the reaction is faster than reorientation, the rate constant depends on the initial orientation of the reactants.

The reaction is then not only modulated by translational but also by rotational diffusion of the reactants which might lead to a variety of reactive complexes with different geometries. Questions arise which need to be answered:

1. Does only one specific reactive complex exist or is there a distribution of com-

plexes?

2. What is (are) the structure(s) of the reactive complex(es)?
3. Is (are) the complex(es) similar or different for different classes of molecules?

In order to address these questions an experimental technique is needed that allows to follow not only chemical reaction dynamics in real time on femtosecond to nanosecond time scales but also to obtain information on ultrafast structural changes. In contrast to electronic transitions many molecular vibrations are of local nature which allows vibrational spectroscopy to gather site-specific information. If the local mode is coupled to the reaction coordinate the inspection of frequency shifts and intensity changes upon reaction of this spectator mode can deduce structural information on the change in molecular geometries and interactions. Besides, vibrational dephasing times are relatively long which leads to narrow infrared absorption bands. The linewidth typically ranges from 5-20 cm^{-1}, only for OH- or NH-vibrations of hydrogen-bonded hydroxy- or amino-groups values of more than 50 cm^{-1} are found. Therefore differences in orientation and thus in interaction between the species - educts, intermediates, products and surrounding solvent - within different reactive complexes might not be masked by overlapping signals. Spectrally resolved signals allow for a distinction between reactive complexes. Polarisation-sensitive infrared spectroscopy is a powerful tool that can deduce information on the mutual orientation of the molecules under certain constraints.

1.6 Outline

This thesis will describe the laser system and the different frequency conversion setups in chapter 2. In chapter 3 a brief introduction to polarisation-sensitive femtosecond ultraviolet pump/mid-infrared probe spectroscopy will be given. This technique uses femtosecond UV pump pulses to trigger the reaction by photoexcitation and the molecular dynamics are followed by probing the induced changes of transmission of the sample with femtosecond mid-IR pulses. The interpretation of the experimental results relies on the understanding of some basic concepts which will be presented: (i) When linearly polarised light is used for both pump and probe pulses information about the anisotropy of a system can be deduced. This can be linked to the mutual orientation of the reaction partners. (ii) In order to understand the differential infrared absorption spectrum of a vibrationally excited molecule the effect of anharmonicity has to be included. In such a way it is possible to determine the time scale of processes like intramolecular vibrational redistribution (IVR) and cooling. In addition it allows to discuss the energy release pathways. Chapter 4 contains an extensive study of photoinduced bimolecular electron transfer reactions of high exergonicity in liquid solution. It raises the question whether radical ion pairs produced upon photoinduced charge separation could be formed in an electronically excited state if accessible from an energetic point of view. In addition, the nature of the charge separation products is examined concerning its geometry and its formation and decay pathways. Chapter 5 reports on the paradigm reaction of solution chemistry: the acid-base neutralisation reaction. Intermolecular proton transfer is studied by using a photoacid, 2-naphthol-6,8-disulfonate (2N-6,8S) and two different bases, cyanate, OCN^-, and bicarbonate, HCO_3^-. These bases are chosen not only to study bimolecular proton transfer dynamics and the structure of reactive complexes but also seeing the generated acids as interesting subjects in itself. The protonation of cyanate might occur at its N-terminal or at its O-terminal which raises the question if the protonation is selective and the reaction product can be linked to the structure of the reactive complex. On the other hand, carbonic acid is an acid which has never been observed in aqueous solution by means of a direct experimental evidence for its existence.

Finally a summary concludes this thesis.

2 Experimental

The term laser is an acronym and stands for Light Amplification by Stimulated Emission of Radiation. Laser light is electromagnetic radiation with outstanding properties like coherence, directionality, brightness, monochromaticity and the emission of ultrashort pulses achieved by a process called mode locking. In 1917 Albert Einstein showed that stimulated emission is the basic principle of the laser [Einstein, 1917]. Before the first laser was built, the microwave equivalent (MASER) was realised by Townes *et al.* in 1954 [Gordon et al., 1954]. The transition from microwave to optical wavelengths was shown to be possible when Maiman announced the advent of the ruby laser in 1960 [Maiman, 1960]. Already in 1964 mode-locking of several longitudinal modes has been shown to produce pulses [Hargrove et al., 1964]. Since then the time resolution has been pushed gradually from nanoseconds [McClung and Hellwarth, 1962] via picoseconds [Armstrong, 1967; Ippen and Shank, 1975] to femtoseconds [Diels et al., 1978; Fork et al., 1981]. For such a process to be highly efficient an enormous gain bandwidth of the active medium is needed. The Ti^{3+} ion in titanium doped sapphire ($Ti:Al_2O_3$) shows the desired broad emission spectrum from 600 nm to 1000 nm [Moulton, 1986; Albers et al., 1986]. Furthermore, the invention of chirped pulse amplification (CPA) provides high pulse intensities in the order of mJ [Strickland and Mourou, 1985]. Based on such powerful Ti:sapphire laser systems tunable optical parametric amplifiers (OPA) can be applied to generate frequencies from the ultraviolet (UV) to the infrared (IR) at high pulse energies [Wilhelm et al., 1997; Kaindl et al., 2000; Kozma et al., 2003].

2.1 Laser system

The laser system consists of a commercial Ti:Sapphire-based amplifier system and two homebuilt parametric devices as shown in Figure 2.1. A Ti:Sapphire oscillator (Spectra Physics Tsunami) is pumped at 532 nm by an intra-cavity doubled cw $Nd^{3+}:YVO_4$ laser (Spectra Physics Millenia Vs) and regeneratively mode-locked due to an acousto-optical modulator within the cavity generating a periodic loss. The output pulse width is determined by Kerr lensing [Spence et al., 1991; Proctor et al., 1993] and the compensation of group velocity dispersion. The oscillator emits 80 fs pulses centred at 800 nm with a repetition rate of 80 MHz and an average power of 600 mW. After passing a Faraday isolator the oscillator pulses are stretched by a factor of 10^4 before entering the Pockels cell-switched cavity to avoid peak intensities on the optical elements that exceed their damage threshold. The Faraday isolator prevents absorption of reflected pulses from the amplifier by oscillator components. The first Pockels cell injects an oscillator pulse every millisecond reducing the repetition rate from 80 MHz to 1 kHz. Immediately prior to the propagation of the selected pulse through the Ti:sapphire crystal, the crystal is excited to population inversion by a high energy pulse from the intra-cavity doubled Q-switched $Nd^{3+}:YLF$ laser (Spectra Physics Empower) which operates at 1 kHz providing 250 ns pulses of 527 nm light with a pump power of 14 W. After about 25 round trips the pulse

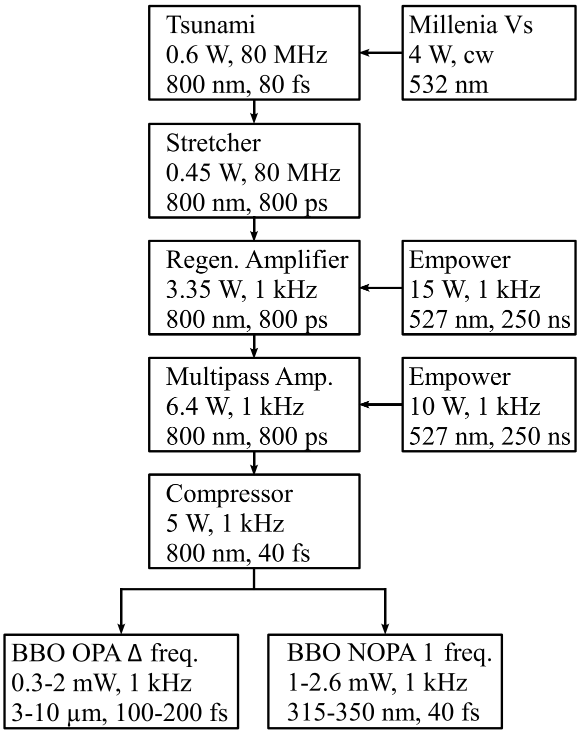

Figure 2.1: Flow diagram of the UV-pump/IR-probe experimental setup.

is amplified to 3.35 mJ and coupled out by a second Pockels cell. Further amplification to 6.4 mJ is achieved in a two-pass Ti:sapphire based amplifier that is pumped with 10 W of 527 nm light delivered by a similar pump laser as for the regenerative amplifier. The compressed pulses of 40 fs with 5 mJ output energy were then split to have the desired pulses of 1 mJ. These pulses were split again by a beamsplitter of 35 % : 65 % to pump simultaneously a noncollinear optical parametric amplifier (NOPA) and an optical parametric amplifier (OPA).

The results presented in sections 4.1 and 4.3 are obtained with a system that is based on a home-built femtosecond kHz laser delivering short pulses of 40 fs with 1 mJ energy and a spectrum peaking at 795 nm [Rini, 2005].

2.2 Nonlinear Optics

Frequency conversion processes are used to realise full tunability options for two-colour pump-probe spectroscopy. The invention of lasers, accompanied by highly intense electric fields gave birth to modern non-resonant nonlinear optics [Bloembergen, 1996; Boyd, 1993; Shen, 1984]. Interaction between an electric field E_i and a dielectric medium changes the charge density distribution of the electrons within the medium which induces a transient polarisation P_i. For weak fields the induced polarisation depends linearly on the field intensity whereas the response of the medium is no longer linear for strong fields. Usually the nonlinear response is treated as a small perturbation and thus descibed as an expansion in powers of the electric field:

$$\begin{aligned} P_i(\omega,t) &= \epsilon_0(\chi^{(1)}_{ij}(\omega)E_j(\omega,t) + \chi^{(2)}_{ijk}(\omega,\omega_1,\omega_2)E_j(\omega_1,t)E_k(\omega_2,t) \\ &\qquad + \chi^{(3)}_{ijkl}(\omega,\omega_1,\omega_2,\omega_3)E_j(\omega_1,t)E_k(\omega_2,t)E_l(\omega_3,t) + \dots) \\ &= P_i^{(1)}(\omega,t) + P_i^{(2)}(\omega,t) + P_i^{(3)}(\omega,t) + \dots \qquad . \end{aligned} \tag{2.1}$$

ϵ_0 is the permittivity of free space and $\chi^{(n)}$ is the electric susceptibility tensor of order n whose magnitude is rapidly decreasing with increasing order. According to Maxwell's equations, such field-induced polarisations act as a source of propagating electromagnetic fields:

$$\Delta\vec{E}(\vec{r},t) - \frac{1}{c^2}\frac{\partial^2}{\partial t^2}\vec{E}(\vec{r},t) = \mu_0\frac{\partial^2}{\partial t^2}\vec{P}(\vec{r},t), \tag{2.2}$$

where c denotes the speed of light in vacuum and μ_0 stands for the permeability of vacuum. The nonlinear polarisation enables energy flow from one or several optical fields into a set of new fields, thereby generating new frequencies of light. The second order polarisation $P_i^{(2)}(\omega)$ gives rise to several frequency converting processes: second harmonic generation (SHG) and sum frequency mixing (SFM) as up-conversion processes and difference frequency generation (DFG) as well as optical parametric amplification (OPA) as down-conversion processes. In up-conversion processes an energetic photon is generated out of two low-energy photons and in down-conversion processes a photon is split into two photons of lower energy (Figure 2.2). Second harmonic generation is a particular case of sum frequency mixing with two identical photons converted into one photon of double energy. The mentioned down-conversion processes are realised in such a way that a pump wave $(\mathbf{k}_1,\omega_1)$ and a seed wave $(\mathbf{k}_2,\omega_2)$ generate a third light wave $(\mathbf{k}_3,\omega_3)$ at their difference frequency. In difference frequency generation pump and seed waves have comparable energies whereas in optical parametric amplification the seed wave is much weaker. The light wave at frequency ω_1 is called the fundamental whereas ω_2 and ω_3 are termed signal and idler, respectively (conventionally $\omega_1 > \omega_2 > \omega_3$). Two conditions have to be fulfilled for the optical frequency conversion process to be effective, namely energy and momentum conservation:

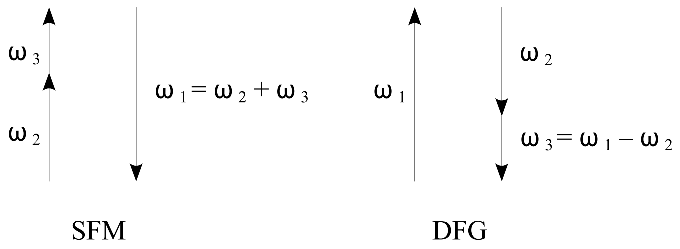

Figure 2.2: Sum frequency mixing (SFM) and difference frequency generation (DFG) presented in the photon picture. ↑: annihilation of a photon, ↓: generation of a photon.

$$\omega_1 = \omega_2 + \omega_3, \tag{2.3}$$

$$\mathbf{k}_1 = \mathbf{k}_2 + \mathbf{k}_3. \tag{2.4}$$

(2.4) describes the phase-matching condition, where identical phases of the three light fields are involved such that constructive interference between the pump wave and the converted waves occurs during propagation through the nonlinear crystal. Dispersion in dielectric media, however, causes different frequencies to propagate at different phase velocities which results in a phase shift. In order to guarantee conservation of momentum the unique properties of birefringent crystals can be exploited [Dmitriev et al., 1997]. Due to an anisotropic arrangement of the crystal lattice, birefringent crystals show an index of refraction that depends on the direction of propagation and the direction of polarisation. In uniaxial birefringent crystals, the **k**-vector of the incident light and one optical crystal axis span the principal plane. Two distinct polarisation directions exist: for light polarised perpendicular to the principal plane (ordinary polarisation), the refractive index n_o is constant with respect to the **k**-vector direction as opposed to light polarised parallel to the principal plane (extraordinary polarisation). Phase-matching is optimal for certain polarisation directions of the three light waves. In type-I phase matching, the signal and the idler wave have the same polarisation direction which is perpendicular to the one of the fundamental wave. In type-II phase-matching, the signal wave is polarised perpendicular to the idler wave [Dmitriev et al., 1997]. Rotation of the crystal normal to the principal plane matches the refractive index for the extraordinary waves to constructively interfere with the ordinary waves over the crystal length according to:

$$n_1 \frac{\omega_1}{c} = n_2 \frac{\omega_2}{c} + n_3 \frac{\omega_3}{c}. \tag{2.5}$$

Three nonlinear crystals are employed to generate mid-infrared light*: β-barium borate (BBO), with the chemical formular β-BaB_2O_4, is frequently used in nonlinear optics. Its interest is based on its high nonlinear coefficient, small dispersion, high damage threshold and a broad transmission range extending from the ultraviolet to the mid-infrared (0.19 - 3 μm). After optical parametric amplification using BBO as nonlinear material the widely tunable signal (ordinarily/vertically polarised) and idler (extraordinarily/horizontally polarised) pulses are converted into their difference frequency employing either $AgGaS_2$ or GaSe as nonlinear crystals. Both crystals provide large transparency at pump and output wavelengths, high nonlinearity, high damage threshold, suitable birefringence for phase matching and low two-photon absorption at all interacting wavelengths. In the wavelength range between 3.5 μm and 8 μm both crystals give comparable mid-infrared pulses in terms of energy and pulse duration. GaSe offers extended tunability towards longer wavelengths up to 20 μm whereas $AgGaS_2$ provides a higher conversion efficiency in the 3 μm region. The crystals used for generation of the ultraviolet pump pulses are all negative uniaxial type I BBO crystals of point group 3m†.

---

* BBO: negative uniaxial, point group 3m, type II, 4 mm, $\theta = 30°$, $\phi = 0°$. $AgGaS_2$: negative uniaxial, point group $\bar{4}2$m, type I, 0.5 mm, $\theta = 37°$, $\phi = 45°$. GaSe: negative uniaxial, point group $\bar{6}2$m, type I, 1 mm.

† SHG: 0.5 mm, $\theta = 29.2°$, $\phi = 0°$. NOPA: 1 mm, $\theta = 30°$, $\phi = 0°$. SFM: 0.1 mm, $\theta = 35.2°$, $\phi = 0°$.

2.3 Femtosecond mid-infrared light pulses

To provide highly stable and widely tunable mid-infrared light pulses an optical parametric amplifier on the basis of β-bariumborate (BBO) in combination with difference frequency generation in GaSe (or $AgGaS_2$) is used [Kaindl et al., 2000]. The basic design is shown in Figure 2.3.

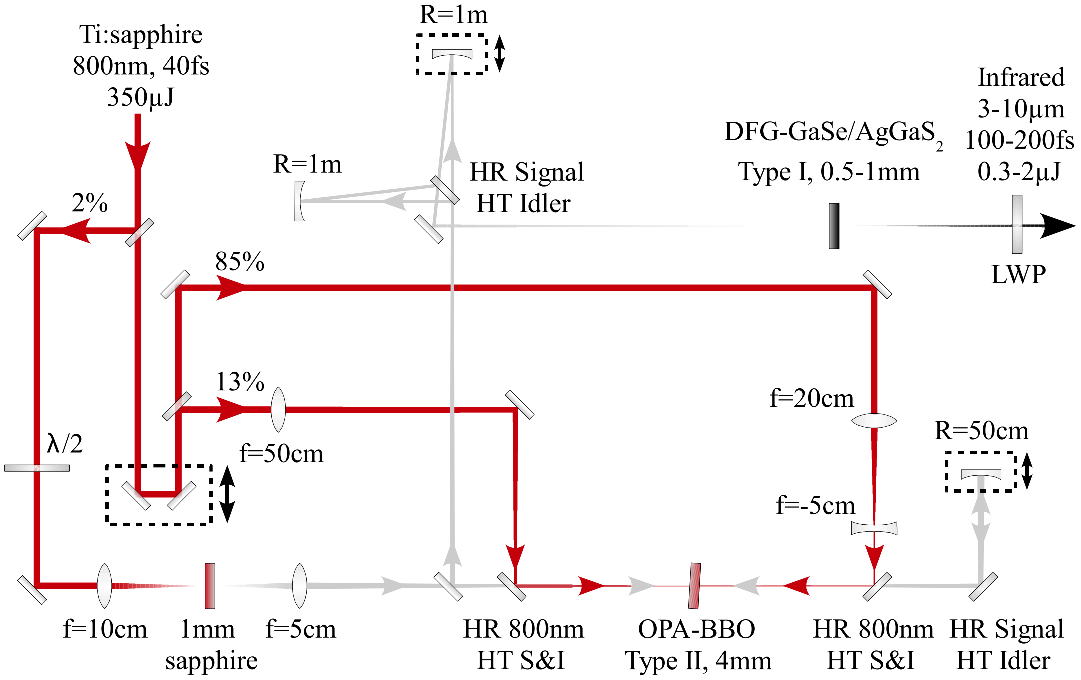

Figure 2.3: Design of the optical parametric amplifier and subsequent difference frequency mixing stage. Note that fundamental and signal of the first and second pass in the amplification stage generating signal and idler are displaced in height. λ/2: half-wave plate, HR/HT: high reflection/transmission, S&I: signal and idler, LWP: long wave pass filter.

The incoming horizontally polarised 800 nm beam (350 μJ) is split into three: a minor fraction (2 %, 7 μJ) is used for the generation of white light continuum. White light contains the near-infrared frequencies of the signal and therefore serves as a seed. Its parametric amplification is achieved by two subsequent amplification stages: the first stage is pumped with a fraction of 13 % (46 μJ) of the fundamental. The major fraction (85 %, 298 μJ) of the fundamental pumps the second amplification stage. For the white light generation the pump pulses are polarisation-rotated by 90° and focused by a lens (f = 10 cm) into a 1 mm sapphire plate. To be amplified the seed is focused into a 4 mm type II BBO crystal and spatially as well as temporally overlapped with the pump pulses of the first stage which are tightly focused (f = 50 cm) into the BBO crystal after passing a variable translation stage. A dichroic mirror separates amplified signal and newly generated idler pulses from the residual fundamental. For the second amplification stage the undesired horizontally polarised idler is removed by a polarising beam splitter and the reflected vertically polarised signal beam is collimated with a concave mirror (radius, R = 50 cm) and sent back into the BBO crystal at slightly different height. The pump pulses of the second stage are adjusted in beam diameter with a 4:1 telescope to match the signal beam diameter and to avoid white light generation in the BBO crystal. To ensure temporal overlap between signal and pump pulses the concave mirror is mounted on a variable translation stage. Across the whole tuning range intense near-infrared pulses with pulse energies of about 80 μJ of combined signal and idler are generated. The signal pulses are continuously tunable between 1.2 μm and 1.6 μm. The corresponding idler pulses range from 2.4 μm to 1.6 μm permitting the generation of small difference frequencies.

These two pulses are separated by a polarising beam splitter and the idler pulses pass a variable translation stage to adjust the temporal delay between them. They are both focused by concave mirrors (R = 1 m) into the 0.5 - 1 mm type I GaSe (or $AgGaS_2$) crystal where their difference frequency is generated. Horizontally polarised mid-infrared pulses tunable between 3 μm and 10 μm are obtained with typical pulse energies of 0.3 - 2.0 μJ depending on the frequency. The pulses are shortest at 5 μm with a duration in the order of 100 fs (FWHM). After the generation of mid-infrared light pulses, residual signal and idler pulses are suppressed by a suitable long wave pass filter.

2.4 Femtosecond ultraviolet light pulses

The femtosecond ultraviolet pump pulses for electronic excitation were generated using noncollinear optical amplification with subsequent sum frequency mixing (SFM). The configuration is shown in Figure 2.4 [Kummrow et al., 2000]. The horizontally polarised fundamental (650 μJ) is split in three beams: the major part of the fundamental (81 %, 527 μJ) is frequency doubled in a 0.5 mm type I BBO crystal providing the pump pulses at 400 nm (135 μJ) for the single-pass noncollinear parametric optical amplifier (NOPA). To achieve a broad amplification bandwidth such a NOPA operates optimal with pulse durations between 100 fs and 150 fs. Given the fact that the Ti:sapphire amplified laser system provides 40 fs pulses a 1 cm quartz plate is introduced into the beam path of the blue pump pulses in order to stretch the pulses in time. A lens (f = 50 cm) focuses the vertically polarised pump pulses in front of the 1 mm type I BBO crystal. The pump intensity can be adjusted by displacement of the nonlinear crystal. The seeding white light continuum is generated by focusing (f = 5 cm) the second smaller part of the fundamental (10 %, 65 μJ) into a 2 mm sapphire plate. For the sake of a stable continuum of good optical quality the pump pulses are attenuated by a combination of half-wave plate and polariser to just above the continuum threshold. The horizontally polarised seed is collimated with a lens (f = 3 cm), focused by a concave mirror (f = 15 cm) and spatially overlapped with the pump beam in the BBO crystal. The angle of about 4° between pump and seed beam inside the crystal is chosen in such a way that the noncollinear phase matching condition is approximately independent from the wavelength and hence very large gain bandwidth is achieved. The part of the fundamental generating the white light passes a variable delay stage which allows to control the optical path length of the different spectral components of the chirped white light in respect to the pump pulses. In this way it is possible to tune the temporal overlap between pump pulses and different frequencies of the white light

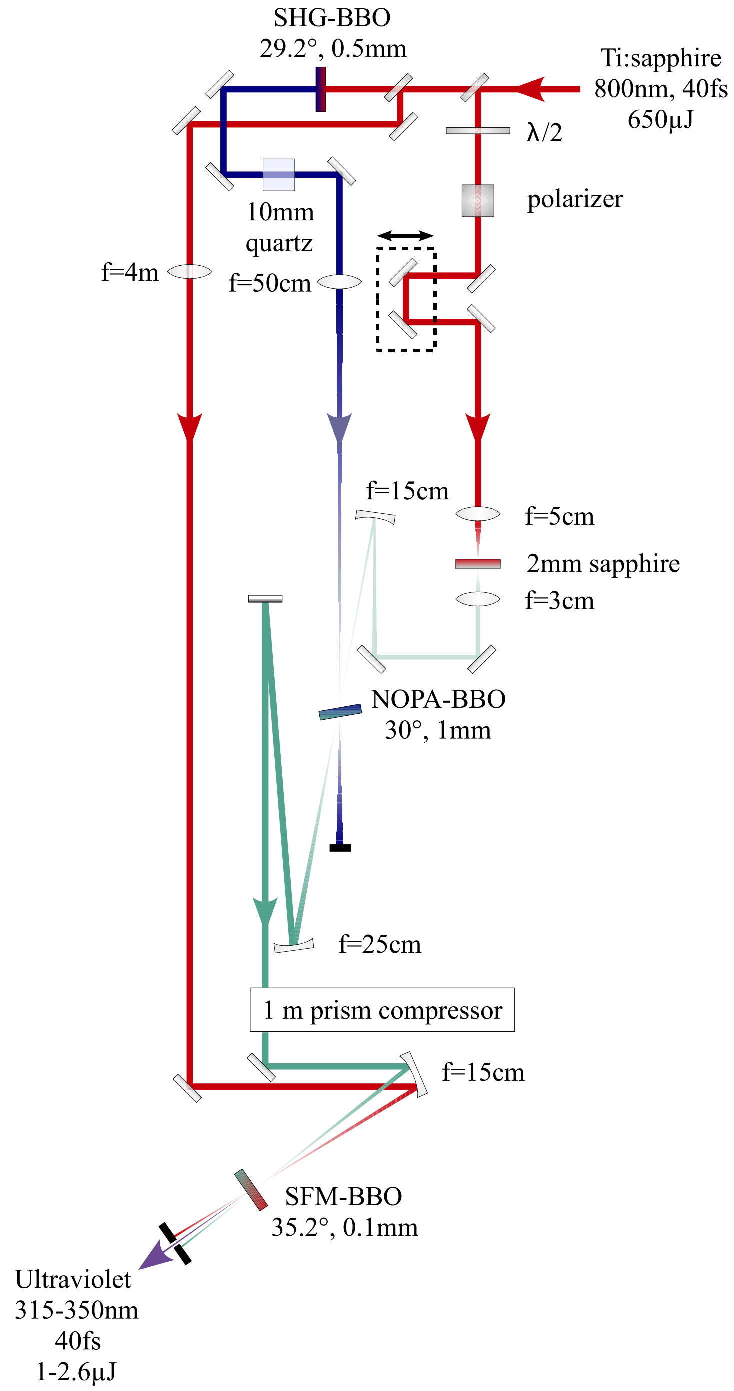

Figure 2.4: Design of the noncollinear optical parametric amplifier and the following sum frequency mixing stage. The beam splitters have 10% reflection. λ/2: half-wave plate.

so that a selected wavelength is amplified. The horizontally polarised visible pulses are collimated with a concave mirror (f = 25 cm) and compressed using a double-pass quartz prism compressor of 1 m length. They are tunable from 490 nm to 660 nm with an energy up to 6 μJ and pulse durations below 35 fs. For the sum frequency mixing the third beam (9 %, 59 μJ) is collimated down by a lens (f = 4 m) and focused together with the visible NOPA pulses into a 100 μm type I BBO crystal with a concave mirror (f = 15 cm). The beam-intersection angle is 1.3°. Vertically polarised UV pulses between 315 nm and 350 nm with energies from 1 μJ to 2.6 μJ and pulse durations of below 40 fs are obtained.

In case of electronic excitation at 400 nm pump pulses are obtained by second harmonic generation (SHG) of the third beam in a 100 μm type I BBO crystal.

2.5 Pump-probe experiments

The pump-probe experimental setup is shown schematically in Figure 2.5. The intense UV pump pulses pass an optical delay line (PI, M-531.DG) in order to vary the time delay between pump and probe pulses up to 1 ns. With the help of a zero-order half-wave plate the polarisation of the pump pulses can be rotated from perpendicular via magic angle (54.74°) to parallel configuration with respect to the polarisation of the probe pulses allowing for polarisation sensitive measurements. Sample transmission with and without electronic excitation is monitored using an optical chopper synchronised to the Q-switch of the CPA pump laser that runs at half the repetition rate of the CPA and therefore blocks every second pump pulse. The pump beam is focused by a lens (f = 20 cm) in such a way that the sample is placed before the focal plane and the beam diameter is about 200 - 250 μm at the sample position in order to minimise non-resonant signal contributions due to solvent and sample cell window material. The mid-infrared light originating from the BBO OPA with subsequent difference frequency mixing stage is split into two weak beams which are used as probe and reference beam, respectively. This is realised by a ZnSe wedge which shows reflections from its front and its back surface, each reflection has an energy of 10 % of the incoming beam. The major part of the mid-infrared light is transmitted through the wedge and blocked. Both probe and reference pulses pass a 2:3-reflection telescope to enlarge their beam diameter which results in a reduction of the focal spot size to 100 - 150 μm in the sample. This ensures that a homogeneously pumped volume is being probed. The probe and reference pulses are focused by a 30° off-axis parabolic mirror into the sample where pump and probe pulses spatially overlap whereas the reference pulses propagate through a nearby sample volume that is not perturbed by the pump pulses. After the sample the pump pulses are blocked whereas the remaining two pulses are collimated by a second 30° off-axis parabolic mirror and focused onto the entrance slit of a monochromator. Depending on the central wavelength of the mid-infrared light gratings with 300 lines/mm (3 - 5 μm), 100 lines/mm (5 - 7.5 μm) and 60 lines/mm (7.5 - 10 μm) are used in order to spectrally disperse the pulses. The resulting spectral resolution depends on the spectral range, to give some examples: 5.6 cm^{-1} for 3.5 μm, 7.2 cm^{-1} for 6 μm and 2.9 cm^{-1} for 9 μm. The intensity of each spectral component of the probe as well as the reference pulses is then recorded with a double array of 31 infrared sensitive mercury cadmium telluride detector elements (MCTs). The MCTs act as photoresistors whose resistance decreases

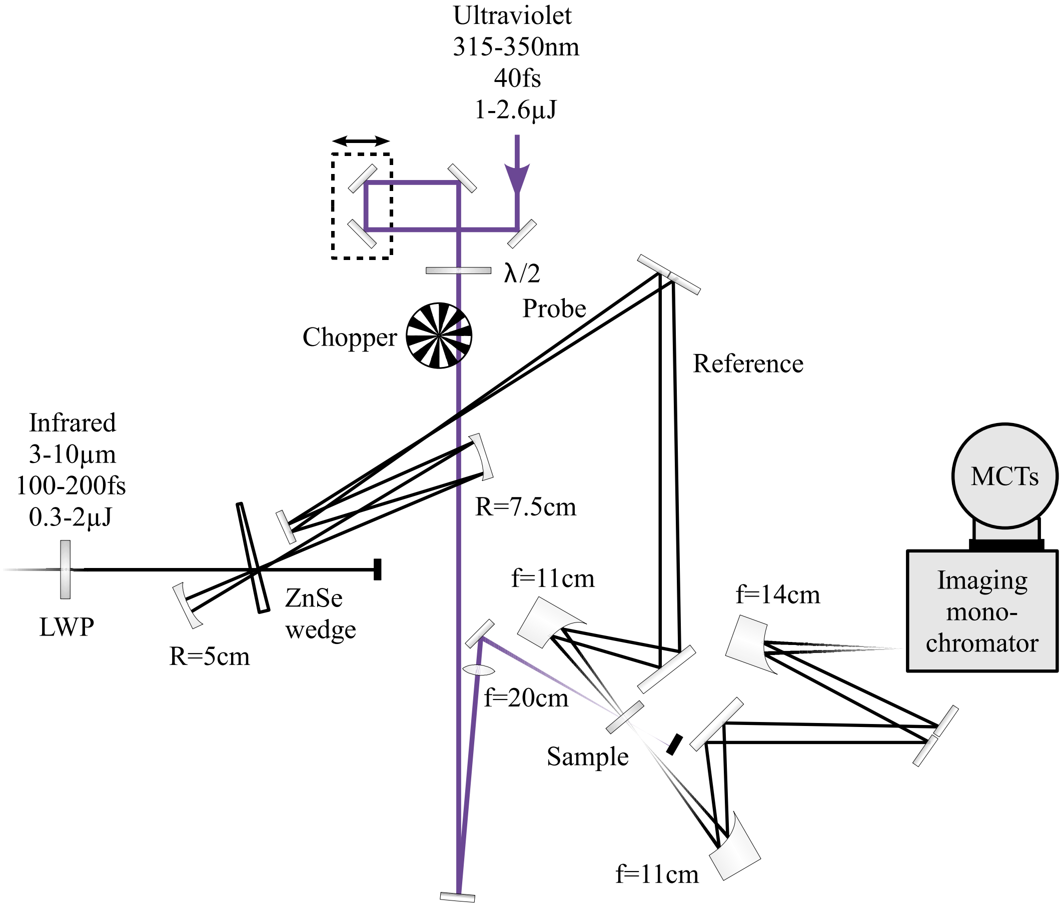

Figure 2.5: Design of the pump-probe setup. Note that the reference pulses propagate through a sample volume which is not excited. The generated third-order signal is collinear to the probe pulses. LWP: long wave pass filter, λ/2: half-wave plate.

with increasing incident mid-infrared light intensity. The change of the bias current due to absorption of mid-infrared photons is integrated by gated electronics that are synchronised to the CPA repetition rate. The signal is sampled by a fast 16-bit Analog-to-Digital converter (Keithley Instruments, DAS-1801-HC) for multi-channel single shot data acquisition which serves to convert the input analog voltage to a digital signal. Introducing the reference pulses into the detection scheme compensates for intensity fluctuations of the probe pulses on a single shot basis which results in an improved signal-to-noise ratio. Absorbance changes as small as 10^{-4} can be readily detected. The transient absorbance change is calculated normalising with respect to the transmitted reference pulses and comparing on two subsequent shots the excited with the unexcited case (index 0):

$$\Delta A(t,\omega) = -\log_{10}\left[\left(\frac{I(t,\omega)}{I_0(\omega)}\right)_{probe} \cdot \left(\frac{I_0(\omega)}{I(\omega)}\right)_{reference}\right]. \tag{2.6}$$

Because of the large bandwidth of short pulses it is crucial to avoid dispersion effects during propagation. Therefore mainly reflective optics are employed except for the ZnSe wedge and the long wave pass filter. In order to avoid spectral and temporal distortion of the mid-infrared pulses in case their spectrum overlaps with water or carbon dioxide absorption lines (Figure 2.6), the experimental setup is enclosed in a box and purged with nitrogen. A peristaltic pump is used to circulate the sample through a flow cell (1 mm thick BaF_2 windows separated by teflon spacer variable in thickness), to guarantee that a new sample volume is excited for every laser shot. All measurements presented in this thesis have been performed at room temperature, $T = 22.5 \pm 0.5$°C. The time

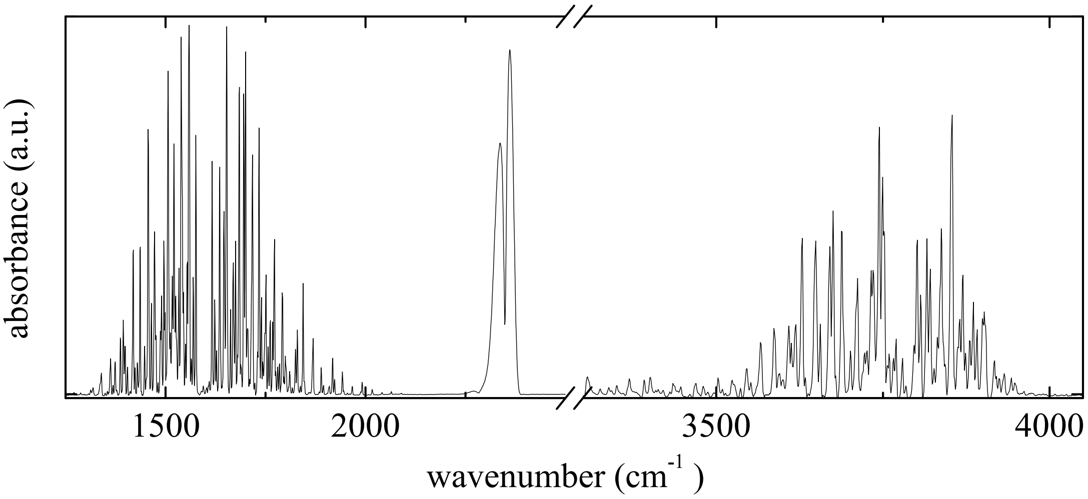

Figure 2.6: Absorbance of air at room temperature in the mid-infrared spectral range. The bending and the symmetric/asymmetric stretching vibrations of water vapor are centred around 1600 cm^{-1} and 3750 cm^{-1}, respectively. The vibrations exhibit a rotational fine structure. Absorption around 2349 cm^{-1} is due to the strong IR-active asymmetric stretching vibration of CO_2 showing rotational fine structure.

zero delay as well as the time resolution of the experimental setup is determined by means of a spectrally resolved cross correlation measurement. A 1 mm thin piece of ZnSe semiconductor is used because of its appropriate non-linear optical properties. Interaction with the UV pump pulses creates instantaneously an electron-hole plasma which can be probed with mid-infrared pulses. The observed signal $S(\tau)$ depends on the delay time τ and is given by the temporal convolution of the response function of ZnSe, $R(t)$, with the second order intensity cross correlation function $G(t)$ between the pump and the probe pulse:

$$S(\tau) \ = \ \int_{-\infty}^{\infty} R(t-\tau)G(t)dt. \tag{2.7}$$

The resonse function can be described with the Heaviside step function $\xi(t)$, $R(t) = \xi(t)$, with $\xi(t) = 0$ for $t < 0$ and $\xi(t) = 1$ for $t \geq 0$. Such a measurement is shown in Figure 2.7 for a UV pump pulse at 330 nm and an infrared pulse centered at 1500 cm^{-1}. The time resolution (FWHM) for the UV pump/mid-infrared probe experiment depends on the probe frequency which is 150 fs at this particular frequency. Throughout the accessible mid-infrared spectral range from 1000 cm^{-1} to 3300 cm^{-1} the typical time resolution lies between 100 and 250 fs, e.g. 250 fs at 1000 cm^{-1}, 100 fs at 2000 cm^{-1} and 150 fs at 3000 cm^{-1}.

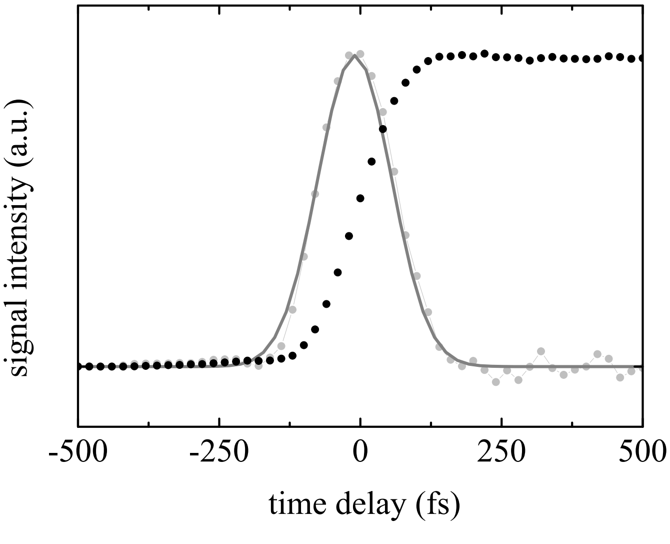

Figure 2.7: Pump-probe signal (black dots) of a cross correlation measurement in ZnSe for infrared pulses centered at 1500 cm^{-1}, corresponding to a time resolution of 150 fs. Its time derivative is shown as a grey line with circles and the fit of this Gaussian shape function is shown as a plain line.

3 Ultrafast polarisation-sensitive UV-pump/IR-probe spectroscopy

Optical spectroscopy is a powerful tool to study matter and its interactions. It exploits the macroscopic optical polarisation of the medium under study. Section 2.2 introduced the field-induced polarisation: the first-order polarisation $P_i^{(1)}(\omega, t)$ gives rise to linear absorption spectroscopy which contains information on the properties of the quantum mechanical object. However, linear spectroscopy only provides information averaged over all time scales. Multiple interactions between the system and electric fields generates a nonlinear response of the system allowing for an understanding of molecular dynamics, coupling mechanisms and transient structures at well-defined time scales.

3.1 Pump-probe spectroscopy

In pump-probe spectroscopy [Mukamel, 1995; Nibbering, 2005] the system interacts with the electric fields of two laser pulses in such a way that it interacts twice with the strong pump pulse E_{pump} and once with the delayed weak probe pulse E_{probe} thereby inducing a third-order polarisation $P_i^{(3)}(\omega, t)$. All electric fields propagate along specific directions that are specified by their respective wavevector $\mathbf{k}$:

$$E(t) = E_0(t)(\mathrm{e}^{-i\omega t + i\mathbf{k}r} + \mathrm{e}^{+i\omega t - i\mathbf{k}r}). \tag{3.1}$$

In general, the wavevector of the signal field $\mathbf{k}_{signal}$ is given by the sum of the wavevectors of the generating fields according to :

$$\mathbf{k}_{signal} = \pm\mathbf{k}_1 \pm \mathbf{k}_2 \pm \mathbf{k}_3. \tag{3.2}$$

As a result of the two interactions of the sample with the pump pulse with wavevectors $+\mathbf{k}_{pump}$ and $-\mathbf{k}_{pump}$ and one interaction with the probe pulse with wavevector $+\mathbf{k}_{probe}$, an electric field E_{signal} will be emitted in the same direction as the probe pulse (Figure 3.1). Both electric fields, E_{probe} and E_{signal}, are either interfered on a single detector

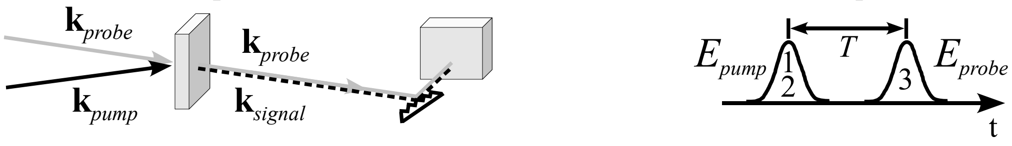

Figure 3.1: Geometry of electric fields represented by their $\mathbf{k}$-wavevectors in pump-probe spectroscopy.

or spectrally dispersed by an optical grating. The spectral components can then be interfered on an array of detection devices or one can scan the monochromator using a single detector. The pump-probe signal is self-heterodyne detected as it interferes with the probe pulse which acts as a local oscillator. Considering the time ordering between the interactions, the rotating wave approximation and the phase matching condition the total pump-probe response for a three-level system can be represented with six so-called Feynman diagrams as shown in Figure 3.2. In principle time ordering between the interactions is possible if the laser pulses are short compared to the time separation between them. In the following, time ordering between pump and probe pulse, the probe pulse being the last interaction with the system, is assumed. The diagrams on the left describe those molecules which are in the ground state after the interactions with the pump pulse and thus represent bleach contribution. The diagrams in the middle represent stimulated emission. The system is promoted to the excited state by the pump pulse and stimulated back to the ground state by the probe pulse. The diagrams on the right represent excited state absorption. The system is promoted to the first excited state by the pump pulse and the second excited state is probed by the probe pulse. Note that the difference between the top and the bottom diagrams is the time ordering between the first two interactions with the pump pulse. Since the time between these two interactions, τ, is assumed to be zero these two diagrams give the same nonlinear response.

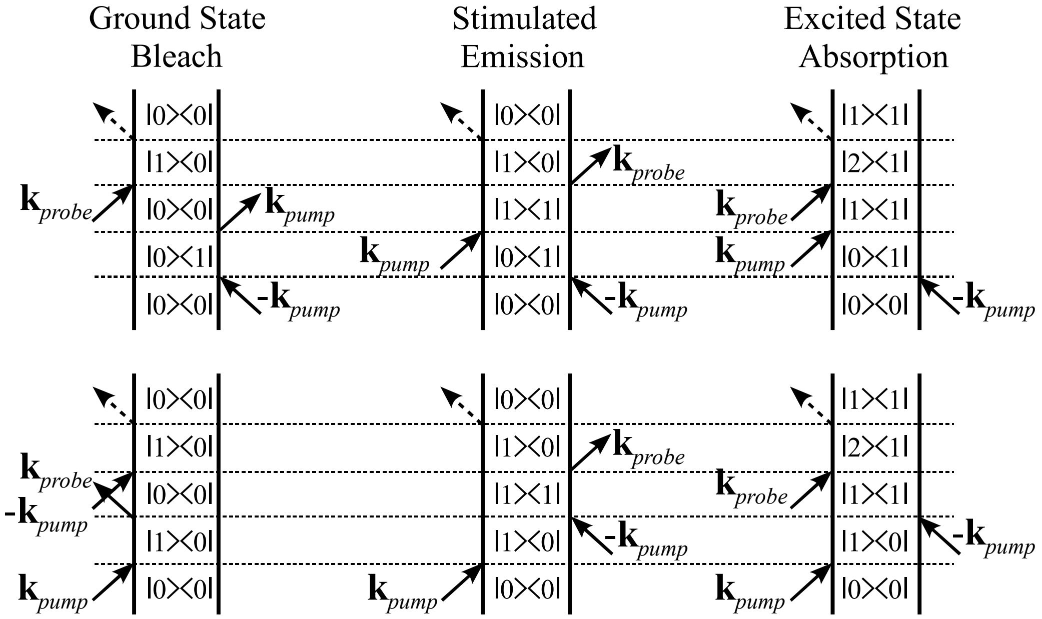

Figure 3.2: Six Feynman diagrams representing the contributions to the pump-probe signal of a three-level system.

Variations of the temporal delay T between pump and probe pulses allow to monitor the transient transmission changes due to the optically triggered processes. In the case that the emitted electric field is weak compared to the probe pulse, the spectrally integrated transmission change is given by:

$$\Delta \mathrm{T}(T,\omega) = \frac{I(T,\omega)}{I_0(\omega)} = \frac{\int_0^\infty dt|E_{probe}(\omega) + E_{signal}(T,\omega)|^2}{\int_0^\infty dt|E_{probe}(\omega)|^2}$$
$$\approx 1 + \frac{2\int_0^\infty dt\Re\{E_{probe}(\omega)E^*_{signal}(T,\omega)\}}{\int_0^\infty dt|E_{probe}(\omega)|^2}. \quad (3.3)$$

Since the detector is slow compared to the duration of the femtosecond light pulses, the detected signal is proportional to the time integral of the light intensity. $\Re$ denotes the real part of a complex number. The response function of a homogeneously broadened oscillator with a linewidth Γ is given by:

$$S^{(3)}(\tau=0,T=0,t) = \left(4\frac{i}{\hbar^3}\mu_{10}^4 \mathrm{e}^{-i\omega_{10}t} - 2\frac{i}{\hbar^2}\mu_{10}^2\mu_{21}^2\mathrm{e}^{-i\omega_{21}t}\right)\mathrm{e}^{-\Gamma t}, \quad (3.4)$$

with the transition dipole moments μ_{10} and μ_{21} and transition frequencies ω_{10} and ω_{21}. In the semi-impulsive limit - the laser pulses are short compared to the system response but long compared to the light oscillation period - the third-order polarisation is equal to the third-order response function, $P^{(3)}(t,T,\tau) = S^{(3)}(t,T,\tau)$. In case a spectrometer performs a Fourier transform of the fields with respect to time t, the pump-probe spectrum is of Lorentzian shape:

$$\Delta A(T,\omega) \propto -\frac{8\mu_{01}^4\Gamma}{(\omega_{10}-\omega)^2+\Gamma^2} + \frac{4\mu_{01}^2\mu_{21}^2\Gamma}{(\omega_{21}-\omega)^2+\Gamma^2}. \quad (3.5)$$

The negative term is the sum of ground state bleach and stimulated emission and the positive one is the excited state absorption.
When the time ordering is reversed ($T < 0$), first the system interacts with the probe pulse and then twice with the pump pulse, a signal will be generated which is named perturbed free induction decay [Hamm, 1995]. The infrared probe pulse resonantly excites a coherent polarisation which decays with its dephasing time. As a result, radiated light, known as free induction decay, is recorded along with the probe pulse. The interaction of the pump pulse might modify the strength and position of the ground state vibrational band. This affects the probe-induced free induction decay. Other contributions arise during pulse overlap between pump and probe pulses which are referred to as “coherent artifact” [Boyd, 1993].

3.2 Effects of anharmonicity and energy transfer

Besides translational and rotational degrees of freedom, a polyatomic molecule with N atoms has $3N-6$ ($3N-5$ for linear molecules) vibrational degrees of freedom. Usually polyatomic molecules are treated in the harmonic oscillator approximation, where only quadratic terms are included in the molecular potential energy function giving rise to independent vibrational normal modes. As a consequence any vibrational motion can be represented as a superposition of normal modes and the total vibrational eigenfunction is a product of oscillator eigenfunctions corresponding to these different normal modes.

However, the molecular potential energy function contains cubic, quartic and higher order terms in every single vibrational coordinate leading to anharmonicity effects that cannot be neglected. Anharmonicity is typically treated as perturbation to the Hamiltonian in the eigenstate representation of the harmonic oscillator normal modes. The Schrödinger equation then no longer resolves into a number of independent equations for each normal mode, the total energy is no longer the sum of eigenvalues but it contains cross-terms involving two or even more normal vibrations [Herzberg, 1945]. In the following the formalism of anharmonicity shall be briefly reviewed [Hamm et al., 1997]:

The vibrational levels of a molecule including anharmonic corrections can be expressed as:

$$\frac{E(v_1, v_2, v_3, ...)}{\hbar} = \sum_i \omega_i \left(v_i + 1/2\right) + \sum_{i \leq j} x_{ij} \left(v_i + 1/2\right) \left(v_j + 1/2\right) \tag{3.6}$$

with the harmonic frequency of the $i-th$ vibrational mode, ω_i, the vibrational quantum number of the $i-th$ vibrational mode, $v_i = 0, 1, 2...$, and the anharmonicity constants x_{ij}. The anharmonicity constants can be derived from the cubic and quartic force constants in a normal coordinate basis. A given vibrational mode k is coupled to the bath of the remaining modes $i \neq k$. Its transition frequency is given by:

$$\omega(v_k \rightarrow v_k + 1) = \omega_k + 2x_{kk}v_k + \sum_{i \neq k} x_{ik}v_i \tag{3.7}$$

where the first term is the anharmonic correction of the $v_k = 0 \rightarrow v_k = 1$ transition in the vibrational ground state:

$$\omega_k = \omega_k^0 + 2x_{kk} + \sum_{i \neq k} x_{ik}/2. \tag{3.8}$$

The second term of (3.7) describes the “diagonal" anharmonic shifts of an excited vibrational mode k, while the third term describes the frequency shifts due to the “off-diagonal" anharmonicity between the selected mode k and the remaining bath modes. Two kinds of anharmonic effects are particularly important in order to extract information from the measured transient vibrational spectra:

(i) Diagonal anharmonicity: Contrary to harmonic oscillators with an equidistant energy between vibrational levels for anharmonic oscillators the energy spacing between vibrational levels becomes smaller as the vibrational quantum number increases. The resulting frequency shifts are responsible for detectable difference absorbance bands.

(ii) Off-diagonal anharmonicity: When the molecule has a large internal vibrational energy that is redistributed over the whole molecule low frequency vibrational modes are highly excited. Anharmonic coupling to the monitored marker mode affects its frequency position as well as its lineshape. Examination of the temporal evolution of band frequency and width reveal information about the time scales of processes such as intramolecular vibrational redistribution (IVR) and intermolecular energy transfer.

An expression that models the line shape of an absorption line $A_k(\omega)$ of one selected vibrational mode k can be obtained by applying the "Golden Rule":

$$\begin{aligned} A_k(\omega) \propto \sum_{v_k} \Bigg\{ &(\alpha(v_k) - \alpha(v_k+1))(v_k+1) \\ &\times \sum_{v_1,\ldots v_m} \left[\left(\prod_{i \neq k} \alpha(v_i) \right) \times \delta \left(\omega - \omega_k - 2x_{kk}v_k - \sum_{i \neq k} x_{ik}v_i \right) \right] \Bigg\}. \end{aligned} \tag{3.9}$$

$\alpha(v_k)$ is a given population distribution function of the mode k with normalisation $\sum_{v_k} = 1$. δ is the delta function which can be replaced by a line shape function with finite bandwidth. The first term $+\alpha_{v_k}$ describes the absorption between the states $v_k \rightarrow v_k+1$, while the second term $-\alpha(v_k+1)$ takes into account the stimulated emission $v_k+1 \rightarrow v_k$. The effect of the off-diagonal anharmonic coupling to vibrationally excited bath modes on the lineshape is taken into account over all vibrational modes $i \neq k$ in all possible quantum levels $v_{1,\ldots m}$, each permutation weighted by its probability $\prod_{i \neq k} \alpha(v_i)$.

Anharmonic coupling to highly excited modes

Using the briefly reviewed formalism, a temperature dependent absorption lineshape of the antisymmetric cyano-stretching vibrations of tetracyanoethene which will be used in section 4.2 has been simulated by J. Dreyer. First, geometry optimisation and harmonic normal mode calculations of tetracyanoethene were performed using density functional theory (DFT) with the B3LYP functional (aug-cc-pvdz) as implemented in Gaussian 03 [Frisch et al., 1998]. The coupling to low-frequency modes was implemented by Taylor expansion of the potential energy V in the dimensionless coordinates of the normal modes. The expansion was performed with respect to the equilibrium geometry and was truncated after fourth order. The latter was restricted to semi-diagonal quartic force constants:

$$V = \frac{1}{2}\sum_{i}^{N} \omega_i q_i^2 + \frac{1}{6}\sum_{i,j,k}^{N} \Phi_{ijk} q_i q_j q_k + \frac{1}{24}\sum_{i,j,k}^{N} \Phi_{ijkk} q_i q_j q_k^2 \,, \qquad \Phi_{ijk\ldots} = \frac{\partial^n V}{\partial q_i \partial q_j \partial q_k \ldots} \,.$$

The harmonic frequencies ω_i and the higher order force constants are the corresponding derivatives evaluated at the equilibrium point. The higher order force constants were calculated numerically by three-point finite differences as proposed by Schneider and Thiel [Schneider and Thiel, 1989] and used previously [Dreyer, 2005, 2007]. Anharmonic constants x_{ij} were derived from the cubic and semidiagonal quartic force constants according to standard procedures [Nielsen, 1951; Willetts and Handy, 1995; Handy and Willetts, 1997]. A thermal Boltzmann distribution for the population distribution functions $\alpha(v_i)$ for the intramolecular bath modes was assumed for all temperatures. Since the absorption lineshape function includes all possible transition frequencies originating from the off-diagonal anharmonic coupling to all excited vibrational modes weighted by the population factors of their respective levels, the anharmonic shifts of the simulated vibrational mode is temperature dependent. Each transition line was convoluted with a Gaussian function of 4 cm^{-1} FWHM. The results for the cyano-stretching mode at 2329 cm^{-1} (ν_{23}) are shown in Figure 3.3 which is qualitatively similar to the mode at

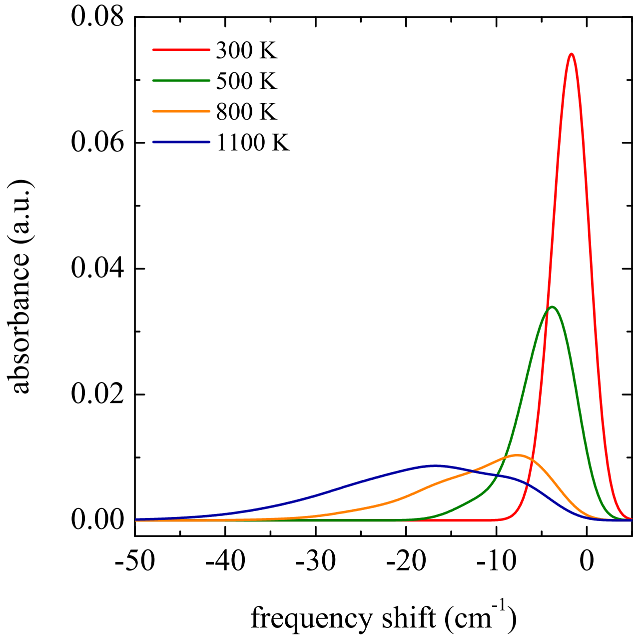

Figure 3.3: Simulated absorption spectrum of the ν_{23} mode of tetracyanoethylene at different temperatures. Frequency shifts are plotted relative to the frequency at 0 K.

2349 cm^{-1} (ν_{24}). At room temperature, only a minor frequency shift of 1.7 cm^{-1} with respect to the zero-temperature position is observed. With increasing temperature the frequency shift becomes more pronounced (about 17 cm^{-1} at 1100 K) and the band exhibits a strong asymmetric broadening. The red-shift as a function of temperature is caused by the anharmonic constants $x_{i,23}$ being mostly negative. The main contribution to the anharmonic effects is due to the off-diagonal anharmonic constants x_{ij}, $i \neq j$, and not due to the diagonal term x_{jj}. Even at 1100 K, the excitation probability of the ν_{23} mode is negligible and the diagonal harmonic constant ($x_{23,23}$ = -2.98 cm^{-1}) is small as compared to the sum of the off-diagonal elements of all low-frequency modes ($\sum x_{i,23}$ = -45.06 cm^{-1}), which are excited considerably at this temperature. Therefore, these modes are responsible for the anharmonic effect determining the reshaping of the ν_{23} absorption band.

3.3 Principles of polarisation-sensitive spectroscopy

In polarisation-sensitive UV-pump/IR-probe measurements linearly polarised light is used for both UV pump and infrared probe pulses. As a consequence, those molecules are preferentially excited with an electronic transition dipole moment parallel to the polarisation of the incoming field. This leads to a selective photoexcitation of a specific orientation of the electronic transition dipole from a disordered ensemble of transition dipoles. The infrared probe pulses interact with vibrational transitions of either the chromophore or its reaction partner. Depending on the polarisation configuration between pump and probe pulses two pump-probe signals are measured:

$$\Delta A(t,\omega)_{\|} = -\log_{10}\left(\frac{I(t,\omega)}{I_0(\omega)}\right)_{\|} \quad \text{and} \quad \Delta A(t,\omega)_{\perp} = -\log_{10}\left(\frac{I(t,\omega)}{I_0(\omega)}\right)_{\perp} \tag{3.10}$$

with an index indicating that both pulses are polarised along the same direction, ∥, or in different directions that are perpendicular to each other, ⊥. From geometric considerations it is possible to determine the angle between the electronic transition dipole moment μ_{el} and the vibrational transition dipole moment μ_{vib} from the initial anisotropy of the pump-probe signal when probing a vibrational transition of the chromophore after its excitation. The same treatment can be applied for a reactive complex of two reactants with a preferred mutual orientation. In other words, as long as spectroscopic transitions for both reaction partners are polarised along specific directions in the molecular frame it is possible to determine the mutual orientation of the reaction partners. Since rotational diffusional motions of the molecules randomise the orientation of the photoselected molecule, the measurement has to be performed on a time scale that is fast compared to rotational diffusion which is in the order of 20 ps for the molecules studied within the scope of this thesis. As a result, structural determination of reactive complexes requires femtosecond time resolution.

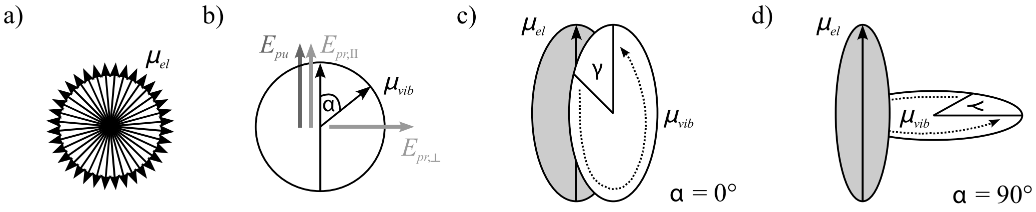

Figure 3.4: Schematic presentation of a) a disordered ensemble of electronic transition dipole moments μ_{el}, b) selective photoexcitation of a molecule with transition dipole moments μ_{el} and μ_{vib} enclosing α as well as the polarisation configuration between pump and probe pulses. c) and d) indicate limiting cases for the mutual orientation of two aromatic molecules and their respective transition dipole moments.

The time-dependent rotational anisotropy is given by [Fleming, 1986]:

$$r(t) = \frac{\Delta A(t,\omega)_{\|} - \Delta A(t,\omega)_{\perp}}{\Delta A(t,\omega)_{\|} + 2\Delta A(t,\omega)_{\perp}}. \tag{3.11}$$

The following expression can be used to derive structural information on the chromophore, or more general, for any system with the transition moments μ_{el} and μ_{vib} enclosing one specific angle α:

$$r(\alpha) = \frac{3\cos^2\alpha - 1}{5} \tag{3.12}$$

which results for instance in $r(0°) = 0.4$, $r(90°) = -0.2$ or $r(45°) = 0.1$.

For a reactive complex of two aromatic molecules, however, an additional degree of freedom between the transition dipoles has to be considered. The molecules might be arranged in a sandwich-like geometry - the planes parallel to each other - or in the other extreme they can be oriented in such a way that the two planes are perpendicular to each other (Figure 3.4 c) and d)). In between, the angle α can adopt any value. In addition, the probed vibrational transition dipole moment might be randomly oriented within the plane of the molecule. In such a case the following expression relates the measured anisotropy to the angle α:

$$r(\alpha) = \frac{3\cos^2\alpha - 2}{10}. \tag{3.13}$$

The two mentioned extreme cases $\alpha = 0°$ and $\alpha = 90°$ yield r = 0.1 and r = -0.2, respectively.

As the rotational diffusion and the investigated bimolecular charge transfer dynamics occur on comparable time scales it is important to measure the pump-probe signal unaffected by orientational factors. This can easily be achieved by performing the measurements for which the probe beam is polarised at the magic angle (54.74°) relative to the pump beam polarisation.

4 Bimolecular Electron Transfer

Although photoinduced bimolecular electron transfer reactions have been extensively investigated during the past 40 years [Weller, 1982; Gould and Farid, 1996; Mataga et al., 2005], there are still several open issues [Vauthey, 2006]. One concerns over the nature and structure of the primary product of the charge separation process and the ensuing species. Tight ion pairs (TIPs)* and loose ion pairs (LIPs)† are introduced to refer to different structures involved in the photochemical process [Masnovi and Kochi, 1985; Kavarnos and Turro, 1986; Asahi and Mataga, 1989; Kikuchi et al., 1991; Gould et al., 1991; Peters and Lee, 1992; Zhou et al., 2002]. The concept of different kinds of ion pairs goes back to Winstein and Fainberg who worked on salt effects in solvolysis during the early fifties [Winstein et al., 1954]. The difference between these two species is supposed to be the interionic distance which is short for TIPs and long for LIPs. For TIPs composed of aromatic molecules, Weller assumed that ions are orientated face-to-face with an interplanar separation of about 3 Å[Weller, 1982]. Such a short distance of face-to-face ions results in a substantial overlap of molecular orbitals of the ion pairs‘ constituents. This assumption is supported by experimental observation, showing that TIPs can exhibit charge transfer (CT) emission [Gould et al., 1991; Kikuchi et al., 1990; Kuzmin, 1996; Muller et al., 2000]. A finite transition dipole moment for charge transfer emission requires spatial overlap of the singly occupied molecular orbitals of the ions and thus the interionic distance can be assumed to be significantly short. Such TIPs can be seen as exciplexes with very large charge transfer character. They can be directly formed upon photoexcitation of the charge transfer band of donor-acceptor complexes [Gould and Farid, 1996; Asahi and Mataga, 1989; Goodman and Peters, 1985; Asahi and Mataga, 1991]. The structure of LIPs is more elusive in nature. Different views on the structure of LIPs can be found in the literature. Some authors assume that LIPs have a precise structure with a typical interionic distance of 7 - 8 Å[Gould and Farid, 1996; Masnovi and Kochi, 1985; Kavarnos and Turro, 1986; Peters and Lee, 1992]. This allows to define specific time constants for ion pair formation, dissociation into free ions and charge recombination. Other authors think of LIPs more like diffusing ions with a distribution of interionic distances ranging from 7 Å to 12 Å[Kakitani et al., 1992; Tachiya and Murata, 1992; Burshtein, 2000; Zhong et al., 2004]. As a result, an accurate description of the time evolution of the ion pair population requires a non-Markovian approach [Burshtein, 2000]. According to the hypothesis accounting for the absence of the inverted regime for bimolecular photoinduced charge separation reactions, TIPs are formed upon weakly exergonic charge separation whereas LIPs are the primary products of highly exergonic charge separation [Masnovi and Kochi, 1985; Kavarnos and Turro, 1986; Asahi and Mataga, 1989; Kikuchi et al., 1991; Gould et al., 1991; Peters and Lee, 1992; Zhou et al., 2002]. Solvation and desolvation processes allow any kind of reactive complex to rearrange to another before charge separation. Similarly,

---

*also named contact or intimate ion pairs

†also dubbed solvent-separated or solvent-shared ion pairs

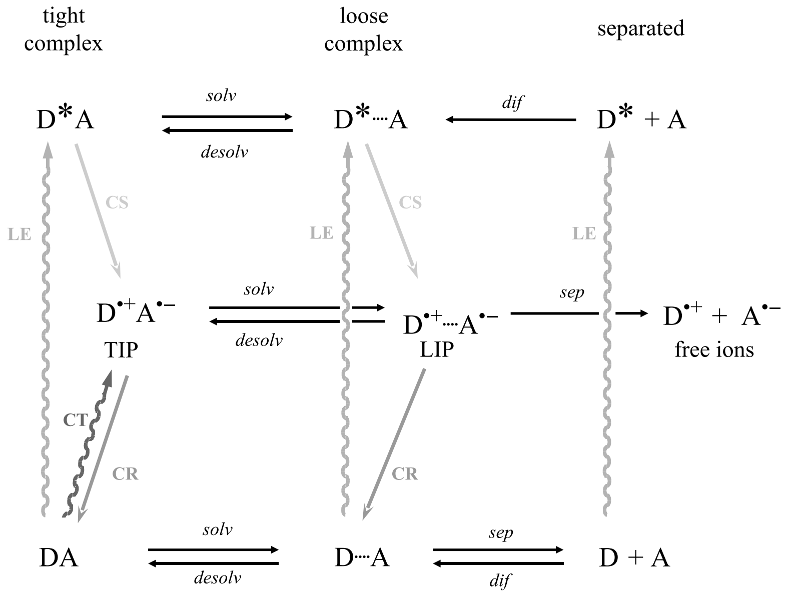

Figure 4.1: General scheme for bimolecular ET reaction between donor D and acceptor A. Solid arrows indicate charge separation (CS), charge recombination (CR), and molecular diffusion. Photoinduced local excitation (LE) to the S_1 state of the donor D^* and charge transfer (CT) excitation of a ground-state complex DA to TIPs are indicated by wavy lines.

before charge recombination TIPs can rearrange into LIPs and *vice versa* (Figure 4.1). Based on the absence of exciplex emission at higher exergonicities, Kikuchi proposed an exergonicity of ΔG^0_{CS} = -0.4 eV as an empirical point of change between the regime of on-contact vs. through-solvent electron transfer [Kikuchi et al., 1990, 1991]. For exergonicities $\Delta G^0_{\mathrm{CS}} < -0.4$ eV charge separation takes place at contact distance and TIPs are formed whereas for $\Delta G^0_{\mathrm{CS}} > -0.4$ eV, the reaction occurs at greater distances and LIPs are generated. This threshold value is often cited to justify the nature of photogenerated ion pairs. However, since charge recombination of TIPs is ultrafast the observation of charge transfer fluorescence might be prevented [Asahi and Mataga, 1989; Nicolet and Vauthey, 2002; Nicolet et al., 2005]. Therefore, the absence of charge transfer emission in highly exergonic charge separation reactions is no adequate evidence of long-distance charge separation which results in the formation of LIPs. Indeed, Nicolet *et al.* observed a substantial heavy-atom effect on the intersystem crossing yield of a radical ion pair formed upon electron transfer reaction with a driving force as large as -0.61 eV [Nicolet and Vauthey, 2003]. As for spin-orbit coupling, the mechanism for the intersystem crossing, is only operative for strongly coupled ion pairs, the threshold value of -0.4 eV is at least underestimated. Further studies of charge recombination dynamics of ion pairs formed upon bimolecular charge separation quenching obtained by the same group using ultrafast spectroscopic techniques are in contradiction with the driving-force dependent ET distance model [Vauthey, 2000, 2001; Pagés et al., 2004]. For example, charge recombination dynamics of ion pairs formed upon highly exergonic bimolecular charge separation reactions were found to be ultrafast [Vauthey, 2001; Pagés et al., 2004] indicative of TIPs and not LIPs as expected. A substantial steric effect has been observed in the charge recombination rate constant of ion pairs revealing that, although highly exergonic, the charge recombination dynamics was slowed down upon increasing the interionic distance. These recent investigations arise the question after the origin of the driving-force dependent ET distance model: the pioneering experiments which lead to its foundation go back to Mataga and co-workers who performed the time-resolved experiments with different time resolutions [Mataga et al., 1988; Asahi and Mataga, 1991]. They found that the driving force dependence of the dynamics of charge recombination is different for ion pairs generated upon bimolecular quenching and for direct charge transfer excitation of donor-acceptor complexes. In the first case, a bell-shaped free energy gap law was found whereas an exponential free energy gap law was observed for the latter. Please note that the charge recombination constant has been extracted from transient absorption measurements with a time resolution of 20 - 40 ps in case of local excitation of the chromophores compared to a much higher time resolution of about 250 - 500 fs in case of charge transfer excitation. These results point to a reinvestigation of photoinduced bimolecular ET reactions with ultrafast spectroscopy.

4.1 Observation of tight & loose ion pairs

To study ion pair formation, 3-methylperylene (MePer) acting as electron donor and the strong electron acceptor tetracyanoethene (TCNE) were chosen. Both solvents, polar acetonitrile (ACN) and weakly polar dichloromethane (DCM) have been used. The exergonicity of the photoinduced charge separation between MePer and TCNE in ACN and DCM has been calculated using (1.52) and the resulting energy diagram for the photoinduced ET reaction along with the parameters is shown in Figure 4.2. The high reduction potential of TCNE and the relatively low oxidation potential of MePer result in a highly exergonic charge separation reaction (ΔG^0_{CS} = -2.25 eV in ACN and ΔG^0_{CS} = -2.05 eV in DCM) which allows for the examination of the Marcus inverted regime. The difference between the exergonicities in ACN and DCM turns out to be small because of

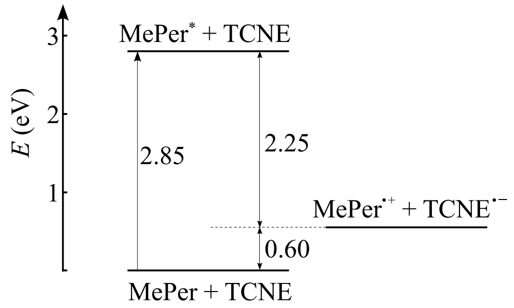

Figure 4.2: Energy diagram for the photoinduced charge separation between MePer and TCNE in ACN. Parameters for the calculation: $E(\mathrm{TCNE}^0|\mathrm{TCNE}^{\bullet -}) = 0.24$ V vs. SCE [Ganesan et al., 2003], $E(\mathrm{MePer}^{\bullet +}|\mathrm{MePer}^0) = 0.85$ V vs. SCE [Mataga et al., 1988], $E(\mathrm{S}_1, \mathrm{MePer}) = 2.85$ eV, ionic radii of 3 Å.

the compensation of the smaller solvation energy by a larger Coulomb interaction when comparing DCM to ACN. It is because of this larger Coulomb interaction that generation of LIPs and ion pair separation can be discarded in the case of DCM as solvent. Stationary absorption spectra of MePer in ACN with different TCNE concentrations are shown in Figure 4.3. The structured band around 400 nm is due to the local S_0-S_1 transition of MePer whereas the broad featureless band centred at 840 nm growing in with increasing TCNE concentration is due to a charge transfer transition of a donor-acceptor complex (DAC). Visible transient absorption (VIS-TA) [Duvanel et al., 2007], fluorescence up-conversion [Morandeira et al., 2002] and photoconductivity [Vauthey et al., 1993; von Raumer et al., 1997; Henseler and Vauthey, 1995] measurements have been performed by O. F. Mohammed and N. Banerji [Mohammed et al., 2008]. Figure 4.4 depicts a series of visible transient absorption spectra at various time delays after local excitation of MePer with 0.1 M and 0.9 M TCNE in ACN. The broad band centred at 700 nm can be assigned to the excited state absorption of MePer (S_1-S_n), while the negative and structured band below 530 nm is due to stimulated emission from the S_1-state. If no quencher is added both signals are present and the decay on a nanosecond timescale is in agreement with the fluorescence lifetime of 3.7 ns reported for MePer in toluene [Morandeira et al., 2003]. In the presence of TCNE as quencher, the decay of the MePer excited state population is much faster [‡]. Moreover, an additional band centred at 543 nm due to the D_0-D_5 transition of the MePer radical cation, $MePer^{\bullet+}$, is observed. At higher quencher concentrations (Figure 4.4 (b)), the stimulated emission band of MePer overlaps with a spectral feature which shows a positive absorbance change and decays with a time constant of about 15 ps. This kinetics is different from that of the $MePer^{\bullet+}$

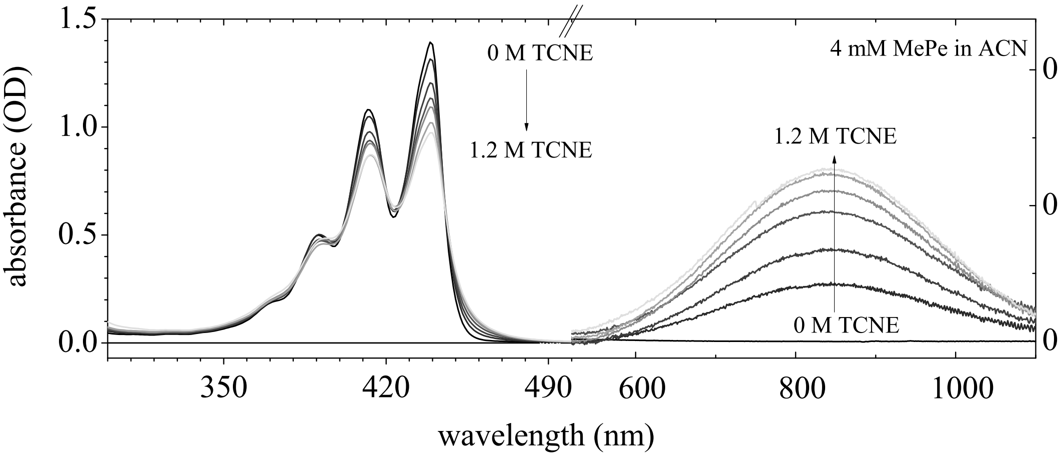

Figure 4.3: Electronic absorption spectra of 4 mM MePer in ACN solution at different TCNE concentrations: 0 M, 0.2 M, 0.4 M, 0.6 M, 0.8 M, 1.0 M and 1.2 M (100 μm cell). The arrows indicate the formation of the CT complex as a function of TCNE concentration.

[‡] The dynamics of the MePer (S_1) band has been reproduced with fluorescence up-conversion measurements guaranteeing that no overlapping absorption band of another species modulates the observed kinetics measured with visible transient absorption spectroscopy.

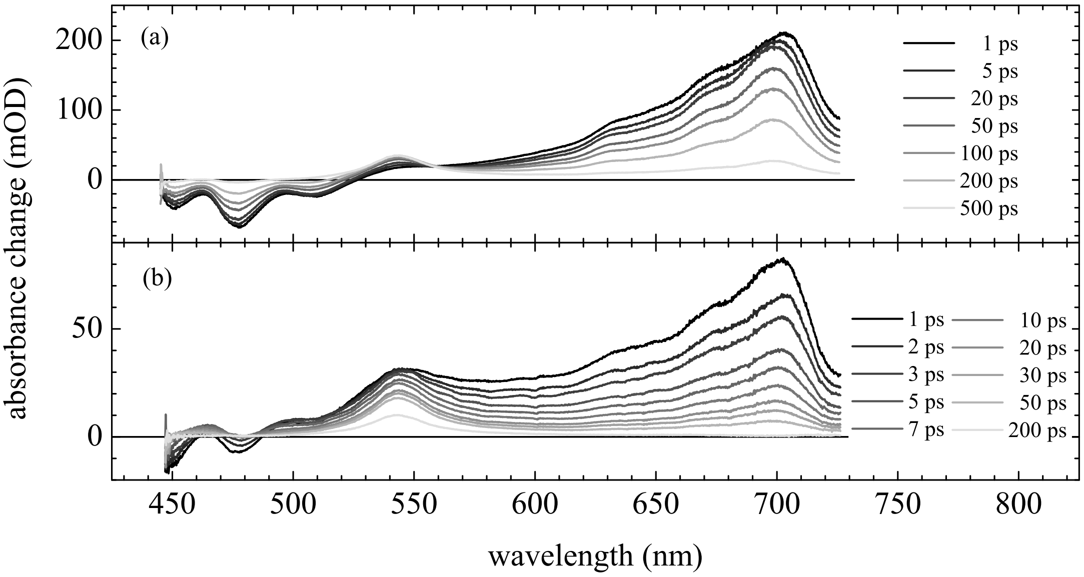

Figure 4.4: Transient UV/Vis difference absorbance spectra recorded at different time delays after local excitation of MePer for (a) 0.1 M TCNE and (b) 0.9 M TCNE in ACN. The signals at 480 nm, 543 nm and 700 nm correspond to stimulated emission, D_0-D_5 transition of the radical cation and excited state absorption of MePer, respectively.

band at 543 nm which excludes the assignment to the radical anion of TCNE, TCNE$^{\bullet -}$. In fact, the absorption coefficient of the TCNE$^{\bullet -}$ band between 370 nm and 490 nm [Shida, 1988] is too small to contribute significantly to the transient spectra. Since this spectral feature is observed at the red edge of the S_0-S_1 absorption band of MePer it can be assigned to absorption of MePer repopulated upon charge recombination, but vibrationally excited ("hot ground state"). Indeed, the 15 ps time constant agrees well with typically observed vibrational cooling rates. The time evolution of the MePer$^{\bullet +}$ band at 543 nm depends significantly on the TCNE concentration, as illustrated in Figure 4.5. At 0.1 M TCNE, the intensity of the MePer$^{\bullet +}$ band increases on a time scale of several tens of picoseconds, reaching a level which remains constant up to 1 ns - the time window of the experiment. By contrast, at 0.9 M TCNE the rise is faster and the intensity decays subsequently to a constant level. The plateau observed for both concentrations is due to the free ion population generated upon dissociation of the ion pairs which decays on a microsecond time scale by homogeneous recombination [Vauthey et al., 1988]. Consequently, the absolute signal intensity of this plateau scales proportionally to the free ion yield. With photoconductivity measurements the free ion yield was determined to amount to 6 % and ≤ 3 % at 0.1 M and 0.9 M TCNE, respectively. Therefore, the maximum signal intensity observed at 543 nm at 0.1 M and 0.9 M TCNE corresponds to only a small fraction (about 6 % and 10 %, respectively) of the total radical ion population formed upon CS quenching of MePer. The fact that only a minor fraction of the total ion population is seen in the transient absorption profile points to a faster charge recombination of the ion pair than it is generated. The estimation of the total ion population from the kinetics of the transient ion population

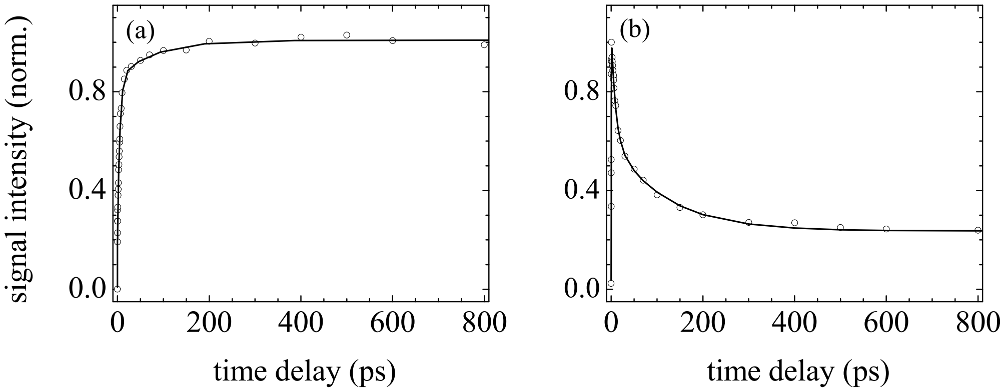

Figure 4.5: Kinetics of the MePer$^{\bullet+}$ band at 543 nm (dots) recorded for 0.1 M (a) and 0.9 M (b) TCNE quencher concentration, showing a fast initial rise, and reaching a final level indicating the free ion yield.

alone leads to an overestimation of the free ion yield and hence to an underestimation of the charge recombination time constant. Earlier time-resolved studies on a similar system, perylene and TCNE, revealed the same ultrafast charge separation and charge recombination dynamics [Pagés et al., 2004]. The transient kinetics of the MePer (S_1) and MePer$^{\bullet+}$ bands at 700 nm and 543 nm could not be reproduced using less than three exponential functions, the best-fit parameters being listed in Table 4.1. Because charge separation and charge recombination occur on the same time scale the data have to be analysed in the following way to obtain the true charge recombination dynamics. The observed time profile of the ion population, $I_{ion}^{obs}(t)$, can be expressed by the

c (M)	λ (nm)	τ_1 (ps)	A_1	τ_2 (ps)	A_2	τ_3 (ps)	A_3
0.1	700	6.3	0.07	137	0.20	345	0.73
0.9	700	0.5	0.17	3.8	0.60	23	0.23
0.1	543	0.3	−0.20	2.0	−0.30	84	−0.50
0.9	543	0.3	−1.00	9.3	0.44	115	0.37

Table 4.1: Parameters (A_i, amplitude; τ_i, time constant) obtained from fitting of a product function with three exponential decay terms to the time-profiles of the VIS-TA intensity recorded at different wavelengths (λ) after 400 nm excitation of MePer with various TCNE concentrations in ACN.

convolution integral:

$$I_{ion}^{obs}(t) = C \int_0^t P_{ion}(t-t') \cdot P_{\mathrm{S}_1}(t')dt' \tag{4.1}$$

where C is a proportionality factor, $P_{ion}(t)$ is the time evolution of the ion population assuming instantaneous formation at time $t = 0$ and P_{S_1} is the temporal evolution of the excited MePer population. If both $P_{\mathrm{S}_1}(t)$ and $P_{ion}(t)$ exhibit monoexponential dynamics with time constants τ_{S_1} and τ_{ion}, respectively, then $I_{ion}^{obs}(t)$ is biexponential with a rising and a decaying component. If $\tau_{\mathrm{S}_1} < \tau_{ion}$, then the rise time is equal to τ_{S_1} whereas the decay time is τ_{ion} and *vice versa* for ions which decay faster than they are formed, namely when $\tau_{ion} < \tau_{\mathrm{S}_1}$. Consequently, an assignment of time constants obtained from the triexponential fit of $I_{ion}^{obs}(t)$ and listed in Table 4.1 to CR time constants has to be done carefully. To have a more reliable picture of the charge recombination dynamics of the MePer$^{\bullet+}$/TCNE$^{\bullet-}$ pair, (4.1) was fitted to the transient absorption profiles measured at different TCNE concentrations. The best-fit parameters are listed in Table 4.2.

c (M)	A_0	τ_1 (ps)	A_1	τ_2 (ps)	A_2	τ_3 (ps)	A_3
0.1	0.08	3.2	0.69	30.4	0.19	127	0.09
0.9	0.07	2.2	0.72	16.0	0.13	116	0.08

Table 4.2: Parameters (A_i, amplitude; τ_i, time constant; A_0, free ion yield) obtained from the fit of (4.1) to the time profile of the VIS-TA intensity shown in Figure 4.5.

The observed complex dynamics points to the occurence of a multitude of types of ion pairs with different associated couplings. Although details such as characteristic time scales have been uncovered with ultrafast electronic spectroscopy [Pagés et al., 2004], a clear experimental distinction between LIPs and TIPs has not been demonstrated so far because the typical strong broadening of electronic transitions masks structural differences between these ion pairs.

Upon charge transfer excitation of the MePer-TCNE complex at 800 nm the visible transient absorption spectra exhibit only the MePer$^{\bullet+}$ band which shows biphasic decay dynamics. The major component (95 %) decays with a 200 fs time constant and the remaining (5 %) goes to zero with a time constant of 7 ps [Mohammed and Vauthey, 2008]. The ion pair dynamics upon charge transfer excitation is consistent with a zero free ion yield.

Experimental

Femtosecond mid-infrared experiments were performed using 20 ml solutions consisting of 4 mM MePer and different concentrations of TCNE in either ACN (Merck) or DCM

(Merck). MePer has been synthesised by O. F. Mohammed according to a procedure reported before [Mohammed et al., 2008] and subsequently purified by column chromatography. TCNE (Aldrich) was sublimed before use. The concentration of TCNE was varied from 0.05 M to 0.9 M in ACN whereas the highest concentration in DCM was 0.1 M due its low solubility. The solvents were used without further purification. The sample absorbance at 400 nm was about 1.5 OD independent of the TCNE concentration. The absorbance at 800 nm depends apparently (Figure 4.3) on the TCNE concentration and is 0.07 OD at 0.9 M TCNE in ACN and 0.045 OD at 0.1 M TCNE in DCM. Local excitation of MePer was achieved with pump pulses of 2 - 3 μJ energy, 55 fs duration at a central wavelength of 400 nm. The MePer-TCNE charge transfer complex was excited with an ultrashort laser pulse at 800 nm with 11 μJ energy per pulse at the sample. The mid-infrared probe pulses were tuned between 2100 cm^{-1} and 2300 cm^{-1} in order to monitor the evolution of the cyano(CN)-stretching vibrational marker modes of the TCNE radical anion. Transient spectra were taken in the spectral range with a central wavelength at 4645 nm and spectral resolution of 2.3 cm^{-1}. In order to guarantee a homogeneously pumped volume of the 300 μm thin sample the beam diameters at the sample position were set to 300 μm and 200 μm for pump and probe beams, respectively. The time resolution was determined to be about 200 fs. In several measurements, the 400 nm pump pulses were stretched to 400 fs duration after propagation through two water cells of 1 cm thickness each to suppress multiphoton contributions.

Results & Discussion

More structural information is revealed with transient infrared absorption spectroscopy by probing the CN-stretching mode range of the generated radical anion, $\mathrm{TCNE}^{\bullet -}$ [Mohammed et al., 2008, 2009a]. Its two antisymmetric CN-stretching vibrational modes are respectively located around 2150 cm^{-1} and 2190 cm^{-1} [Miller, 2006]. Both bands undergo exactly the same dynamics. For the matter of convenience the experimental results will be discussed using the transient band at 2150 cm^{-1}. Please note that the same is true for the band at 2190 cm^{-1}. The left panel in Figure 4.6 shows a series of transient absorption spectra measured in ACN upon local excitation of MePer at 400 nm at three different TCNE concentrations. It is readily apparent that the transient spectra depend on the applied quencher concentration. With 0.2 M TCNE (Figure 4.6 (b)), the transient vibrational band appears within time resolution and subsequently decays during the first 20 ps by about 30 %. This is followed by the appearance of a spectrally narrower (by 5 cm^{-1}) and blueshifted (by 5 cm^{-1}) CN-stretching vibrational band in the time range between 50 ps and 200 ps after which the signal remains essentially constant up to 1 ns. Already at first glance, the spectral changes seem to originate from two distinct spectral components, one decaying and the other ingrowing, as opposed to a continuous spectral shift from one to the other. The band shape was analysed by using singular value decomposition (SVD) and Lorentzian fits. Two spectral components were obtained which closely resemble the early and late spectra recorded with 0.2 M TCNE[§]. Comparison between the transient spectra recorded for different

---

[§] A third and almost flat contribution is present during the excitation pulse and decays rapidly afterwards. Intensity and kinetics depend on the excitation conditions. It might be attributed to a quasi-free electron which has been ejected from MePer by two-photon absorption.

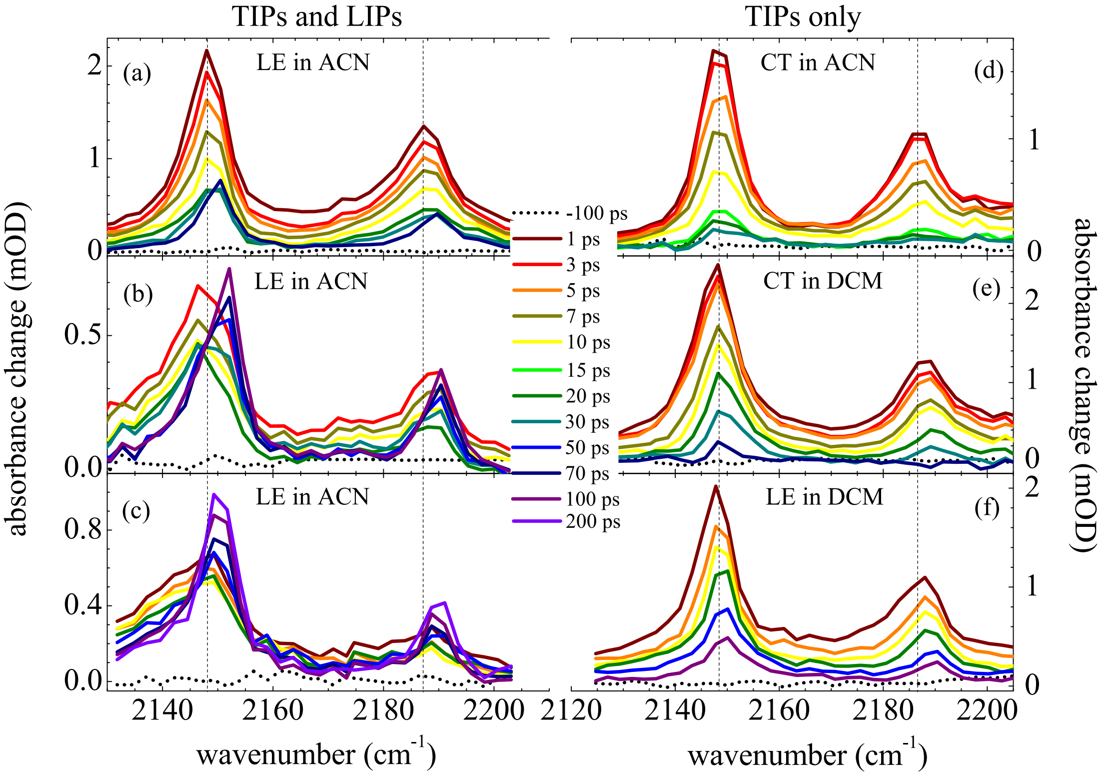

Figure 4.6: Transient absorption spectra of the CN-stretching mode region of the TCNE radical anion in ACN after local excitation of MePer for three different quencher concentrations: 0.9 M (a); 0.2 M (b); 0.1 M (c), clearly showing the early and late spectral components assigned to TIPs and LIPs, respectively. CT excitation of MePer in ACN (d; 0.9 M TCNE) and DCM (e; 0.1 M TCNE) as well as local excitation of MePer in DCM (f; 0.1 M TCNE) only shows the red-shifted component assigned to TIPs. The dotted line indicates the frequency position for TIPs.

quencher concentrations (0.05 M - 0.9 M TCNE) shows that these two components are present for all concentrations, whereby the spectral component at early time delay dominates at high quencher concentration, and *vice versa* for low quencher concentration. All transient spectra obtained upon local excitation of MePer in ACN can be reproduced by a linear combination of the two spectral components from SVD.

The spectral dynamics observed upon local excitation of MePer is absent in the spectra recorded upon CT excitation of the MePer/TCNE donor acceptor complex in ACN at 800 nm as displayed in Figure 4.6 (d). The shape of the transient band closely resembles the early spectral component, mentioned above although the width is slightly smaller. Please note that only a minor fraction of the total response induced by CT excitation is observed in the transient infrared spectra due to the limited time resolution. The band decays to zero with a time constant of 7 ps in agreement with the weak residual intensity in the visible transient absorption measurements.

Transient infrared spectra have also been recorded in the weakly polar solvent DCM upon both CT (Figure 4.6 (e)) and local (Figure 4.6 (f)) excitation. They are essentially the same. Only a slight frequency shift of about 1 cm^{-1} can be seen for the case of local excitation of MePer which continuously shifts with a time constant of around 20 ps, a typical cooling rate in DCM [Mohammed et al., 2006]. For both local and CT excitation the measured transient spectra resemble the early spectrum obtained in ACN upon local excitation. Moreover, the transient bands decay to zero, indicative of a free ion yield of zero. The decay is biphasic after 400 nm excitation (0.1 M TCNE) with time constants of 24 ps (75 %) and between 300 - 600 ps (25 %), while it is monoexponential with a 11 ps time constant upon CT excitation.

Figure 4.7 shows the time evolution of the area of the low frequency CN-stretching band around 2150 cm^{-1} measured upon local excitation in ACN with various TCNE concentrations. The areas have been obtained by fitting Lorentzian line shapes to the experimental data and taking then the resulting peak integral. As to be seen from this figure, the dynamics of the early contribution does not or only weakly depend on TCNE concentration, only its amplitude increases with quencher concentration. The dynamics of the late contribution, on the other hand, strongly varies with TCNE concentration. A comparative analysis of these time profiles is difficult to perform as they cannot be always reproduced by a multiexponential or any other obvious analytical function. At 0.1 M TCNE, a fit to the late part yields a biphasic rise with 20 ps (65 %) and 240 ps (35 %). At the intermediate concentrations, 0.2 M and 0.3 M, a multiexponential function does not accurately reproduce the data. On the other hand, the profiles at 0.6 M and 0.9 M can be analysed using a triple exponential function with one rising and two decaying components. The parameters at 0.9 M TCNE are consistent with those obtained from the VIS-TA data. At 0.1 M, the time constants for the rising part do not match with those found in the VIS-TA data. This is not impressive as the early part, which looks like an almost constant contribution in the Lorentz-fit, has to be separated from the late one, which is inherently inducing incertitude. Furthermore, the extinction coefficient of the two components might not be the same. On the other hand, at 0.9 M there is almost no late component in the IR data and therefore, the kinetics become more comparable.

Because of the dynamics associated with the two spectral components and the dependence of their amplitude on the TCNE concentration, the early and late spectral

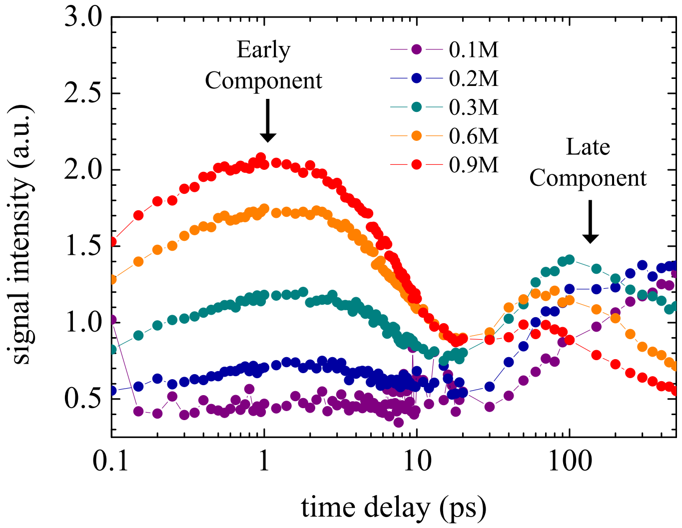

Figure 4.7: The time-dependent intensity of the CN-stretching band at 2150 cm^{-1} of TCNE$^{\bullet-}$ in ACN, obtained by analysing the transient spectra at different quencher concentrations, clearly shows an early component dominated by TIPs, and a late component of LIPs governed by diffusional dynamics.

component can be reasonably assigned to tight and loose ion pairs, respectively. TIPs result mainly from a quasi-static quenching of the fraction of MePer (S_1) population with a TCNE molecule at optimal position for ultrafast charge separation. Such a situation is favoured by high quencher concentration. As formation of these pairs does almost not involve diffusion, their formation and decay do essentially not depend on TCNE concentration, as found for the early spectral component. On the other hand, the late spectral component with a narrow and blue-shifted band is absent during the first 20 ps after excitation. Its maximum amplitude is reached after several hundreds of picoseconds depending on the quencher concentration. This spectral component can be attributed to LIPs. These pairs are the products of the dynamic quenching of the MePer (S_1) population without a nearby TCNE molecule with an optimal position for charge separation. As a consequence, the reactants have to diffuse until they couple enough to undergo charge separation. In this case, the coupling should be just large enough to make charge separation faster than diffusion. The assignment of these spectral components is supported by the transient infrared results obtained upon 800 nm excitation. First, the CT excitation spectra are very similar to the early spectrum found upon local excitation of MePer at 400 nm, the main difference being a smaller bandwidth. Second, the decay of the ion bands is ultrafast as the decay of the early spectral component. Direct excitation in the CT band of a donor-acceptor complex directly leads to TIPs [Nicolet and Vauthey, 2002; Nicolet et al., 2005]. As the oscillator strength of the CT transition is directly proportional to the square of the electronic coupling [Kulinowski et al., 1995], LIPs have no possibility to be generated upon optical CT excitation. It should, nevertheless, be noted that only a small fraction of the ion pairs produced upon CT excitation is seen in the transient infrared data. Indeed, the visible transient absorption measurements show that the majority of these pairs undergoes charge recombination with a 200 fs time constant and that only a minor fraction decays on the few ps time scale. Only this minor fraction can clearly be observed because of the smaller time resolution of the transient infrared absorption experiment. Although these pairs recombine much slowly than the others, they still can be considered as strongly coupled. The data obtained in the weakly polar solvent DCM upon 400 nm excitation further supports this interpretation. In this solvent, the CN-stretching vibrational bands are at the same frequency as one can find in the early spectrum of ACN, pointing to a strong coupling. This is also consistent with the relatively fast decay of these bands with a 24 ps time constant for charge recombination. As DCM is weakly polar, Coulomb interaction between the ions is not screened and thus LIPs, if formed, collapse into TIPs but do not dissociate into free ions.

A frequency red-shift at early times does not *a priori* indicate a different species, as local excitation of MePer in ACN, where 2.25 eV of energy is released upon charge separation, may cause excess energy redistribution into vibrational modes that may potentially contribute to transient frequency downshifts [Nibbering et al., 2005]. Subsequent vibrational cooling would then also cause frequency up-shifting on a time scale of tens of picoseconds. In contrast, CT excitation generates a TCNE-radical anion without significant excess energy (0.7 eV). Assuming all ion pairs are formed in a hot vibrational state which subsequently cools down, such a transient spectral picture, two distinct spectral components rather than a continuous frequency shift, can only be observed for the case that charge separation is much slower than vibrational cooling. This is most definitely not the case for high quencher concentrations. The excess energy is therefore channelled through intramolecular vibrational redistribution in $\text{MePer}^{\bullet+}$ and dissipated to the solvent. This hypothesis will be discussed in the next section. The reason for the spectral difference between the CN-stretching vibrational band associated with LIPs or with TIPs is in fact due to a significantly different charge distribution of electron density in $\text{TCNE}^{\bullet-}$. Quantum chemical calculations suggest that, in the case of TIPs, the vibrational red-shift points to a stronger coupling of $\text{TCNE}^{\bullet-}$ with $\text{MePe}^{\bullet+}$. Indeed, substantial ion pairing effects on the frequencies of the CN-stretching bands of TCNE^{2-} have been reported in the literature [Khatkale and Devlin, 1979]. However, solvent induced frequency shifts are of similar magnitude, and the underlying reasons for the frequency shifts may be more intricate.

4.2 Energy release in tight ion pairs

Energy release following photoinduced electron transfer reactions in solution is not fully understood. Intramolecular vibrational excitations play a key role in the microscopic mechanism and dynamics of these reactions. Section 1.3 touches on the subject of vibrational modes with non-vanishing Franck-Condon vibrational overlap integrals between the coupled electronic states of the donor-acceptor super-molecule before and after charge separation. The question of the energy release pathway is connected to such Franck-Condon factors and the density of vibrational levels in the D^+A^--state to which the energy of the DA-state can be channelled. In order to know how much energy is released to TCNE compared to MePer upon charge separation and charge recombination their accepting modes have to be identified. This is a challenging task. The approach outlined here combines ultrafast UV-pump/IR-probe spectroscopy with density functional theory and a finite differences method. In the following, the results obtained with two different donor-acceptor systems, MePer/TCNE and 9,10-dicyanoanthracene (DCA)/TCNE will be presented. With MePer as electron donor, a manifold of excited states of the radical cation is situated below the S_1 state of the chromophore [Pagés et al., 2004] and thus, an excited radical ion could be formed. Due to a lack of information on the energies of the excited states of the radical cation, only the D_1 excited state is considered here. With DCA on the other hand, the first excited state of the radical cation is located above the S_1 state. The ion pair should accordingly be formed exclusively in the ground state. The energy level diagrams for both systems are shown in more detail in Figure 4.8. The possibility that the excited state radical cation of MePer is involved in the photoinduced electron transfer reaction opens up three different pathways for energy release:

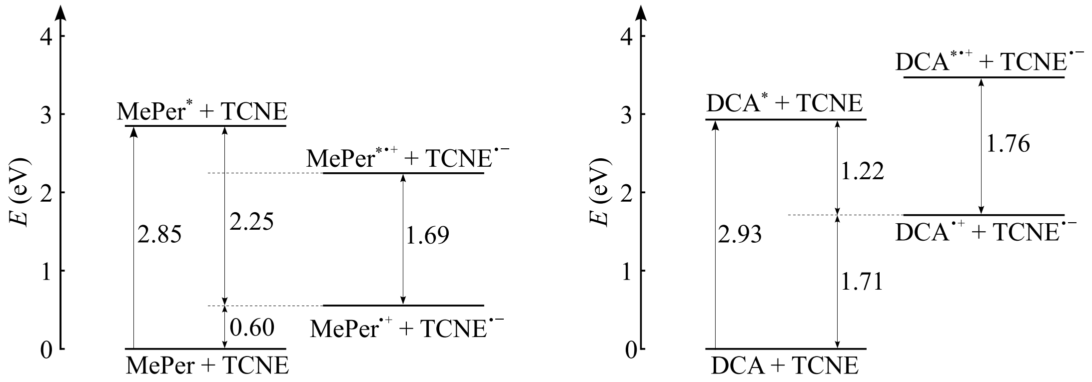

Figure 4.8: Energy diagrams for the photoinduced charge separation between MePer and TCNE as well as DCA and TCNE in ACN. Excited states of radical cations are considered. Parameters for the calculation: $E(\mathrm{TCNE}^0|\mathrm{TCNE}^{\bullet-})$ = 0.24 V vs. SCE [Ganesan et al., 2003], $E(\mathrm{DCA}^{\bullet+}|\mathrm{DCA}^0) = 1.93$ V vs. SCE [Kikuchi et al., 1993], $E(\mathrm{S}_1, \mathrm{DCA}) = 2.93$ eV, $E(\mathrm{D}_1, \mathrm{DCA}) = 1.76$ eV [Shida, 1988], $E(\mathrm{MePer}^{\bullet+}|\mathrm{MePer}^0) = 0.85$ V vs. SCE [Mataga et al., 1988], $E(\mathrm{S}_1, \mathrm{MePer}) = 2.85$ eV, $E(\mathrm{D}_1, \mathrm{MePer}) = 1.69$ eV [Shida, 1988], ionic radii of 3 Å.

(I) Charge separation leads to $\mathrm{MePer}^{\bullet+}$, the electronic ground state radical cation. The corresponding free energy of charge separation and charge recombination are $\Delta G^0_{\mathrm{CS}} = 2.25$ eV and $\Delta G^0_{\mathrm{CR}} = 0.60$ eV, respectively.

(II) Charge separation leads to $\mathrm{MePer}^{*\bullet+}$, the electronic excited state radical cation. Subsequent internal conversion between the electronic excited state and the ground state of the radical cation releases its corresponding energy into accepting vibrational modes of $\mathrm{MePer}^{\bullet+}$ in its electronic ground state. In this case the free energy of charge separation, charge recombination and internal conversion are as follows: $\Delta G^0_{\mathrm{CS}} = 0.56$ eV, $\Delta G^0_{\mathrm{CR}} = 0.60$ eV and $\Delta G^0_{\mathrm{IC}} = 1.69$ eV.

(III) Charge separation leads to MePer$^{*\bullet+}$, the electronic excited state radical cation. However, due to the faster charge recombination in comparison to the internal conversion the latter process does not play a significant role. Charge recombination proceeds between the electronically excited radical cation, MePer$^{*\bullet+}$, and TCNE$^{\bullet-}$. The corresponding free energy of charge separation and charge recombination are $\Delta G^0_{\mathrm{CS}} = 0.56$ eV and $\Delta G^0_{\mathrm{CR}} = 2.29$ eV, respectively.

According to scenarios (I) and (III) the sum of the free energy which is released upon charge separation and charge recombination is the same, namely $\Delta G^0 = 2.85$ eV. The full initial excitation energy can be released to both reactants, donor and acceptor, during the full CS-CR cycle. This is in marked contrast to scenario (II): only part of the excitation energy can be released to both molecules. In fact the energy amounts to 1.16 eV. In case of DCA as electron donor the free energy of charge separation and charge recombination are $\Delta G^0_{\mathrm{CS}} = 1.22$ eV and $\Delta G^0_{\mathrm{CR}} = 1.71$ eV, respectively. In this case, the full initial excitation energy of 2.93 eV can be released to both, donor and acceptor, without a fraction that can be *a priori* allocated to the donor.

Experimental

Femtosecond mid-infrared experiments were performed using 20 ml solutions consisting of either 4 mM MePer or $1.8 \cdot 10^{-4}$ M DCA and different concentrations of TCNE in ACN (Merck). The sample absorbance at 400 nm was about 1.0 OD for MePer (Figure 4.3) and 0.1 OD for DCA (Figure 4.9) independent of the TCNE concentration. Local excitation of MePer or DCA was achieved with pump pulses of 3.5 μJ energy, 55 fs duration at a central wavelength of 400 nm. The mid-infrared probe pulses were tuned between 2100 cm^{-1} and 2300 cm^{-1} in order to monitor the evolution of the CN-stretching vibrational marker modes of the TCNE radical anion and of TCNE in the ground state. Transient spectra were taken in the spectral range with central wavelength at 4600 nm and spectral resolution of 2.4 cm^{-1}. In order to guarantee a homogeneously

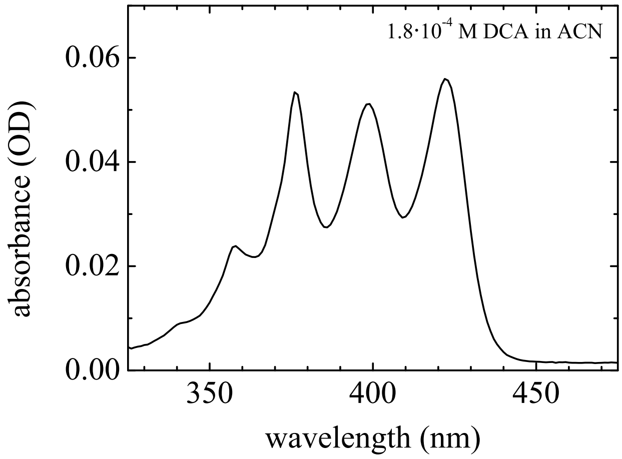

Figure 4.9: Electronic absorption spectra of $1.8 \cdot 10^{-4}$ M DCA in ACN solution (100 μm cell).

pumped volume of the 200 μm thin sample the beam diameters at the sample position were set to 250 μm and 150 μm for pump and probe beams, respectively. The time resolution was determined to be about 200 fs.

Results & Discussion

The left panel in Figure 4.10 shows a series of transient absorption spectra measured in ACN upon excitation of DCA at three different TCNE concentrations. Several contributions overlap in this spectral range. The largest feature located at 2164 cm^{-1} is due to the S_1 excited state absorption of DCA. This transient signal has been recorded upon excitation of DCA with no quencher added to be able to subtract this contribution. For each transient spectrum shown in Figure 4.10 (a) - (c) the excited state absorption spectrum of DCA at the same time delay has been normalised to the value at the pixel with the maximum intensity of the S_1-band. The pure S_1-contribution has been subtracted pixel by pixel. The result of the data analysis is shown in the right panel of Figure 4.10. After subtraction of the S_1-contribution four transient signals are present: the band at 2150 cm^{-1} is due to the antisymmetric CN-stretching vibrational mode of the TCNE$^{\bullet-}$ radical anion. This signal has been observed before using MePer as electron donor. With DCA as electron donor the same temporal evolution of the spectral shape of the vibrational band at 2150 cm^{-1} due to the dynamics of the two distinct spectral components is observed as already discussed in section 4.1. The bimolecular ET reaction between DCA and TCNE therefore results also in the formation of TIPs and LIPs. The signal at 2190 cm^{-1}, however, cannot be seen at early time delays up to 50 ps since a third more intense signal overlays this weak band. This latter signal is present immediately after excitation of DCA and its maximum shifts from 2190 cm^{-1} at time delays less than 1 ps to 2200 cm^{-1} at time delays higher than 30 ps. The corresponding frequency blue shift amounts to 10 cm^{-1}. The fourth contribution is the ground state bleach of the TCNE antisymmetric CN-stretching vibration at 2205 cm^{-1} due to the disappearance of ground state TCNE upon ET reaction. At later time delays, the bleach recovers due to charge recombination. The recovery is accompanied by a spectral blue shift of about 3 cm^{-1}. Comparison between the transient spectra recorded for different quencher concentrations (0.3 M - 0.9 M TCNE) shows that the shape of the third contribution does not vary with TCNE concentration, only its amplitude changes. The same applies also for the bleach signal.

The fraction of reactive complexes with strong electronic coupling undergoes charge separation and subsequent charge recombination within the experimental time resolution. The energy which is released upon these two processes is channelled to primary accepting vibrational modes of both molecules, DCA and TCNE. This leads to a non-thermal non-Boltzmann population distribution of the intramolecular vibrational modes. Upon intramolecular vibrational redistribution, typically occuring on (sub)picosecond time scales [Hogiu et al., 2000; Kozich et al., 2002, 2006, 2009] a Boltzmann distribution results. With this it is possible to determine an internal temperature of the molecule. Because the energy dissipation to the solvent is much slower (about several tens of picoseconds) the internal temperature is much higher than that of the surrounding solvent. One can refer to the molecule being "vibrationally hot". If the assumption of a Boltzmann distribution holds the excess energy is predominantly present in low-frequency modes. Due to anharmonic coupling of the CN-stretching vibration of TCNE to these

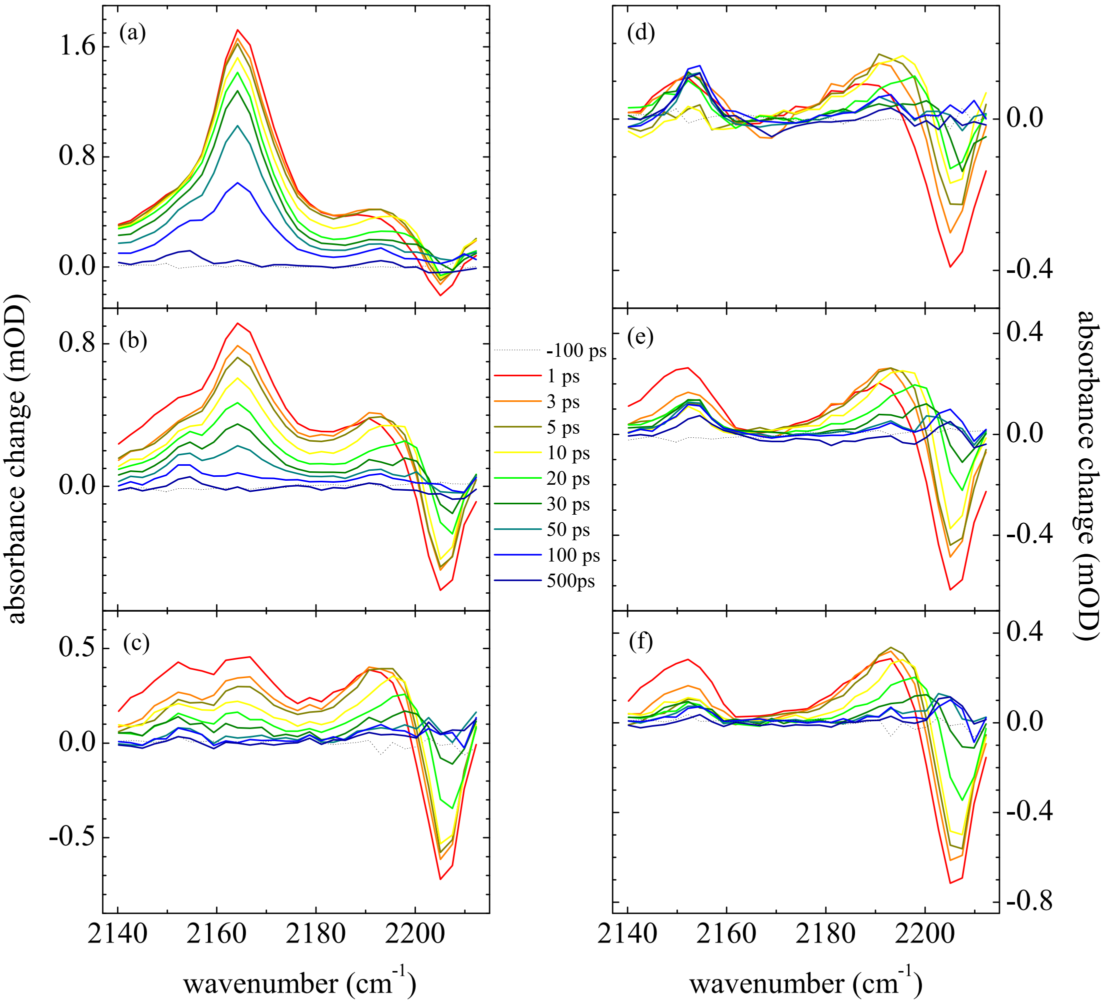

Figure 4.10: Transient absorption spectra of the CN stretching mode region of the TCNE radical anion in ACN after local excitation of DCA for three different quencher concentrations: 0.3 M (a); 0.6 M (b); 0.9 M (c) as measured and 0.3 M (d); 0.6 M (e); 0.9 M (f) after subtraction of the S_1 excited state absorption of DCA.

excited low-frequency modes with mainly negative off-diagonal anharmonic coupling constants, the CN-stretching vibrational band exhibits a red-shift and a strong asymmetric broadening as shown in Figure 3.3. The intramolecular temperature of TCNE before the photoinduced ET reaction is about 300 K. The ground state TCNE population decreases upon charge separation giving rise to the observed bleach signal. If there was no excess energy channelled to TCNE this bleach signal recovers at the same time scale as the charge recombination. Since the intramolecular temperature of TCNE is higher than 300 K after passing through the CS - CR cycle a difference absorption spectrum results as shown in Figure 4.11. Depending on the intramolecular transient temperature a positive red-shifted signal and a bleach signal are to be seen. Qualitatively, the simulated and the experimentally obtained difference absorption spectra are in good agreement. The positive signal at 2190 cm^{-1} which shifts to the blue within 30 ps corresponds to the hot ground state. This frequency shift is due to the decrease of the intramolecular temperature as a result of the intermolecular energy transfer to the solvent. With increasing frequency the spectral overlap between the hot ground state contribution and the bleach signal becomes more prominent which gives rise to the observed spectral dynamics on the bleach signal. For the simulation which is briefly described in section 3.2 an ultrafast intramolecular vibrational redistribution of less than 1 ps is assumed. The question whether IVR occurs on a subpicosecond time scale and whether it is much faster than intermolecular energy transfer needs still to be answered.

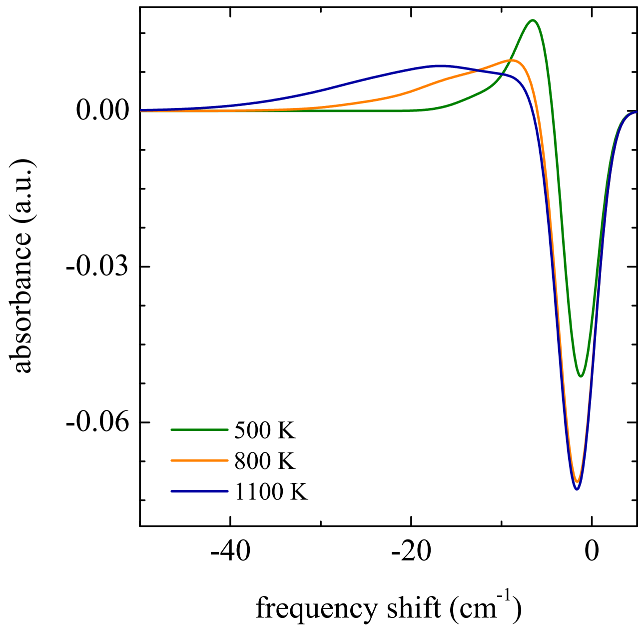

Figure 4.11: Simulated difference absorption spectra of the ν_{23} mode of tetracyanoethylene at different temperatures. Frequency shifts are plotted relative to the frequency at 0 K.

Transient anti-Stokes Raman measurements on several systems and upon different excitation conditions show that a nonthermal distribution of vibrational populations can exist up to 5 - 15 ps [Hogiu et al., 2000; Kozich et al., 2002, 2006, 2009]. Nevertheless it is possible to exclude a strong deviation from a thermal energy distribution. A selective excitation of a distinct vibrational line yields a different spectral fingerprint as shown by Hamm [Hamm et al., 1997].

A comparison between the transient spectra measured with MePer/ TCNE and DCA/ TCNE reveals that such a hot ground state contribution is absent when using MePer as electron donor. As can be seen in Figure 4.12 only three signals are present: both CN-stretching vibrational bands of TCNE$^{\bullet-}$ at 2150 cm^{-1} and 2190 cm^{-1} as well as the ground state bleach signal at 2208 cm^{-1}. This indicates that a negligible amount of energy is released to TCNE which suggests strongly that scenario (II) applies for the system MePer/TCNE.

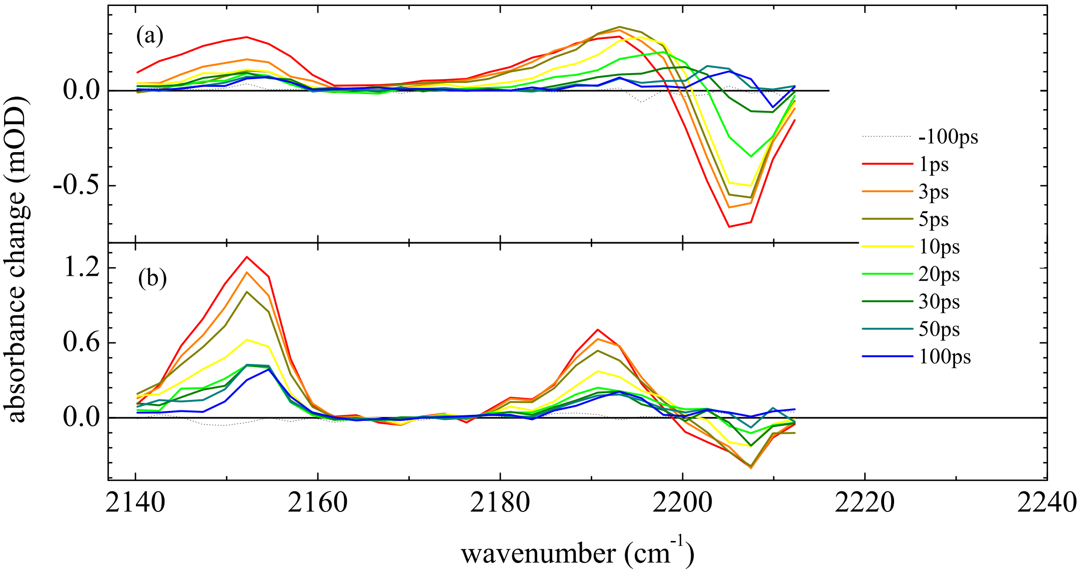

Figure 4.12: Comparison of the transient absorption spectra of DCA (a) and MePer (b) in ACN for 0.9 M TCNE. The hot ground state contribution as to be observed with DCA as electron donor is missing when using MePer.

Now, that TIPs and LIPs are identified and connected to their reaction pathways along with the reaction dynamics (section 4.1) and that the question of energy release in TIPs has been discussed (section 4.2) it is the aim of the coming section to reveal the structure of TIPs.

4.3 Importance of the mutual orientation of reaction partners

The question whether TIPs have preferred geometries or are just generated by a statistical distribution of donor-acceptor complexes at close range can be answered with polarisation-sensitive femtosecond infrared spectroscopy [Lim et al., 1995].

Experimental

Polarisation-sensitive mid-infrared measurements were realised in such a way that for each time delay, three transient spectra have been recorded, with the polarisation of the probe light aligned parallel, perpendicular and at magic angle with respect to the polarisation of the excitation light. As the reflectivity of the dielectric mirrors is not identical for the three angles, the obtained spectra have been corrected in a way that a) the resulting anisotropy decays to zero at long pulse delays and b) the isotropic signals measured at magic angle configuration and calculated from the combination of parallel and perpendicular configurations are identical. The sample of 4 mM MePer and 0.9 M TCNE in ACN was pumped at 400 nm.

Results & Discussion

Figure 4.13 shows the time evolution of the measured anisotropy on the CN-stretching band at 2150 cm^{-1}. The initial anisotropy r equals 0.09 ± 0.03 for the early contribution on both antisymmetric CN-stretch vibrations. This anisotropy decays on a 10 ps timescale, in agreement with the reorientational time constant of 14.5 ps reported for MePer in ACN [Morandeira et al., 2003]. The initial value for the anisotropy on both

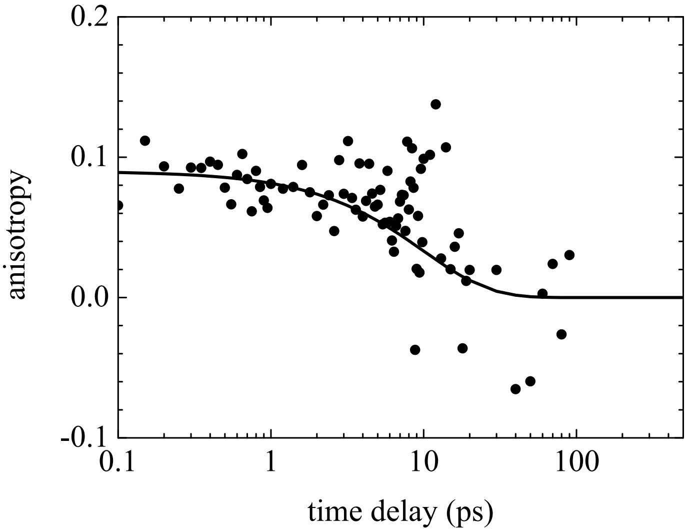

Figure 4.13: The anisotropy r of the CN-stretching band at 2150 cm^{-1}: the experimental data for 0.9 M TCNE are shown as dots and the single-exponential fit of the decay dynamics due to rotational diffusion is indicated as a solid line.

bands reveals structural insight into the reactive complex:

The electronic transition dipole moment for the local excitation is directed along the long axis of MePer as shown in Figure 4.14 a). The IR transition dipole moments of the two CN-stretching vibrations $\mu_{IR,1}$ and $\mu_{IR,2}$ are aligned in the plane of TCNE, either parallel or perpendicular to the ethylenic bond, for the bands at 2190 cm^{-1} and 2150 cm^{-1}, respectively. They are orthogonal to each other. An anisotropy $r = 0.09 \pm 0.03$ on both bands at early time delays implies an average angle of 45° between the electronic transition dipole moment μ_{el} of MePer and the IR transition dipole moments of the two vibrations $\mu_{IR,1}$ and $\mu_{IR,2}$. Furthermore, the electronic transition dipole moment must be parallel to the plane of the TCNE molecule. Within this plane it can be oriented in different ways (Figure 4.14 b)): (i) with an angle of 45° for both transitions μ_{IR} with respect to μ_{el} for all TIPs, (ii) in a statistical distribution of 50 % MePer with the long axis oriented parallel and 50 % perpendicular to the C=C axis of TCNE and (iii) completely random within the plane. Based on this geometric insight together with the fact that ultrafast electron transfer rates are found for TIPs, it can be concluded that MePer and TCNE are aligned in sandwich-type cofacial arrangement thereby maximising orbital overlap and electronic coupling. This geometry agrees well with what has been found in X-ray diffraction studies of crystalline donor-acceptor complexes [Harding and Wallwork, 1955; Jones and Marsh, 1962]. It is unfortunately not

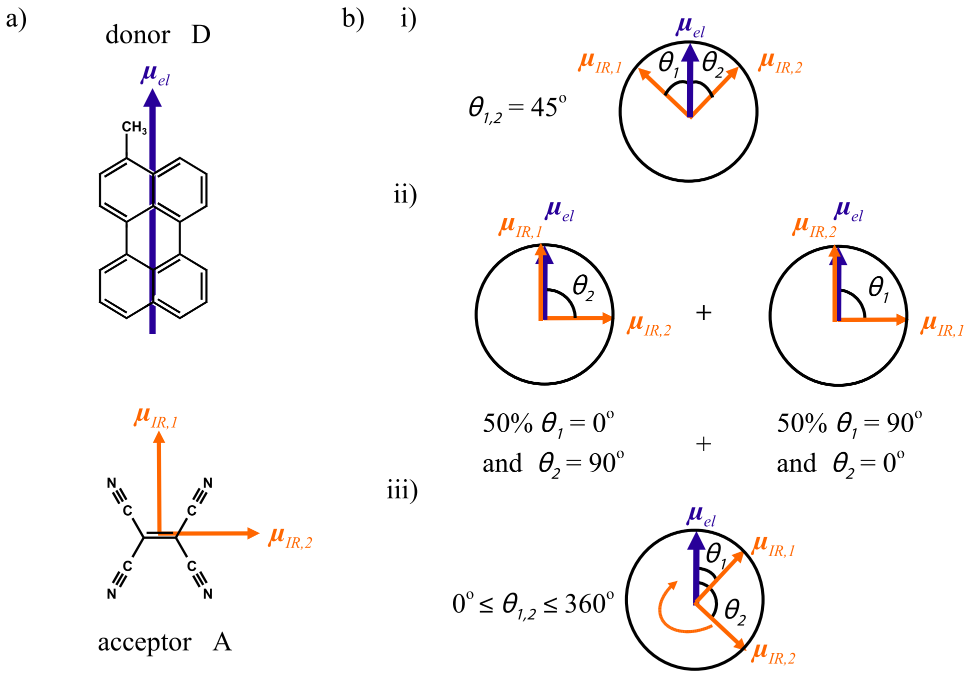

Figure 4.14: a) Molecular structures of donor D, MePer, and acceptor A, TCNE along with the electronic and IR transition dipole moments (μ_{el}, $\mu_{IR,1}$ and $\mu_{IR,2}$). b) Three possible geometries of the reactive complex for which both IR-active vibrations show an anisotropy $r = 0.1$.

possible to obtain such detailed structural information on the ion pairs responsible for the spectral component of the LIPs appearing later than 20 ps, as anisotropy decay due to rotational motions of the ions is by then almost complete [Morandeira et al., 2003].

Theoretical support for sandwich-structures

To get more insight into possible mutual orientations of MePer and TCNE quantum chemical calculations have been carried out in the electronic ground state as well as in the first excited state. In order to perform model calculations perylene (Pe) has been used throughout the calculations leaving out the methyl group. It has been verified in test calculations that the influence of the methyl group is only of minor significance for the structures investigated here. For the ground state calculations Hartree-Fock (HF/6-31G(d)) as well density functional theory methods (B3LYP/6-31G(d,p)) have been applied. For excited states configuration interaction with single excitations (CIS/6-31G(d)) methods has been used. Geometry optimisations were followed by vibrational frequency analyses to verify the nature of the stationary points as minimum structures on the potential energy surface. Please note that only gas phase calculations are reported here. All calculations were performed by J. Dreyer with the program Gaussian 03 [Frisch et al., 1998].

First, potential energy surface scans have been performed to localise possible ground state structures of Pe/TCNE tight complexes by varying the relative position of TCNE with respect to Pe. In the scans TCNE was kept parallel to Pe with the double bond aligned either along the long axis or the short axis of Pe, respectively. Local minima of the potential energy surface were fully optimised resulting in two different structures shown in Figure 4.15. Structure (a) is only about 260 cm^{-1} more stable than structure (b) according to results of B3LYP/6-31G(d,p) calculations. Structure (a) corresponds to the conformation that has been observed experimentally in Pe/TCNE crystals [Ikemoto et al., 1970; Ciezak et al., 2006] and has already been characterised computationally before [Ciezak et al., 2006]. Both complexes are oriented essentially in

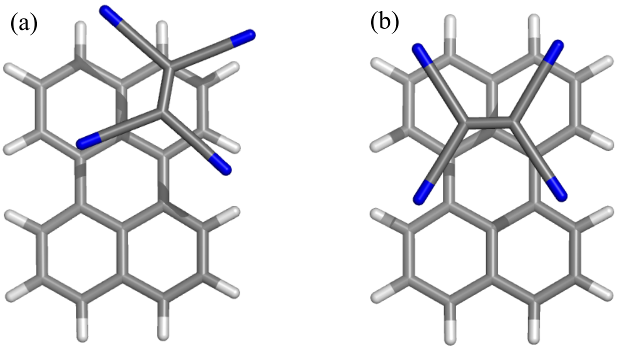

Figure 4.15: Local ground state minima obtained with density functional theory calculations.

a parallel sandwich-like structure. In structure (a), however, the naphthalene moiety in Pe that is not overlayed by TCNE is somewhat tilted out-of-plane away from TCNE. Dipole moments are 4.0 D and 3.3 D for structures (a) and (b), respectively, and the separation of TCNE and Pe amounts to about 340 pm for both structures. From this a charge transfer corresponding to 0.2 electrons from Pe to TCNE is inferred. Hartree-Fock calculations, performed as a reference for excited state CIS/6-31G(d) calculations, yield qualitatively similar results.

For geometry optimisations in the first excited state both ground state structures were used as starting points. Both calculations converged to the same final geometry, which was confirmed by vibrational analysis to be a S_1 minimum structure at the CIS/6-31G(d) level of theory (Figure 4.16). Here, the TCNE molecule is oriented along the diagonal of Pe again in a parallel sandwich-like structure. At the CIS/6-31G(d) theoretical level the S_1 state is fully characterised by the single electronic transition from HOMO to LUMO. Both orbitals are entirely localised on one of the two complex molecules, the HOMO on Pe and the LUMO on TCNE. Thus, the HOMO-LUMO transition corresponds to a charge transfer transition. From the calculated dipole moment of 14.7 D and the complex separation of 367 pm a degree of charge transfer corresponding to about 0.8 electronic charges is calculated. Thus, this charge transfer state calculated in the gas phase resembles a solution phase ion pair in close contact, that is the tight ion pair. For a distinction of tight and loose conformations more sophisticated computational methods considering the surrounding solvent molecules explicitly are needed.

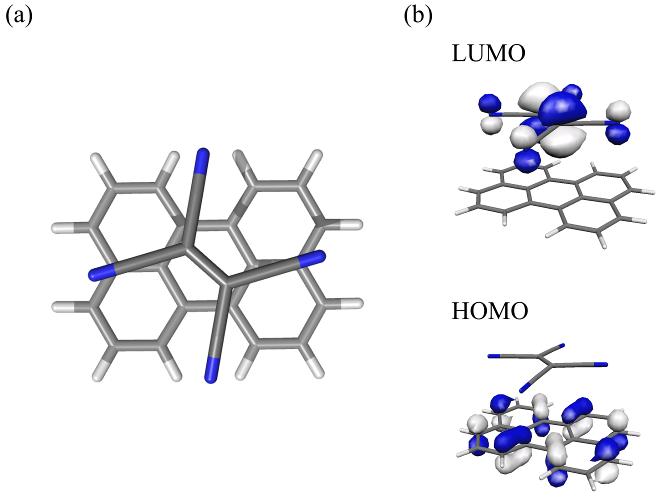

Figure 4.16: (a) Minimum structure in the S1 state localised with CI singles calculations. (b) Highest occupied molecular orbital (HOMO) and lowest unoccupied molecular orbital (LUMO).

4.4 Conclusion

The results obtained by studying the photoinduced bimolecular ET reaction between MePer and TCNE in acetonitrile with polarisation-sensitive UV-pump/IR-probe spectroscopy offer for the first time a univocal spectroscopic evidence for different types of ion pairs involved in the reaction. Assuming two types of charge separation products of well-defined geometry is most definitely not an appropriate simplification. Already the biphasic decay dynamics of the TIPs formed upon CT excitation points to TIPs with different geometries and thus different electronic couplings. Reactant pairs with a weaker coupling may still exhibit a non-zero oscillator strength for CT transition. Upon CT excitation a small population of formed TIPs are less strongly coupled and therefore have a sufficient lifetime to be observed in the time-resolved experiments. These less strongly coupled tight ion pairs are observed upon both local and CT excitation that is confirmed by the same transient spectrum and the same dynamics. Concluding, tight and loose ion pairs should be considered as limiting cases, there is a continuous distribution of pairs between these two limits. TIPs, most likely in a sandwich-like cofacial arrangement, are charge separation products with strong electronic couplings that lead to both ultrafast formation and decay rates on subpicosecond time scales. LIPs, on the other hand, exist in a less defined geometry with a very likely rather wide variety of mutual orientations and centre-to-centre distances which result in a weaker electronic coupling as well as formation and decay rates in the picosecond range. The crucial parameter governing the nature of the primary charge separation products, TIPs or LIPs, is the distribution of neutral reaction pairs in the ground state. This distribution strongly depends on the quencher concentration and on the nature and magnitude of interaction between the reactants. TIPs will be formed upon local or CT excitation of strongly coupled ground state reaction pairs whereas LIPs will be generated either upon static quenching of weakly coupled donor-acceptor pairs or upon diffusional encounter of the locally excited donor with an acceptor molecule. This conclusion can be drawn considering the distinctly different orders of magnitude for the time scales for charge separation and charge recombination in the case of tight and loose reaction pathways together with the fact that diffusional motions are slow. In order to explain the experimental results, following scheme (Figure 4.17) can be proposed: At the time the charge separation reaction is initiated with an ultrashort pump pulse, a certain number of MePer/TCNE pairs are complexed and thus strongly coupled. They undergo rapid charge separation and subsequently even faster charge recombination which results finally in neutral complexed ground-state pairs within a few picoseconds. Considering that charge separation occurs on much faster time scales than diffusional motions interconversion of strongly coupled reaction pairs into weakly coupled reaction pairs can be excluded. The same is true for the interconversion of TIPs into LIPs before charge recombination. Those chromophore molecules which are not complexed with a nearby quencher molecule first have to form an encounter complex after translational and rotational diffusion. It is generally assumed that the charge separation rate depends on the overlap of the involved molecular orbitals and therefore on the distance between the reactants and on the mutual orientation within the reactive complex. Consequently, charge separation can occur before the reactive complex has reached its optimal geometry. In fact, as soon as the charge separation rate constant k_{CS} is higher than the diffusion rate constant k_d, a LIP may be formed which exhibits a sufficiently small rate

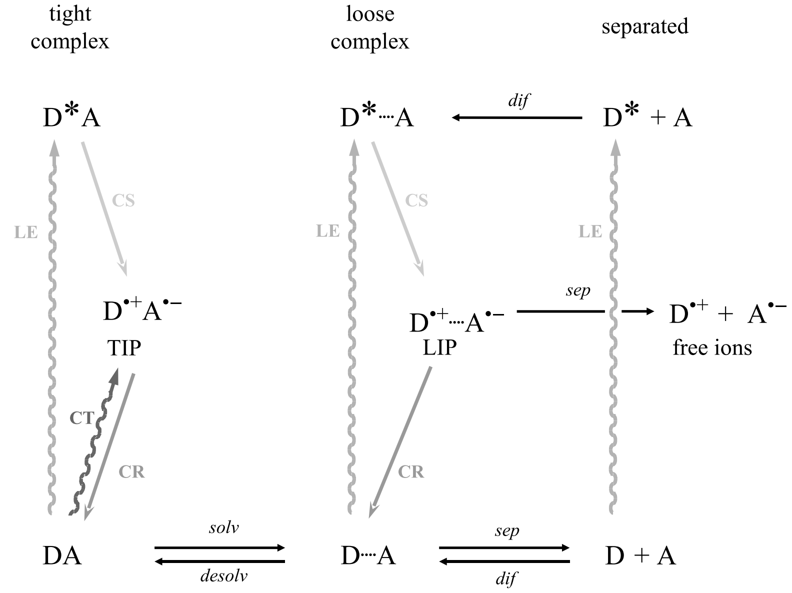

Figure 4.17: Referring to Figure 4.1, the results obtained with the bimolecular ET system, MePer and TCNE, do not show solvation and desolvation between tight and loose complexes, and TIPs and LIPs which is assumed by the standard model.

for charge recombination which allows separation into free ions to compete. Loose ion pairs are thus the unique source of free ions. However, diffusion of the ions can also result in an increase of the electronic coupling. Then charge recombination probably takes place before the optimal mutual orientation of the ions is reached.

The outcome that highly exergonic charge separation quenching yields both TIPs and LIPs is in strong disagreement with the conventional model invoking a driving force dependent ET distance to explain the absence of the inverted regime in bimolecular photoinduced ET. Moreover, current ET theories cannot account for both charge separation and charge recombination being of ultrafast nature. In case of MePer as electron donor and TCNE as electron acceptor experimental results indicate that photoinduced charge separation might lead to the excited radical cation of MePer. Subsequent intramolecular conversion from the excited to the ground state radical cation and charge recombination affects the free energy of charge separation and charge recombination. The lower free energy for both processes could account for the processes to be of ultrafast nature. However, in case of DCA as electron donor charge separation leads to TIPs and LIPs although the reaction is indeed highly exergonic. Because of its anisotropic nature, the electronic coupling V at contact distance is much larger than assumed in models using spherical symmetry, where the couplings are averaged over all mutual orientations of the reactants. This means that even if charge separation takes place at contact distance in the inverted regime, the couplings are large enough to guarantee ultrafast ET reaction rates, much faster than diffusion. Furthermore, because of the anisotropy, the decrease of V with distance (when TIPs rearrange into LIPs) is much steeper than that assumed for spheres. Charge separation then always slows down with increasing distance, independent of the magnitude of the driving force. As a consequence, non-Markovian unified theories of charge separation and charge recombination [Burshtein, 2000; Kakitani et al., 1995; Gladkikh et al., 2005], which take the time dependence of the distribution of distances between the reactants into account, should be refined to include orientational degrees of freedom in V.

5 Bimolecular Proton Transfer

Small ions like bicarbonate, HCO_3^-, and cyanate, OCN^-, tend to form acids that are unstable in aqueous solution. For this reason, direct observation of aqueous carbonic acid, H_2CO_3, cyanic acid, HOCN, and isocyanic acid, HNCO, has proven to be elusive. In combination with short-laser-pulse excitation, photoacids provide a powerful tool for the transient generation and characterisation of such unstable acids.

5.1 Photoacids

The discovery of photoacidity 60 years ago goes back to Förster [Förster, 1949, 1950, 1970] who related the unusually large Stokes shift found in the fluorescence spectra of several classes of aromatic dyes to excited state proton transfer (ESPT). The excited state proton transfer leads to fluorescence emission from the generated product, namely the conjugate photobase. Such aromatic molecules - so-called photoacids - exhibit enhanced acidity when promoted to their excited electronic state. If the excited state lifetimes of both photoacid and conjugate photobase is long compared to the rate constants for the dissociation and geminate recombination reactions, an excited state acid-base equilibrium is reached. In this case, photoacids resemble ground-state acids which makes it possible to express their excited state acidities quantitatively with the help of the Förster cycle (Figure 5.1) based on thermodynamic considerations [Pines and Pines, 2007]. The strength of a ground-state acid is quantified by its acidity constant K_a, defined as the equilibrium constant for the proton dissociation in water [Atkins,

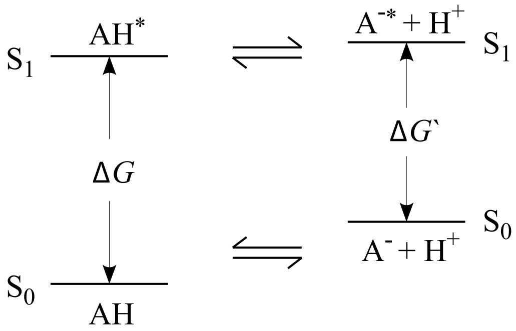

Figure 5.1: Scheme of the reversible Förster cycle. S_0: ground state, S_1: first singlet excited state, ΔG and $\Delta G'$: free energy changes for the transition from the ground state to the first singlet state of the photoacid AH and its conjugated anion A^-, respectively.

1990]:

$$K_a = \frac{[\mathrm{H_3O^+}][\mathrm{A^-}]}{[\mathrm{AH}]}. \tag{5.1}$$

Usually it is expressed in logarithmic units:

$$pK_a = -\log_{10} K_a. \tag{5.2}$$

Within the Förster cycle it is assumed that electronic excitation of a photoacid shifts its ground state acidity constant K_a to an excited state acidity constant K_a^* so that the latter can be similarly defined thermodynamically:

$$K_a^* = \frac{[\mathrm{H_3O^+}][\mathrm{A^{-*}}]}{[\mathrm{AH^*}]} \qquad \text{or} \qquad pK_a^* = -\log_{10} K_a^*, \tag{5.3}$$

where an asterisk indicates that the constituent is electronically excited. The pK_a^* value of a photoacid can be determined experimentally by monitoring the change in the fluorescence quantum yield of the photoacid and the conjugate photobase as a function of sample pH in case the acid-base equilibrium is not affected by proton quenching. Time-resolved spectroscopy can reveal the unimolecular proton-dissociation rate constant k_r^* and the bimolecular proton-recombination rate constant k_d^* of the excited photoacid which gives the excited state equilibrium constant using the relation:

$$pK_a^* = -\log_{10}\left(\frac{k_d^*}{k_r^*}\right). \tag{5.4}$$

Apart from these two direct experimental methods the pK_a-jump upon electronic excitation can be estimated from absorption and fluorescence spectra:

$$\Delta pK_a^* = pK_a - pK_a^* = \frac{\Delta G - \Delta G'}{RT \ln 10}, \tag{5.5}$$

which is schematically presented in Figure 5.1. The pK_a of the photoacid in the excited state is usually lowered by six to seven units compared to the ground state pK_a value. Among a multitude of photoacids the commonly used belong to the three families that were introduced by Förster and Weller [Weller, 1961; Förster, 1949, 1950, 1970]: the naphthols, the pyrenols and the aminopyrenes (Figure 5.2). Naphthols and pyrenols are neutral photoacids. Their excited-state dissociation leads to the formation of an ion pair which subsequently dissociates into a fully solvated proton and the anion of the photoacid:

$$\mathrm{ROH^*} \rightleftharpoons \mathrm{RO^{*-}H^+} \rightleftharpoons \mathrm{RO^{*-}(aq)} + \mathrm{H^+(aq)}. \tag{5.6}$$

Aminopyrenes are strong cationic photoacids that need to be protonated in the electronic ground state in order to undergo isoelectric proton transfer after electronic excitation:

$$\mathrm{RNH_3^{*+}} \rightleftharpoons \mathrm{RNH_2^{*}H^+} \rightleftharpoons \mathrm{RNH_2^*(aq)} + \mathrm{H^+(aq)}. \tag{5.7}$$

The field related to photoacids evolves and spreads into different branches, the elucidation of proton transfer rates and mechanism attract considerable interest. No matter if photoacids are used as probe molecules or the phenomenon photoacidity itself is under study in order to reveal its underlying cause, generalisation of experimental findings into one theoretical model should be treated with caution. It has been shown that cationic photoacids behave differently than neutral photoacids in many ways [Pines and Pines, 2007; Spry and Fayer, 2008]. Neutral photoacids dissociate mainly in water whereas for cationic acids the proton transfer rate constant can even increase when adding organic solvent to water [Pines and Pines, 2007]. Also the underlying origin for photoacidity is discussed to be different for neutral and cationic acids [Spry and Fayer, 2008].

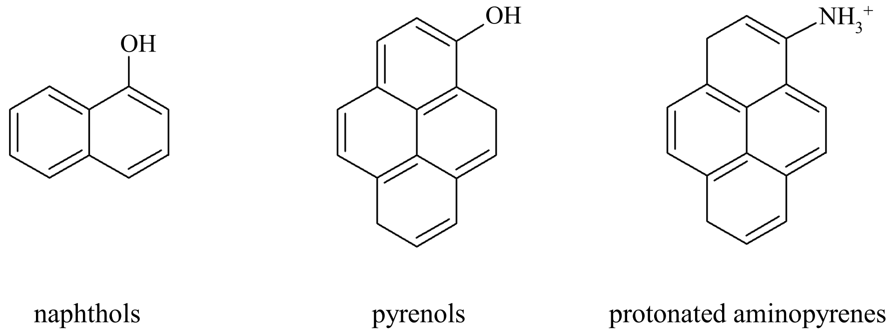

Figure 5.2: Commonly used families of photoacids.

Neutral Photoacids

Much research has been devoted to find evidence for the general validity of the Förster cycle [Pines and Pines, 2007, 2002]. Pines and Huppert [Pines and Huppert, 1986] were the first to report on experimental indication for microscopic reversibility of excited-state proton transfer. They interpreted the deviation from a pure exponential decay of the fluorescence of excited HPTS in aqueous solution as due to reversible excited-state geminate proton recombination reaction. Over a long period, repeated cycles of dissociation-recombination occur in the excited state leading to a pseudo-equilibrium. The equilibrating system is continuously perturbed by the gradual separation of the ion pair by diffusion which results in a power-law decay of the photoacid concentration at long times [Pines et al., 1988; Agmon et al., 1988]:

$$[\mathrm{AH}^*]_t \propto K_a^*(4\pi D t)^{-3/2}, \tag{5.8}$$

where D is the mutual diffusion coefficient between the proton and the conjugate photobase and t is the time elapsed from the moment of the initial dissociation of the photoacid. This equation holds when two conditions are fulfilled, namely when no proton quenching occurs and the excited-state lifetimes of photoacid and conjugate photobase are equal. The influence of the excited-state geminate recombination reaction on the observed excited-state dissociation rate constant k_d^* results in a dependence of k_d^* on the salt concentration of the solution [Pines and Huppert, 1989; Pines et al., 1991]. The introduction of salt to an aqueous photoacid solution affects the probability to escape neutralisation of the ion pair due to screening of the Coulomb interaction between the geminate proton and the conjugate photobase. The influence of the recombination reaction on the overall dissociation dynamics thus decreases leading to a smaller proton dissociation lifetime. However, the decrease of the proton dissociation lifetime levels off at a certain salt concentration due to another effect that counteracts against the already mentioned one. The solvation of salt ions lowers the activity of the aqueous solution resulting in an increase of the pure proton dissociation lifetime of the photoacid. Further increase in the salt concentration will eventually cause an increase in the observed proton dissociation lifetime. According to the above relation (5.4) the excited-state pK_a^* of a photoacid depends on the electrolyte concentration of the solution. The same is true for the ground-state pK_a.

One of the early targets in photoacid research has been the direct measurement of the reaction rate for proton transfer to solvent (PTTS) and with that the elucidation of proton-solvation as well as the proton transfer mechanism. When probing proton solvation dynamics broadband infrared absorption is expected. The reason is twofold: first, the proton is hydrated in many different configurations which dynamically exchange [Marx et al., 1999]. Second, gas phase studies on hydrated proton clusters revealed that the hydration environment influences the infrared-active vibrational resonances of the hydrated proton [Headrick et al., 2005]. Therefore the identification of the hydrated proton still poses a challenge. In several time-resolved measurements using UV-pump/IR-probe spectroscopy, electronic excitation of the photoacid HPTS in water yielded a transient infrared continuum absorption throughout the 1400 - 3000 cm^{-1} spectral range within the experimental time resolution of about 150 - 200 fs [Mohammed et al., 2005a; Siwick and Bakker, 2007; Siwick et al., 2008; Cox and Bakker, 2008]. Mohammed *et al.* assigned this signal to the OH stretching frequency of HPTS [Mohammed et al., 2005a] whereas another physical interpretation was given by Bakker and co-workers. They attributed the continuum absorbance change to the acidic proton [Siwick and Bakker, 2007; Siwick et al., 2008; Cox and Bakker, 2008]. Directly after electronic excitation of HPTS, the covalent OH-bond in HPTS is weakened and a strengthening of the hydrogen bond to the solvating water occurs. This polarisable hydrogen bond leads to the observed IR continuum absorbance change. When the proton

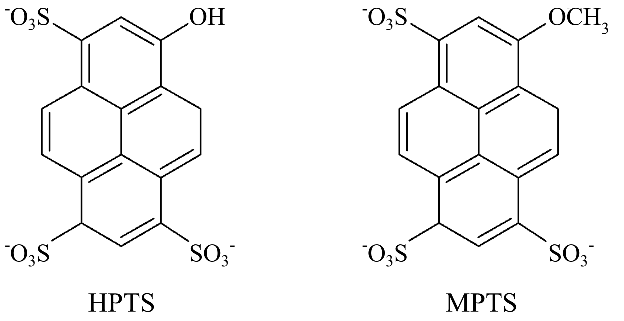

Figure 5.3: Molecular structures of HPTS (8-hydroxy-3,6,8-trisulfonate) and MPTS (8-methoxy-3,6,8-trisulfonate), respectively.

leaves the photoacid and transforms to a fully hydrated state the measured continuum absorbance change will decrease in case the IR cross section is higher for the polarisable hydrogen bond than for the fully hydrated proton. The observed dynamics reflect therefore the proton solvation time. Bakker and co-workers monitored this transient continuum absorption in order to reveal finer details on acid-base reactions regarding the proton transfer mechanism. With that they introduced a “Grotthuss Hopping Model for Intermolecular Proton Transfer”.

Using the methoxy-derivative of HPTS, MPTS, with the molecular structure shown in Figure 5.3 it is possible to answer the question if the broadband continuum absorption change is due to a solvated proton. Since MPTS does not dissociate upon electronic excitation this signal should not be detected. Figure 5.4 shows a comparison between the transient absorption spectra recorded for MPTS and HPTS. It shows an infrared continuum absorbance change after electronic excitation which is the same for HPTS and MPTS in both amplitude and dynamics [Mohammed et al., 2009b]. This careful examination of the infrared continuum transient absorption, however, raises doubts about the given physical interpretation on the signal. It is worth mentioning that 2-Naphthol-6,8-disulfonate (2N-6,8S) also shows the transient continuum absorption signal upon photoexcitation. It is the photoacid which is used for the studies on acid-base neutralisation reactions in water as discussed in subsequent sections. 2N-6,8S was chosen because of its appropriate pK_a-values in the ground and excited state. In order to extract reliable reaction kinetics from the time resolved measurements the dynamics of the monitored vibrational marker modes had to be disentangled from the dynamics of the underlying transient continuum absorption. Lineshape fitting with a Gaussian-function on a straight line has been used to separate the different contributions.

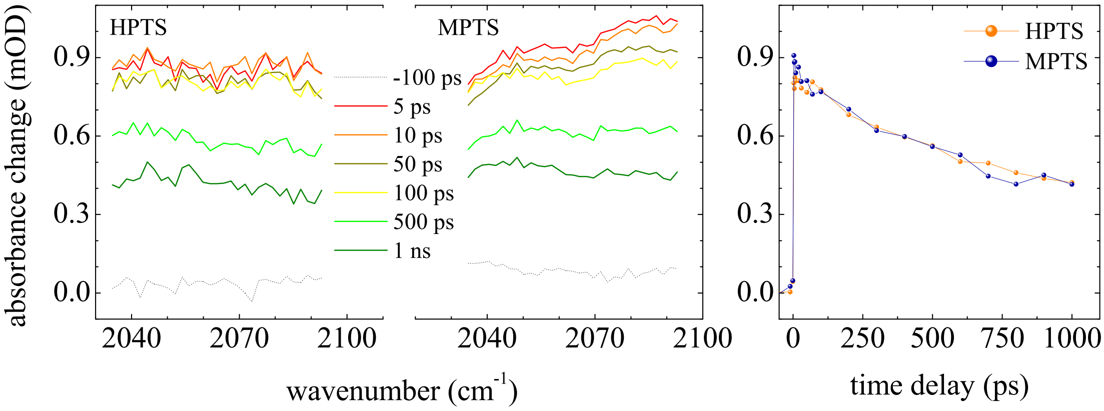

Figure 5.4: Comparison between the transient continuum absorption after electronic excitation of HPTS and MPTS in H_2O at $pH = 1$, respectively. The transient spectra are shown on the left and in the middle whereas the compared kinetics are displayed in the right panel.

5.2 Characterisation of 2-Naphthol-6,8-disulfonate

Experimental

The laser, the parametric amplifiers for the generation of the ultraviolet pump and infrared probe pulses as well as the experimental setup is described in detail in chapter 2. Electronic excitation was achieved with pump pulses of 2 μJ energy, 50 fs duration at a central wavelength of 330 nm. The mid-infrared probe pulses were tuned between 1350 cm^{-1} and 1700 cm^{-1} in order to monitor the evolution of the vibrational marker modes associated with the photoacid and its conjugate photobase. With the help of a zero-order half-wave plate the polarisation of the pump pulses was rotated so as to measure at magic angle condition to eliminate signal contributions due to orientational relaxation of the excited molecules. The monitored vibrational marker modes are located in a spectral region where water absorbs due to the OH bending vibration. Deuterated water was employed allowing for the measurement using a 50 μm thick sample. The concentration of 2-naphthol-6,8-disulfonic acid, dipotassium salt hydrate (2N-6,8S; ABCR) in deuterium oxide (Deutero; 99.8 %) was kept at 50 mM with a pD of about 5.

Results & Discussion

The photoacid 2-Naphthol-6,8-disulfonate changes its pK_a value by about 8 units from $pK_a = 9.3$ - 9.4 to $pK_a^* = 1.0$ - 1.3 at 0 M ionic strength in deuterated water allowing for real-time observation of deuteron transfer to solvent (DTTS) (Figure 5.5) in deuterated water and deuteron transfer to base (DTTB). Figure 5.6 shows the electronic absorption spectra of photoacid and conjugate photobase, respectively. Both forms exist in solution depending on its pH (pD) value. At $pH = 1$, 2N-6,8S surely exists in the photoacid form whose electronic absorption spectrum is displayed as black line whereas the conjugate photobase is present at $pH = 12.8$ giving the corresponding spectrum as grey line. The fluorescence spectrum after excitation of the photoacid form at pH of about 8 equals the fluorescence spectrum of the photobase form as shown as grey dots, typifying the Förster cycle. The experimental identification of vibrational bands marking the photoacid and conjugate photobase conformations of 2N-6,8S in the electronic excited state has been carried out by measuring transient infrared spectra of 2N-6,8S in D_2O solution at two different pD values (Figure 5.7). The early time response after excitation of 2N-6,8S at $pD = 5$ reveals vibrational modes of the photoacid in the electronic excited state as positive absorbance changes. A comparison with the steady-state infrared spectrum of the photoacid indicates frequency shifts and alterations in IR cross sections when promoting the photoacid from the electronic ground state to the electronic excited state

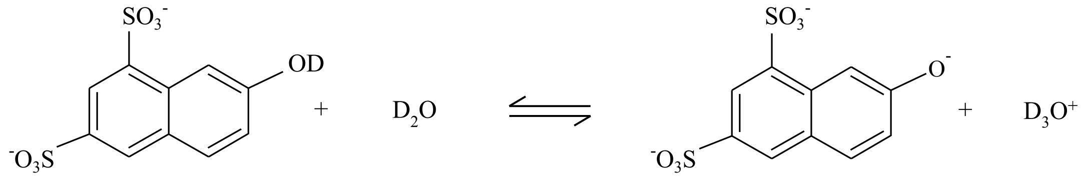

Figure 5.5: The reaction scheme shows the deuteron transfer to solvent in D_2O.

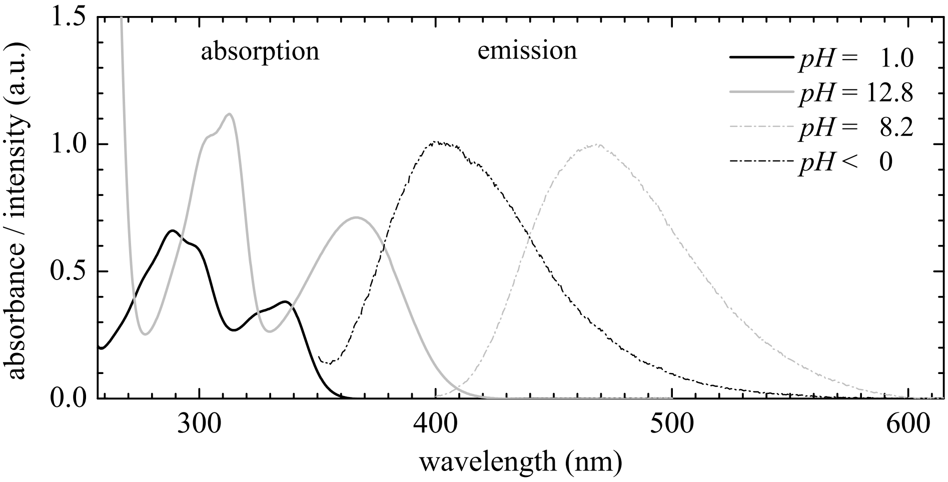

Figure 5.6: Electronic absorption spectra of 25 mM 2N-6,8S in H_2O (sample thickness 50 μm) as function of pH. Both photoacid (black solid line) and photobase (grey solid line) forms absorb at 330 nm, with different cross sections favouring the photoacid form. The fluorescence spectra of the photoacid form and its conjugate photobase is shown in black and grey dots, respectively.

in the spectral range between 1300 cm^{-1} and 1700 cm^{-1}. The bleach signal at about 1630 cm^{-1} due to depletion of photoacid ground state population indicates a strong IR-active mode of electronic ground state 2N-6,8S confirmed by the steady-state infrared spectrum. At long pulse delay the vibrational mode pattern changes significantly due to the deuteron transfer to the solvent transforming the photoacid into its conjugate photobase. This is in full accordance to the transient vibrational spectrum measured after excitation of 2N-6,8S at $pD = 12$: when only the conjugate photobase is present. For a reasonable comparison of these two transient vibrational spectra one has to take into account the modes of electronic ground state 2N-6,8S in the particular conformation as can be seen in Figure 5.7 (a) for the photoacid conformation and (d) for the conjugate photobase, respectively. This careful experimental analysis of the transient vibrational spectra considering ground state spectra of 2N-6,8S allows for the determination of one marker mode corresponding to the photoacid form of 2N-6,8S in the S_1-state, located at 1472 cm^{-1}. Another photoacid marker mode at 1502 cm^{-1} is replaced by a photobase band at 1510 cm^{-1} with a higher absorbance strength. A second, spectrally resolved marker mode for the photobase conformation is located at 1410 cm^{-1} which has a similar magnitude as the other photobase band at 1510 cm^{-1}. With this it is possible to follow the full Förster cycle of 2N-6,8S through IR-active vibrational modes, where the electronic excited states of 2N-6,8S decay with a 10 ns and 12 ns time constant, for the photoacid and photobase forms, respectively. Transient spectra of 2N-6,8S in D_2O have been recorded as a function of pump-probe delay and a section of these spectra is plotted in Figure 5.8 with a detailed presentation of the early time delays from 0.5 ps to 5.0 ps on the left panel. The transient spectra show a decrease of band strengths of the three bands at 1472 cm^{-1}, 1502 cm^{-1} and the bleach signal at 1519 cm^{-1} on a short time scale of a few picoseconds. On this time scale deuteron transfer has not taken place as can be seen by the missing conjugate photobase signals at 1410 cm^{-1} and

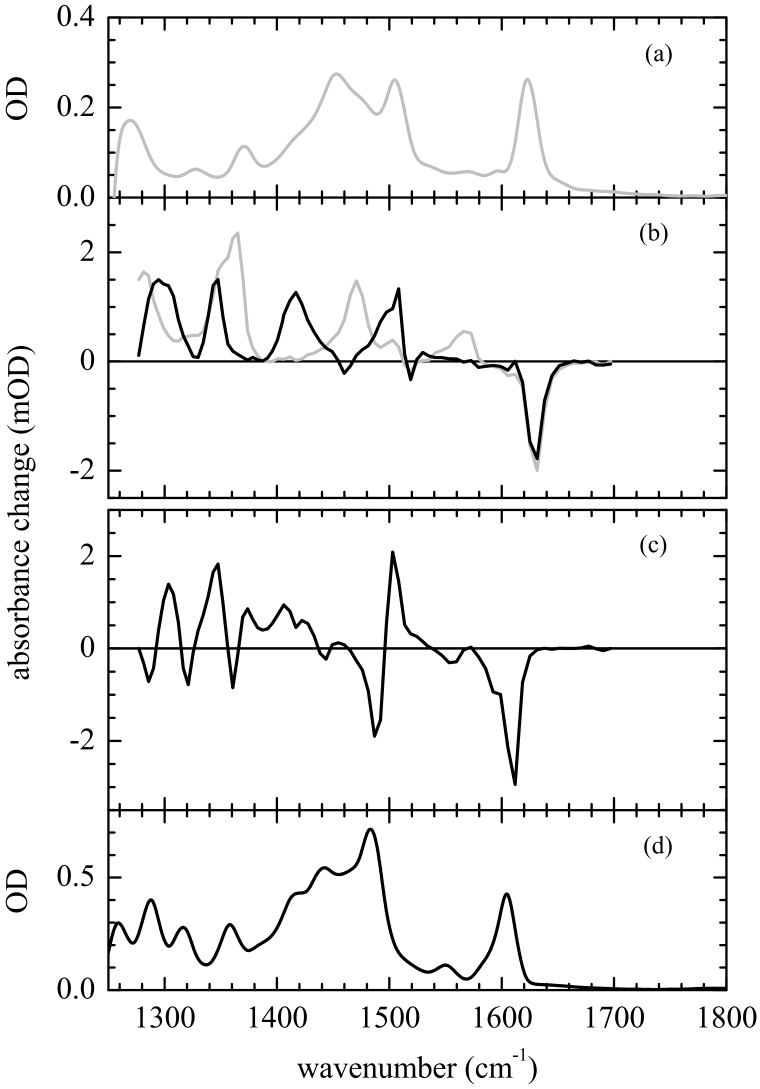

Figure 5.7: Comparison of the steady-state IR spectra of the photoacid form of 2N-6,8S in the electronic ground state (a), and the transient IR spectrum upon electronic excitation (b), measured at early pulse delay (1 ps) where the photoacid form prevails (grey curve) and at long pulse delay (1 ns), when the conversion into the conjugate photobase in the S_1-state has completed (black curve). The steady-state (d) and transient IR spectra (c) of the photobase form of 2N-6,8S, show the location of fingerprint vibrations in the S_0 and S_1-states.

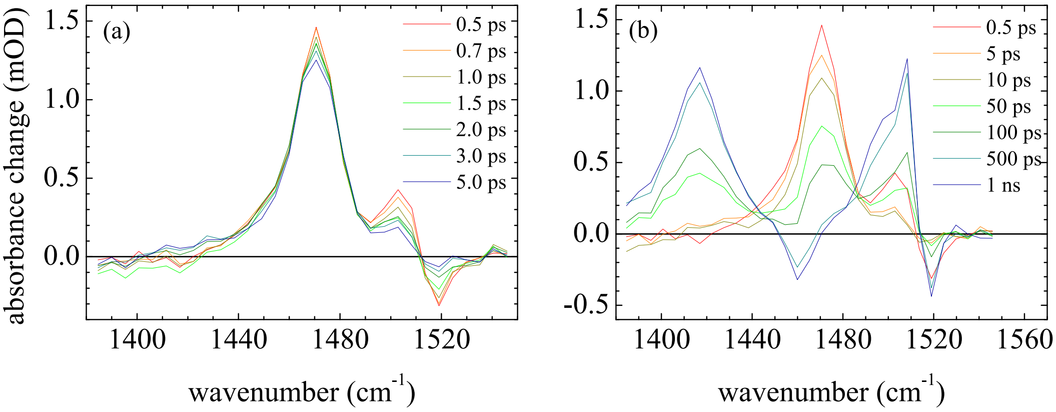

Figure 5.8: Differential absorption spectra of 2N-6,8S in D_2O at short time delays (a) and at long time delays up to 1ns (b).

1510 cm^{-1}. It is likely that these initial dynamics is caused by solvent rearrangements and/or crossover between electronic states [Tran-Thi et al., 2000; Hynes et al., 2002; Tran-Thi et al., 2002; Spry and Fayer, 2008; Knochenmuss et al., 1999; Magnes et al., 1999]. However, it is beyond the scope of this thesis to discuss the question on the nature of photoacidity for this particular photoacid. Seeing that deuteron transfer happens on a much slower time scale (Figure 5.8 (b)), it is possible to reveal more insight into it. The time evolution of the absorbance change at 1410 cm^{-1} and 1510 cm^{-1} as well as the inverted signal at 1472 cm^{-1} are shown in Figure 5.9. Apparently, all three transients follow identical kinetics proving that the short time dynamics on the photoacid band at 1472 cm^{-1} can be neglected. The deuteron transfer time to the solvent can be extracted

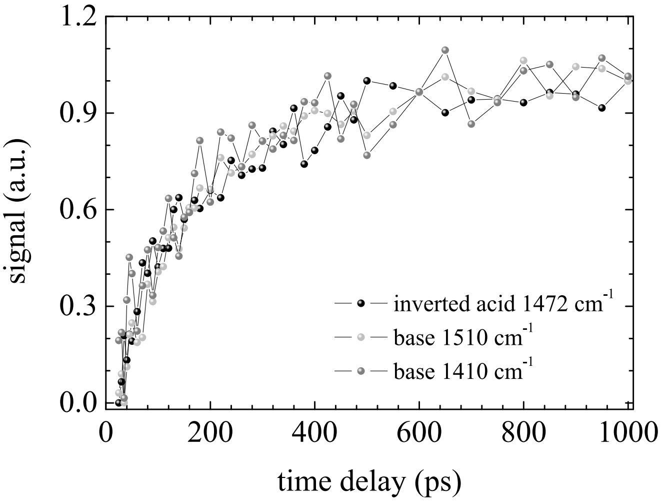

Figure 5.9: Comparison of the population kinetics of the inverted photoacid 1472 cm^{-1} band (black circles), of the photobase 1510 cm^{-1} (light grey circles) and of the photobase 1410 cm^{-1} band (dark grey circles).

from the fits to the three transients yielding 200 ps. This knowledge about the time evolution of the genuine marker modes of 2N-6,8S photoacid and conjugate photobase in deuterated water gives insight into deuteron transfer to the solvent. The next sections will focus on the dynamics in presence of a base.

5.3 Isocyanic acid versus cyanic acid

Protonation of cyanate, OCN^-, in aqueous solution is thought to result in two different products: isocyanic acid, which is the most stable (HNCO, $pK_a = 3.7$ [Boughton and Keller, 1966]) and cyanic acid (HOCN, $pK_a < 3$ [Pankratov and Khmelev, 2005a,b]) which is not thought so strongly unfavourable as to be safely excluded. Indeed both HNCO and HOCN as shown in Figure 5.10 have been considered in quantum chemical calculations on acidity properties [Pankratov and Khmelev, 2005a,b], and in charge transfer complexes with water or ammonia [Park and Woon, 2004].

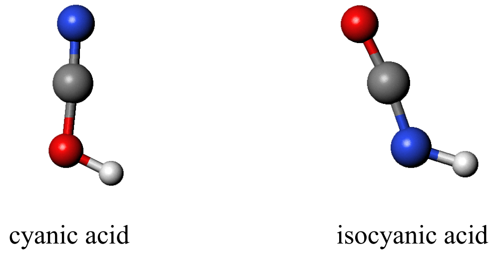

Figure 5.10: Structures of cyanic acid, HOCN, and isocyanic acid, HNCO. Relation between colour and atom: Blue: N; White: H; Grey: C; Red:O.

It is the aim of this section to find out how much of both reaction products, cyanic acid and isocyanic acid are formed upon transient protonation at early time delays, and whether the on-contact reactive complex between the photoacid (2N-6,8S) and cyanate has a well-defined structure [Adamczyk et al., 2009a]. Using the Szabo-Collins-Kimball approach to describe bimolecular reaction dynamics subject to the Debye-von Smoluchowski diffusional motions, an on-contact proton transfer reaction rate is derived.

Introduction

The existence of HNCO and HOCN is an issue in the determination of solid-phase protonation and deprotonation processes of small molecules in interstellar ice [Schutte and Khanna, 2003; Raunier et al., 2003a,b,c, 2004]. Moreover, both, HNCO and HOCN, have to be considered as intermediates in the hydrolysis of cyanate [Amell, 1956; Vanderzee and Myers, 1961], where carbamic acid (H_2NCOOH) may be the precursor of the final products CO_2 and NH_3 (Figure 5.11 (a)). Alternate reaction pathways involving cyanate may have to be taken into account, if only as transient population build-ups of cyanate and (iso-)cyanic acid also in the case of aqueous formation of carbamate [Brooker and Wen, 1993; Park et al., 2008]. Similarly, HNCO and HOCN, might be involved as intermediates in the classic Wöhler synthesis [Wöhler, 1828; Liebig and Wöhler, 1830; Dunitz et al., 1998; Tsipis and Karipidis, 2003], where ammoniumcyanate converts into urea (H_2NCONH_2) in aqueous solution via an ammonia addition mechanism. The same is true for the reverse reaction pathway of decomposition of urea [Lynn, 1965; Alexandrova and Jorgensen, 2007], where NH_3 elimination is understood to prevail above hydrolysis (Figure 5.11 (b)). Detailed knowledge on the reaction mechanisms of Figure 5.11 may also be relevant for other means of urea synthesis. For instance using direct addition of NH_3 and CO_2 followed by elimination of H_2O is understood to occur under industrial scale high pressure and temperature conditions [Buckingham et al., 1986; Ramachandran et al., 1998]. In biological environments, hydrolysis of urea is catalysed by the urease enzyme [Karplus et al., 1997]. The elimination mechanisms in urease that are competitive to hydrolysis [Estiu and Merz, 2007] might also involve transient population build-ups of cyanate and (iso-)cyanic acid.

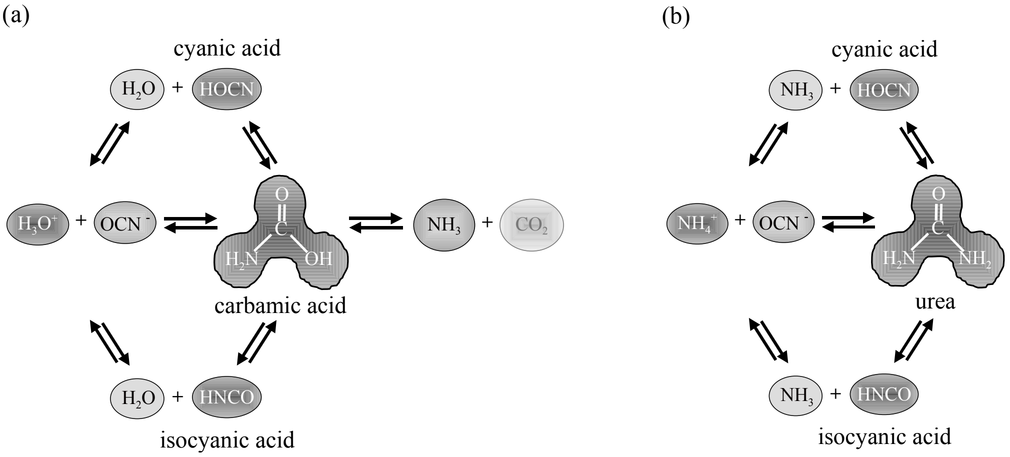

Figure 5.11: Reaction pathways where OCN^- reacts with H_3O^+ (a) or NH_4^+ (b), forming carbamic acid or urea, respectively. Reaction pathways may include protonation steps leading to either HOCN or HCNO, but may also involve direct addition pathways. Carbamic acid is not stable in aqueous solution: it dissociates into NH_3 and CO_2.

Until now, isocyanic acid is the best characterised of the four possible [C,H,N,O] isomers [Belson and Strachan, 1982; Teles et al., 1989; Pinnavaia et al., 1993]. Recent ab initio quantum chemical calculations have shown that isocyanic acid (HNCO) is at least 24 kcal mol^{-1} more stable than cyanic acid (HOCN), whereas fulminic acid (HONC) and isofulminic acid (HCNO) have even higher heats of formation [Schuurman et al., 2004; Mladenović and Lewerenz, 2008]. As a result, much spectroscopic data refers to isocyanic acid, an early example is the gas phase infrared study by Herzberg and Reid [Herzberg and Reid, 1950]. Whereas isocyanic acid can readily be measured in the condensed phase using infrared spectroscopy [Nelson, 1970], the other isomers have only be characterised using low temperature matrices as trapping media [Raunier et al., 2003a; Teles et al., 1989; Jacox and Milligan, 1964; Bondybey et al., 1982].

Experimental

Femtosecond mid-infrared experiments were performed using 100 ml solutions consisting of 50 mM 2N-6,8S (2-Naphthol-6,8-disulfonic acid dipotassium salt hydrate; 80 %, ABCR) in distilled water. The concentrations of sodium cyanate (Aldrich) used were 0.5 M, 1 M and 1.5 M. In order to control sample degradation due to the chemical instability of aqueous HNCO/HOCN on a long time scale the solutions were buffered with TRIS, (tris(hydroxymethyl)aminomethane saline Fluka, tablets, *pH* 7.6 ± 0.2 (25°C), 0.05 M TRIS/HCl, 0.15 M NaCl) and UV-spectra were taken before and after each measurement (Figure 5.12). Electronic excitation was achieved with pump pulses of 1.7 μJ energy, 60 fs duration at a central wavelength of 336 nm. The mid-infrared probe pulses were tuned between 2000 cm^{-1} and 2500 cm^{-1} in order to monitor the evolution of the vibrational marker modes associated with either cyanic and/or isocyanic acid. Transient spectra were taken in the spectral range with centre frequency at 2273 cm^{-1} and spectral resolution of 3 cm^{-1}. In order to guarantee a homogeneously pumped volume of the 50 μm thin sample the beam diameters at the sample position were set to 300 μm and 200 μm for pump and probe beams, respectively. The time resolution was determined to be 250 fs. With the help of a zero-order half-wave plate the polarisation of the pump pulses was rotated so as to measure at magic angle condition to eliminate signal contributions due to orientational relaxation of the excited molecules.

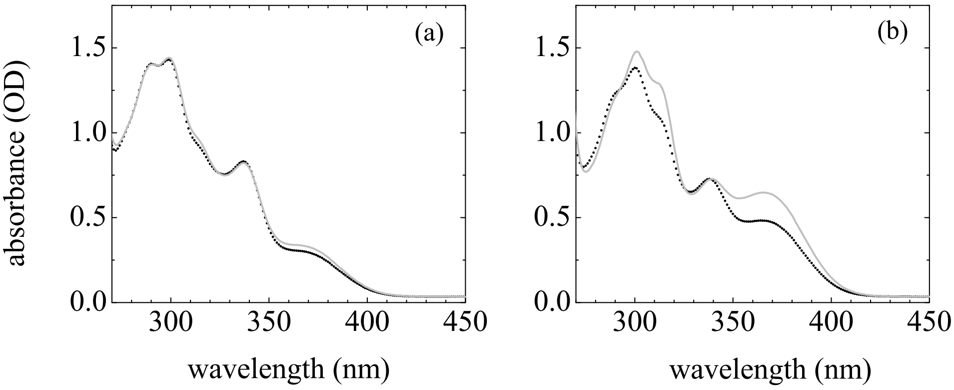

Figure 5.12: Electronic absorption spectra of the 50 μm thick solutions containing 50 mM 2N-6,8S and 0.5 M (a) and 1.5 M (b) OCN^{-} in H_2O used in the experiment. The black dotted curve shows the spectrum measured just before the time-resolved experiment, and the grey solid curve indicates the spectrum measured after 95 min., the duration of the time-resolved experiment.

Results & Discussion

The distinction whether cyanic or isocyanic acid is transiently generated relies on the identification of vibrational marker modes at different designated frequencies, preferably spectrally resolved. For this infrared spectra were calculated at optimised structures for HOCN and HNCO by J. Dreyer. Density functional theory (DFT) with the B3LYP functional [Lee and Yang, 1988; Miehlich et al., 1989; Becke, 1993; Hertwig and Koch, 1997] and the 6-31+G(d,p) basis set as implemented in Gaussian 03 [Frisch et al., 1998] were used for geometry optimisation and normal mode calculations. The analysis reveals six vibrational normal modes of each isomer (Figure 5.13).

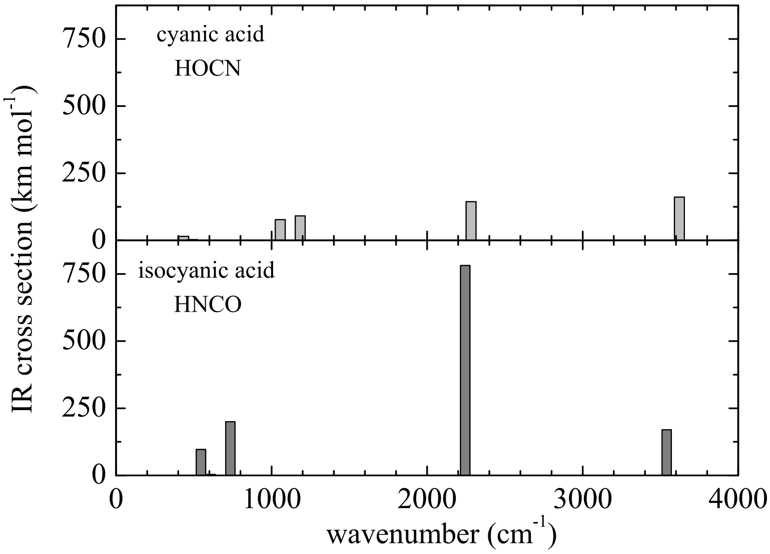

Figure 5.13: Calculated IR-active vibrational spectrum of HOCN and HNCO.

the OH- and NH- stretching vibrations corresponding to HOCN and HNCO isomers, respectively are located between 3500 cm^{-1} and 3600 cm^{-1}. The cyanate- (HNCO) and cyano-stretching (HOCN) modes are found around 2250 cm^{-1} to 2300 cm^{-1} and the four bending vibrations of the two isomers can be detected between 400 cm^{-1} and 1300 cm^{-1}. Both the bending vibrations and the OH- or NH-stretching modes are located in spectral regions which are challenging to probe due to spectral overlap with the librational modes and the broad OH stretching mode of H_2O, respectively. However, the cyanate- and cyano-stretching modes can readily be probed, as only the combination overtone of H_2O has a weak absorption in this spectral range. The calculated cyano-stretching - ν(CN) - frequency for HOCN is 2282 cm^{-1} whereas HNCO exhibits a cyanate stretching mode, ν(O=C=N), centred at 2245 cm^{-1}. These values will be shifted due to hydrogen bond formation with the solvent. Indeed, the frequencies obtained with low temperature matrix studies of HOCN and HNCO clusters with water were 2295 cm^{-1} for HOCN and 2252 cm^{-1} for HNCO [Raunier et al., 2003a]. Moreover, the cyano stretching mode of OCN$^-$ is located at 2172 cm^{-1}. With typical spectral bandwidths for vibrations of small molecules in the solution phase of 20 - 30 cm^{-1}, it should be possible to probe all distinct species: HOCN, HNCO and OCN$^-$ dissolved in H_2O using time-resolved infrared spectroscopy. However, since the cyanate stretching mode of HNCO has an infrared absorption cross section that is 5.4 times higher than the cyano stretching mode for HOCN, one has to scale transient signals accordingly. Figure

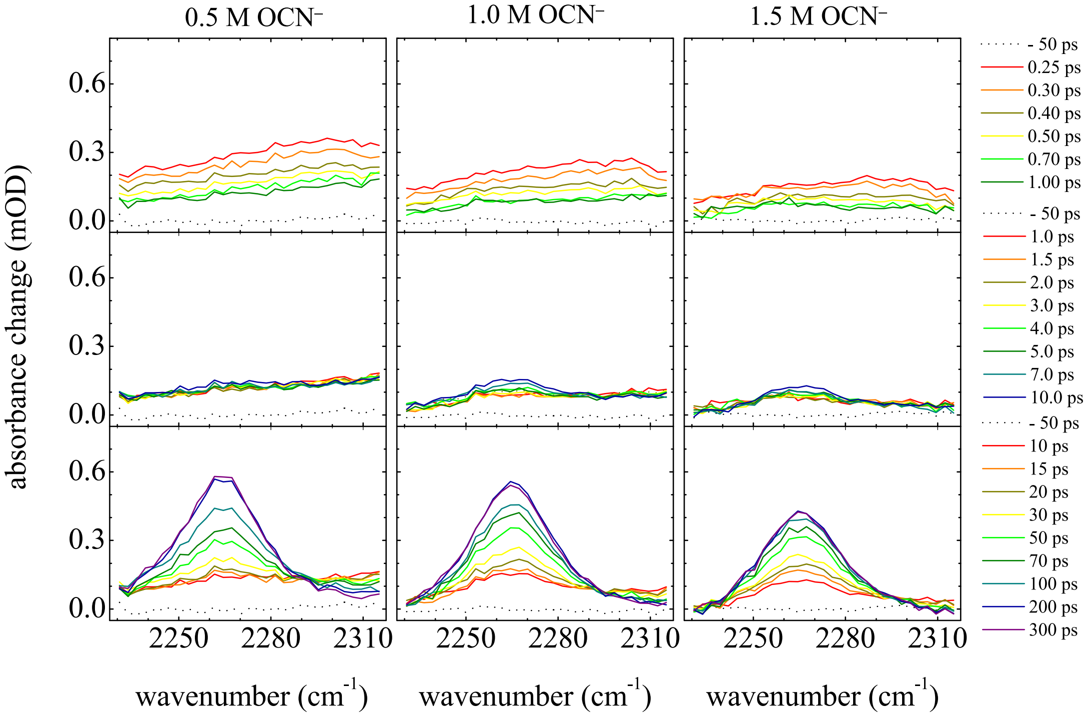

Figure 5.14: Transient IR spectra measured in the cyanate/ cyano-stretching region of HNCO/HOCN. The three columns indicate the response measured for three OCN^- concentrations. For each OCN^- concentration three plots indicate the response in three different temporal regimes.

5.14 shows the transient infrared spectra recorded for three cyanate concentrations from 0.5 M to 1.5 M. For each concentration present three panels are presented: one with the transient response within 1 ps pulse delay time, one with the signals recorded at pulse delays of several picoseconds, and one with the response measured at longer delay times of tens to hundreds of picoseconds. It is evident from these transient spectra that apart from the broadband featureless signal appearing directly upon photoexcitation of 2N-6,8S no instantaneous rise of the cyanate/ cyano-stretching bands of HNCO or HOCN can be observed. The existence of hydrogen bonded tight complexes $ROH\cdots OCN^-$ and $ROH\cdots NCO^-$ can thus be excluded as they would have led to a temporal resolution limited rise of the HOCN or HNCO marker mode signals. Instead, it is only on picosecond time scales, with rise times dependent on the concentration of OCN^-, that a transient band appears located at 2265 cm^{-1}, very close to the value reported for $HNCO\cdots H_2O$ complexes in low temperature argon matrices [Raunier et al., 2003a]. Within the measurement accuracy, no transient band around 2290 cm^{-1} is observed that could be indicative of transient population of HOCN. This experimental result reveals information on the structure of the photoacid-base complex. The O-side of OCN^- has a sufficient base strength and anionic charge density (about 0.8 e compared to about 0.9 e of the N side [Park and Woon, 2004]) that proton transfer should happen provided a proper long-lived alignment in a rigid $ROH\cdots OCN^-$ complex occurs. Likely, the reactive complex between 2N-6,8S and OCN^- is very flexible and not well structured, unlike the situation between pyranine and the carboxylate bases [Rini et al., 2003, 2004; Mohammed et al., 2005b, 2007a,b], where tight and loose complexes with well-defined structures could be detected. Not for 2N-6,8S-cyanate photoacid-base pairs: just like tight complexes loose complexes of the type $ROH\cdots H_2O\cdots OCN^-$ and $ROH\cdots H_2O\cdots NCO^-$ can be excluded as no signal at 2570 cm^{-1} was observed. This suggests that such hydrogen bonded complexes between 2N-6,8S, water and OCN^- are not long-lived. The acid and base approach each other by diffusion, but are not colliding directly or forming a long-lived hydrogen-bonded complex. Although there is roughly an equal chance to approach the acid from the N or O terminal both from steric and electrostatic point of view, only the protonation reaction at the N-side has been detected. This means that the rate of the proton transfer to the N-terminal is at least one order of magnitude faster than to the O-terminal. The other possibility is that the two terminals react with similar rate constants but the protonated O-terminal dissociates much more rapidly than the protonated N-terminal. But it would imply that the dissociation rate of the O-terminal is on the order of a few picoseconds. Both kinetic scenarios lead to the conclusion that in aqueous solution protonation of OCN^- results in HNCO rather than HOCN, as experimentally is observed. The experimental kinetic data also suggest that the acidity of HOCN is much higher than HNCO (pK_a-value of HOCN is at least one unit lower than that of HNCO). It can be concluded that the equilibrium between the two isomers is likely to be controlled by the forward reaction so that the proton transfer reaction leads directly to preferred generation of the more stable product, HNCO, with a lifetime extending way beyond 1 ns.

A Gaussian line shape fitting to the experimental transient spectra derives the true population kinetics of the 2265 cm^{-1} band. The obtained kinetics and the result of

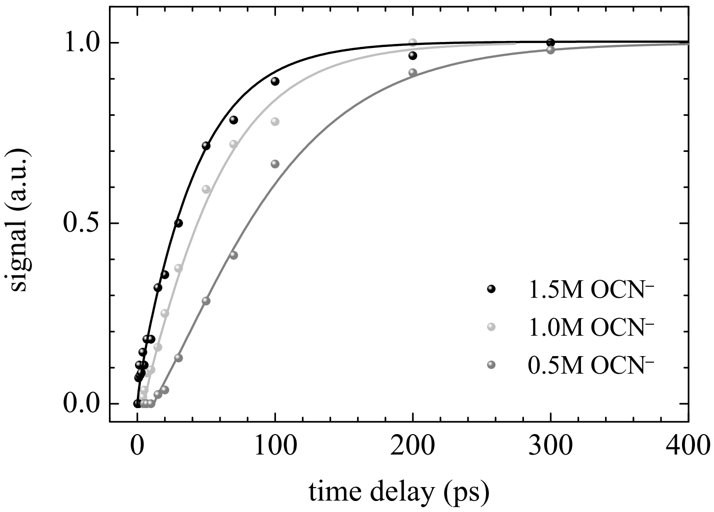

Figure 5.15: Time-dependent rise of the cyano-stretching marker mode of HNCO for three different concentrations of OCN^- (symbols), plus fits using the model described in appendix 5.6 and fit parameter values given in Table 5.1.

the fitting procedure as function of time delay between pump and probe are shown as symbols and solid lines in Figure 5.15, respectively. The values for the fitting parameters are given in Table 5.1.

c (M)	σ_{eff} (Å)	σ'_{eff} (Å)	D $[10^{-9}\mathrm{m}^2\mathrm{s}^{-1}]$	D' $[10^{-9}\mathrm{m}^2\mathrm{s}^{-1}]$	k_w $[10^{10}\mathrm{s}^{-1}]$	k_a $[10^{10}\mathrm{M}^{-1}\mathrm{s}^{-1}]$
0.5	4.0	6.2	2.2	10	1.2	6
1.0	4.4	6.0	2.2	10	1.2	6
1.5	4.6	5.9	2.2	10	1.2	6

Table 5.1: c is the concentration of OCN^-. σ_{eff} is the effective contact distance (including the screened Coulomb interaction with $\sigma = 5.5$ Å) and D is the mutual diffusion constant for 2N-6,8S and OCN^-. σ'_{eff} is the effective contact distance and D' is the mutual diffusion constants for H^+ and OCN^-. k_w is the proton dissociation rate of 2N-6,8S in H_2O, and k_a the on-contact bimolecular reaction rate between 2N-6,8S and OCN^-.

5.4 Carbonic acid

Since the ancient world scientists wondered about the ingredients of mineral water. Aristotle, amongst others, searches for the cause of its effects on health without any results. The first scientific notation of carbonic acid goes back to the flemish doctor Johann Baptist van Helmont (1577 - 1644) [Teuteberg, 2003]. He analysed the mineral water of Spa and made carbon dioxide from potash and chalk. But it was not until the end of the eighteenth century that Antoine Laurent Lavoisier (1743 - 1794) proved that carbon dioxide consists of carbon and oxygen which lead to the term "gas carbonique". The history of carbonic acid is full of confusion: at the end of the nineteenth and beginning of the twentieth century carbon dioxide, CO_2, dissolved in water was considered to only exist in the acid form, H_2CO_3 [Ellms and Beneker, 1901] because of its weak acidic behaviour. Nowadays there are still chemistry textbooks that postulate that pure carbonic acid, H_2CO_3, cannot be isolated because of its ready dehydration to CO_2 [King, 2005]. It will be shown throughout this section that both perspectives are wrong.

Introduction

Dissolution of gaseous CO_2 in pure water leads to aqueous solvation of CO_2,

$$CO_2(g) \rightleftharpoons CO_2(aq), \tag{5.9}$$

which is understood to be accompanied by hydration resulting in carbonic acid, H_2CO_3, and subsequent acid-base chemistry leading to bicarbonate, HCO_3^-:

$$CO_2(aq) + 2\ H_2O \rightleftharpoons H_2CO_3 + H_2O \rightleftharpoons HCO_3^- + H_3O^+. \tag{5.10}$$

The equilibrium constant for the equilibrium between dissolved carbon dioxide and carbonic acid is approximately:

$$K_{CO_2} = \frac{[H_2CO_3]}{[CO_2(aq)]} \approx 2 \cdot 10^{-3}. \tag{5.11}$$

That is why only a minor fraction of dissolved CO_2 exists as carbonic acid, H_2CO_3. In pure water the corresponding equilibrium constant for the first deprotonation of carbonic acid is

$$K_{H_2CO_3} = \frac{[H^+][HCO_3^-]}{[H_2CO_3]} = 1.72 \cdot 10^{-4}\mathrm{M}. \tag{5.12}$$

The first dissociation constant is denoted as $pK_a(1) \approx 3.8$ and referred to as the true dissociation constant of carbonic acid [Wissbrun et al., 1954]. Because of the low concentration of carbonic acid in an aqueous solution of carbon dioxide, the solution is only weakly acidic and the first dissociation constant is often given by

$$K^*_{H_2CO_3} = \frac{[H^+][HCO_3^-]}{[CO_2(aq) + H_2CO_3]} = 4.498 \cdot 10^{-7}\mathrm{M}, \tag{5.13}$$

the first apparent dissociation constant $pK_a^*(1) \approx 6.35$. Carbonic acid is diprotic. Bicarbonate thus deprotonates to carbonate according to

$$HCO_3^- + H_2O \rightleftharpoons CO_3^{2-} + H_3O^+ \tag{5.14}$$

with the second dissociation constant

$$K_{HCO_3^-} = \frac{[H^+][CO_3^{2-}]}{[HCO_3^-]} = 0.479 \cdot 10^{-10}\mathrm{M}, \tag{5.15}$$

$pK_a(2) = 10.32$. The dissociation constants given above are strongly dependent on temperature, pressure and salinity [Millero and Roy, 1997]. The reported values are obtained at a temperature of 25°C, standard pressure and zero salinity. It is obvious that the total dissolved inorganic carbon is distributed among the four components: carbon dioxide, CO_2, carbonic acid, H_2CO_3, bicarbonate, HCO_3^-, and carbonate, CO_3^{2-}. Their relative fractions are determined by the pH-value

$$pH = -\log_{10}[H^+] \tag{5.16}$$

of the aqueous solution as can be seen in Figure 5.16. Note that with the known value of the atmospheric partial pressure of CO_2 ($3.5 \cdot 10^{-4}$ atm) [Millero and Roy, 1997], the total dissolved inorganic carbon can be obtained using Henry's law:

$$K_0 = \frac{[CO_2(aq)]}{p_{CO_2}}. \tag{5.17}$$

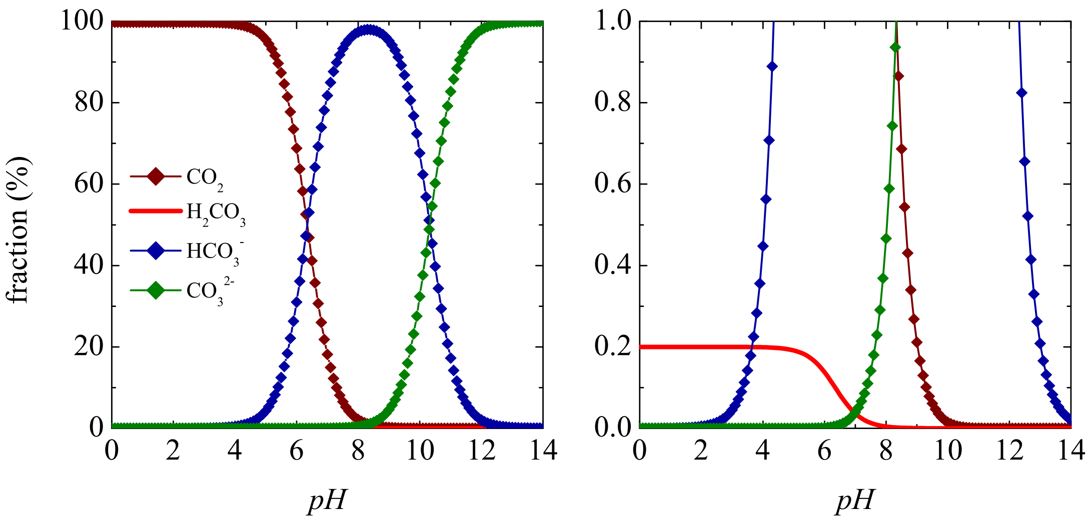

Figure 5.16: Distribution of the four components as percentages of the total dissolved inorganic carbon as a function of the pH ($K_1 = 4.498 \cdot 10^{-7}$ M and $K_2 = 0.479 \cdot 10^{-10}$ M) assuming the system is closed.

The apparent solubility constant K_0 depends on temperature and salinity. Given a value of $3.428 \cdot 10^{-2}$ mol l^{-1} atm^{-1} at 25°C and zero salinity, the concentration of the total dissolved inorganic carbon amounts to $1.2 \cdot 10^{-5}$ M which yields a concentration of carbonic acid of $2.4 \cdot 10^{-8}$ M.

The high solubility of CO_2 in water, the rapid dehydration of carbonic acid resulting in solvated CO_2 and and an optimal pH buffer capacity ranging from 5.1 to 7.1 provide the basis for the vital physiological role of the regulation of the pH-value of blood. Within the relevant pH range following equilibrium reactions are of importance:

$$CO_2(g) + 2\ H_2O \rightleftharpoons CO_2(aq) + 2\ H_2O \rightleftharpoons H_2CO_3 + H_2O \rightleftharpoons HCO_3^- + H_3O^+. \qquad (5.18)$$

In order to prevent acidosis ($pH < 7.35$) the lungs remove excess CO_2 from the blood by respiration exchanging CO_2 with O_2 and consequently lowering the proton concentration. On the contrary, alkalosis ($pH > 7.45$) is prevented by excretion of HCO_3^- through the kidneys in such a way that the equilibrium is shifted towards the right which results in a decrease of the pH-value.

Looking at the Earths' atmosphere water vapour is the most significant greenhouse gas, followed by carbon dioxide and various other greenhouse gases of minor importance like methane, nitrous dioxide, ozone and chlorofluorocarbons. The common spectral properties of all greenhouse gases have been studied in the field of atmospheric research. First, the high transmission in the visible spectral range being almost transparent to solar radiation allows its absorption by the Earths' surface. Second, they absorb and emit infrared light upcoming from the Earth' s surface thereby trapping heat in the surface-troposphere system. In the absence of the natural greenhouse effect the heat energy would leak from the atmosphere and the average surface temperature of 14°C could be as low as -18°C. Consequently, the natural greenhouse effect establishes a moderate climate which is a condition for life on Earth [Ramanathan, 1988].

The aqueous chemistry of carbon dioxide plays a crucial role in the regulation of the CO_2 exchange between atmosphere, hydrosphere, lithosphere and biosphere in order to guarantee a constant CO_2 - concentration, below 1 %, in the atmosphere. The lithosphere is the greatest sink for CO_2 but because of the long storage period its importance lies in the long-term control of the atmospheres' CO_2 - content: a process called chemical weathering is responsible for the decomposition of rocks due to acidic rain. Rain dissolves atmospheric CO_2 and becomes weakly acidic when reacting with carbonate to bicarbonate, $H_2CO_3 + CO_3^- \rightarrow 2HCO_3^-$. The decomposition products are transported into the ocean where a conversion to sedimentary rock takes place. After the escape to the Earths' interior, CO_2 is now released back to atmosphere by vulcanic activity.

Oceans are the greatest reservoir for CO_2. They have great impact on the short-term changes in the carbon cycle being of essential relevance for climate of the Earth. The CO_2 exchange solely takes place at the air-water interface. Once dissolved at surface water two processes lead to CO_2 accumulation: the solubility pump and the biological pump. The first mechanism is based on the fact that the solubility of CO_2 increases with decreasing temperature that is why the global ocean circulation transports the CO_2 into the deepwater. The second mechanism describes the biological CO_2 fixation. CO_2, dissolved at the oceans' surface water, is removed by photosynthesis and stored in organic matter. After organic decay most of the organic matter (90 %) is decomposed thereby releasing CO_2 to the atmosphere within weeks. Only a small part is stored in deepwater for hundreds of years. Deepwater ascends to the surface due to thermohaline circulation releasing carbon dioxide back into atmosphere.

During the last decades the possible change of global climate due to human activities has been realised as one of the major problems of our times. The combustion of fossil fuels since the industrial revolution and the tropical deforestation have lead to an increase of carbon dioxide concentration in the atmosphere with a pre-industrial value of 280 ppmv [Barnola et al., 1987] to 379 ppmv [Pachauri and Reisinger, 2007] in 2005. Carbon dioxide is the most important anthropogenic greenhouse gas, representing 77 % of total anthropogenic greenhouse gas emissions in 2004. Between 1970 and 2004, its annual emissions have grown by about 80 %, from 21 to 38 gigatonnes, showing a definite upward trend. The anthropogenic greenhouse gases influence Earths' thermal energy budget more and more and amplify the greenhouse effect. This development will have incalculable consequences for not only the global climate but also ecosystems and human society.

The carbonic acid molecule

Theoretical studies reveal the gas phase equilibrium structure of carbonic acid to be the anti-anti conformer (0 kJ/mol). The structure is shown in Figure 5.17 along with the geometries of its less stable rotational isomers, syn-anti (7.8 kJ/mol) and syn-syn (49.2 kJ/mol). The calculations indicate that intramolecular rearrangements between the conformers proceed mainly by internal rotation. It is more likely that the transition from syn-syn to anti-anti takes place by sequential internal rotation of the two OH-groups rather than by simultaneous rotation taking into account their energy barriers.

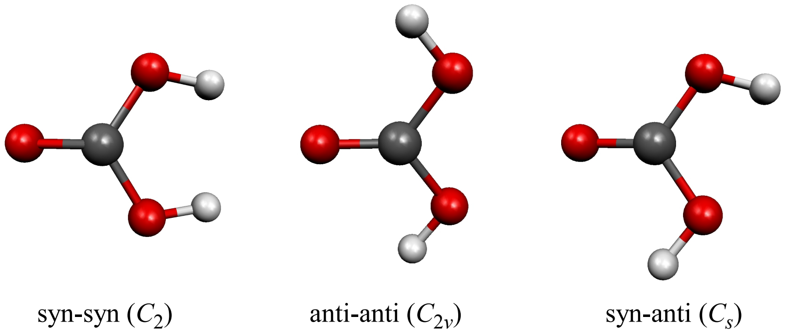

Figure 5.17: Structures of carbonic acid based on parameters taken from [Wight and Boldyrev, 1995].

Intramolecular proton transfer seems to be of small importance because of its high energy barrier of 160.1 kJ/mol [Wight and Boldyrev, 1995]. Carbonic acid is a dicarboxylic acid. It is commonly known that small carboxylic acids tend to form bimolecular aggregates. In gas phase and apolar solvents they form C_2-symmetric dimers with two degenerate intermolecular hydrogen bonds [Pauling and Brockway, 1934; Karle and Brockway, 1944; Derissen, 1971; Fujii et al., 1988]. In crystalline phase only the heavier group members form symmetric cyclic dimers, formic and acetic acid crystals consist of chains [Holtzberg et al., 1953; Jones and Templeton, 1958; Nahringbauer, 1970]. Calculation of gas-phase free energies shows that the dimer consisting of two anti-anti conformers is more stable by about 12 kcal/mol compared to the syn-anti monomer. The stability increases even more going to higher oligomers. In doing so the stability gain flattens out with increasing oligomer size. However in aqueous solution the monomer is favoured because of the hydration free energy being much less negative per H_2CO_3 unit in the oligomers [Tossell, 2006]. The hydration of carbon dioxide to carbonic acid

$$H_2O + CO_2 \rightarrow H_2CO_3 \tag{5.19}$$

has a high potential energy barrier of 217.2 kJ/mol in the gas phase in contrast to the reaction

$$OH^- + CO_2 \rightarrow HCO_3^- \tag{5.20}$$

which has no barrier whatsoever. The product is metastable in respect to dissociation to H_2O and CO_2 by 185 kJ/mol. In fact, theoretical calculations point out that an isolated carbonic acid molecule is kinetically stable at room temperature with a half-life of almost 65.7 million days which corresponds to a decomposition rate of $1.2 \cdot 10^{-13}$ s^{-1}. Only in presence of water the dehydration becomes faster catalysed by water molecules. Thereby the half-life is reduced to only 10 hours by presence of one water molecule and to 2 minutes for two water molecules. It is understood that the dehydration proceeds via a proton relay mechanism [Loerting et al., 2000].

Recent isolation of carbonic acid

Long-held claims of kinetic instability has been disproven by isolation of carbonic acid in the gas and in the solid phase. Schwarz *et al.* formed carbonic acid in the gas phase by thermolysis of NH_4HCO_3 and detected among others a peak at $m/z = 62$ for the radical cation of carbonic acid by means of mass spectrometry [Terlouw et al., 1987]. Hage, Mayer and Hallbrucker synthesised solid carbonic acid successfully by protonation of bicarbonate using a cryogenic technique. Layers of $KHCO_3$ ($KDCO_3$) and HCl (DCl) in glassy methanol or glassy water were deposited on a CsI window at 78 K in a high-vacuum cryostat and heated stepwise to 300 K. With the help of vibrational spectroscopy they were able to monitor the formation of solid carbonic acid at temperatures higher than 150 K [Hage et al., 1993, 1997, 1998]. It was shown that depending on the solvent two different polymorphs, α- and β-H_2CO_3, are formed. They suggest that dimer and larger clusters of H_2CO_3 are the building blocks in the crystal structures of α- and β-H_2CO_3 [Kohl et al., 2009]. The infrared spectrum of β-H_2CO_3 and an assignment of the measured vibrational transitions to the corresponding vibrational modes are given in Figure 5.18 and Table 5.2 [Hage et al., 1997].

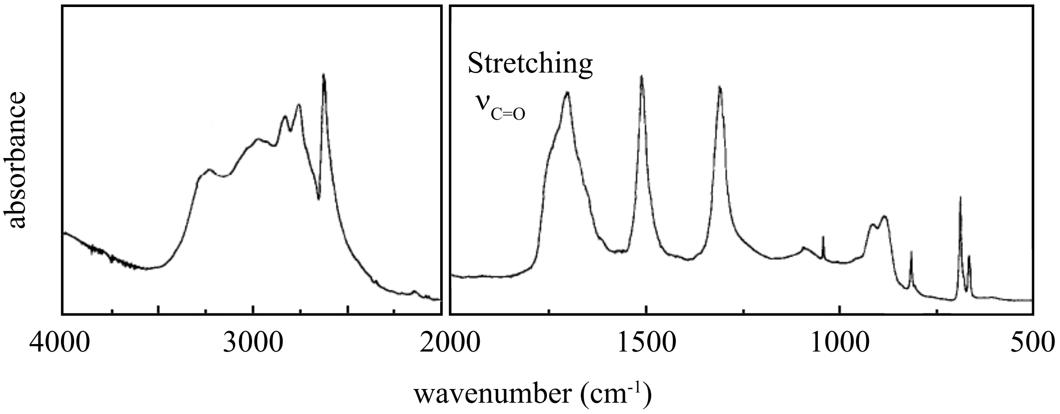

Figure 5.18: The infrared spectrum of β-H_2CO_3 taken from [Hage et al., 1997].

vibrational mode	ν(OH)	ν(C=O)	ν_{as}(C-OH)	δ_{ip}(C-OH)
wavenumber (cm^{-1})	2623	1698	1504, 1302	1504, 1302
vibrational mode	ν_s(C-OH)	δ_{oop}(C-OH)	δ_{oop}(CO_3)	δ_{ip}(CO_3)
wavenumber (cm^{-1})	1038	910, 881	813	686, 664

Table 5.2: Assignment of the vibrational bands shown in Figure 5.18.

It does not come as a big surprise that there is a multitude of crystal structures knowing that two energetically similar conformers exist which tend to form different kind of oligomers [Winkel et al., 2007]. A different way to synthesise carbonic acid was chosen by two other groups. Moore *et al.* and Strazzulla *et al.* irradiated 1:1 $CO_2 + H_2O$ ice mixtures with protons at 20 K. Some of the new features observed in the infrared spectrum were assigned to carbonic acid trapped in the ice matrix. After removal of H_2O, CO_2 and other products like CO, solid H_2CO_3 could be isolated [Moore and

Khanna, 1991; Gerakines et al., 2000; Brucato et al., 1997]. The infrared spectra of carbonic acid obtained by these two different methods do differ in the positions of the bands which can be readily explained by the different hydrogen-bonding interactions in the solid. Controversial is however the assignment of the bands around 1495 cm^{-1} and 1290 cm^{-1}. These could be due to C-OH asymmetric stretching or C-OH in-plane bending vibrations [Moore and Khanna, 1991; Hage et al., 1993]. It should be noted that irradiation of 1:1 $CO_2 + H_2O$ ice mixtures with He^+ ions [Brucato et al., 1997], proton irradition of pure CO_2 ice [Brucato et al., 1997] and UV photolysis of the ice mixtures also give carbonic acid [Gerakines et al., 2000]. Recently, in the course of studying the surface chemistry of calcium carbonate by exposure to acidic gases, adsorbed carbonic acid could be identified on the basis of its vibrational spectrum [Al-Hosney and Grassian, 2004].

5.5 Carbonic Acid in aqueous solution

The previous section has outlined a brief summary on the research on carbonic acid. It has been demonstrated that it is possible to isolate carbonic acid in solid and gas phase. Quantum chemical calculations indicated that H_2CO_3 only becomes unstable when water is present: adding a single water molecule to anhydrous H_2CO_3 makes its decomposition 10^9 times faster thereby reducing the lifetime of this species incredibly [Loerting et al., 2000]. For this reason, direct observation of aqueous carbonic acid has proven to be quite elusive. In this section, recent results are presented that show unequivocally the first direct experimental observation of carbonic acid in aqueous solution [Adamczyk et al., 2009b]. This has been achieved by transient protonation of bicarbonate using the optically triggered photoacid 2N-6,8S and femtosecond infrared spectroscopy. Stationary vibrational spectroscopy has been used successfully to detect solid carbonic acid as can be seen in Figure 5.18. The carbonyl stretching vibration of carbonic acid will be monitored in order to follow its transient generation.

Experimental

Bicarbonate slowly autodehydrates in aqueous solution to yield carbonate, water and carbon dioxide:

$$\begin{aligned} 2\ DCO_3^- + D_2O \rightleftharpoons D_2CO_3 + CO_3^{2-} + D_2O &\rightleftharpoons CO_2(aq) + 2D_2O + CO_3^{2-} \\ CO_2(aq) + 2D_2O + CO_3^{2-} &\rightleftharpoons CO_2(g) + 2D_2O + CO_3^{2-} \end{aligned} \tag{5.21}$$

This equilibrium not only serves to reduce the concentration of DCO_3^- present, initially prepared by dissolving $NaH^{12}CO_3$ (Aldrich) or $NaH^{13}CO_3$ (98 %; Aldrich) in D_2O (Deutero GmbH), but also leads to an increase of *pD* due to CO_2 leakage out of the solution. The fraction of photoacid 2-naphthol-6,8-disulfonic acid, dipotassium salt hydrate (2N-6,8S; ABCR; 50 mM) present in its acid form is obviously highly dependent on the *pD* of the solution as can be seen in Figure 5.6. Consequently, because of the aqueous equilibrium displayed in (5.21), one finds that the initial concentrations of the two reagents decrease in time: the photoacid is converted to its nonreactive photobase form, and DCO_3^- is slowly transformed into carbon dioxide and CO_3^{2-}. This makes it

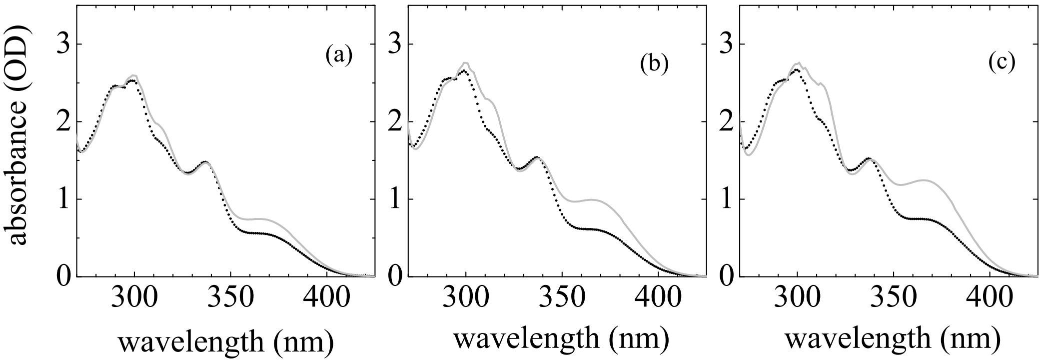

Figure 5.19: Electronic absorption spectra of the 100 μm thick solutions directly after preparation (black dotted curve) and after being used in the femtosecond infrared measurements (grey solid curve) for 0.25 M (a), 0.5 M (b) and 0.8 M (c) $NaDCO_3$, with initial values for the *pD* value of 8.07, 8.13 and 8.20, respectively. The fraction of 2N-6,8S (50 mM) present in its acid form corresponds to 40.2 mM, 39.3 mM and 36.9 mM for (a), (b) and (c), respectively, at the beginning and 36.9 mM, 32.6 mM and 28.1 mM at the end of the measurements.

imperative to ensure that minimal *pD* driven concentration changes occur during the measurement in order to measure reliable kinetics. Bicarbonate concentrations in the range between 0.1 - 0.8 M and sample volumes of 100 ml were used. Apart from the high base concentration it is desirable to have a high fraction of photoacid molecules in the acid form. For this a sufficiently low *pD* must be used. To this effect an optimal $pD = 8$ was found and the solution was buffered with tris(hydroxymethyl)aminomethane[TRIS], DCl (Aldrich) that has a large buffer capacity in this *pD*-region. Buffer concentrations of 0.15 M were used as a compromise between buffer capacity and minimizing the increase in ionic strength. UV-visible spectra of the samples were recorded before and after the measurements (Figure 5.19), and in situ monitoring of the *pD* was implemented in order to verify that the experimental conditions were effective in ensuring a minimal change in *pD* (Figure 5.20 (a)). The change in the ratio between the concentrations of the photoacid and its conjugate base form deduced from the steady-state absorbance in the UV-visible (Figure 5.19), corresponds to the monitored increase in alkanity of 0.1. Confirmation that the apparently negligible increase of the *pD* with time did not impact the measured reaction kinetics was obtained by performing all measurements twice. In the first measurement the pulse delay was scanned in the forward direction (i.e. from -100 ps to 1 ns) where for every pulse delay step signal acquisition occurred for 400 laser shots and averaging over 15s. A backward scan (i.e. from 1 ns to -100 ps) was then recorded with the same solution. Individual measurements were scanned over the whole range only once, no loop averaging was employed. This then allowed a comparison between the measured kinetics of the forward and backward scans. Had the increase in *pD* led to a change in kinetics over time, one would have measured different kinetics for the forward scan compared to the backward scan. As one can see in Figure

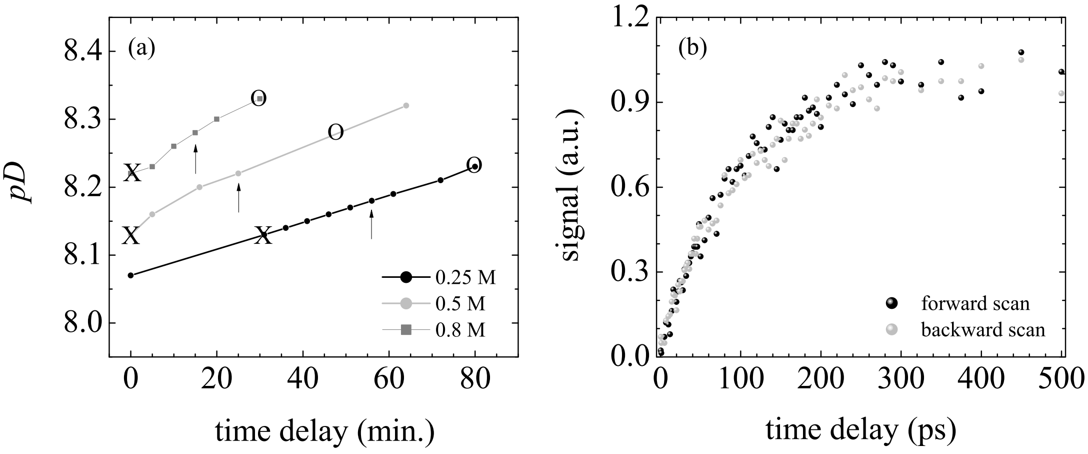

Figure 5.20: Evolution of *pD* during measurement (a): start (cross), end of 1. (arrow) and end of 2. measurement (circle). (b) Kinetics of the C=O stretching marker mode of D_2CO_3 measured at 0.8 M DCO_3^-, showing identical kinetic traces measured by scanning the pulse delay stage from -100 ps to 500 ps (forward scan) and afterwards from 500 ps to -100 ps (backward scan).

5.20 (b) this is not the case. It can be concluded that the rise of 0.1 unit of *pD* that occurs during the time span of the measurement (forward and backward runs), i.e. 60 minutes does not impact the reaction kinetics in a significant way.

Results & Discussion

For low bicarbonate concentration of 0.1 M it is possible to monitor the dynamics of the asymmetric carbonyl stretching vibration of bicarbonate at 1630 cm^{-1} in order to detect the deuteron arrival at the accepting base. Figure 5.21 shows the IR-active C=O stretching vibration of bicarbonate. For comparison the transient bleach signals of 2N-6,8S in photoacid and conjugate photobase configurations are displayed again to highlight the spectral overlap between the bleach signals and the bicarbonate C=O band. Some selected transient spectra measured after excitation of 2N-6,8S in presence of 0.1 M DCO_3^- are plotted below. The bleach signals that appear within time resolution correspond to the photoacid and photobase in the electronic ground state. The increase of the bleach signal at 1630 cm^{-1} at longer times correlates with a rise of a signal at 1720 cm^{-1}. Seeing that the conjugate photobase has a long excited state lifetime the observed dynamics at 1630 cm^{-1} can only be due to a depletion of bicarbonate concentration as a consequence of the final deuteron transfer in the acid-base neutralisation experiment, when bicarbonate converts to carbonic acid. The band at 1720 cm^{-1} can be assigned to the carbonyl stretching vibration of carbonic acid. The frequency position is in full accordance with previously published data as can be seen in Figure 5.18. Further support for the assignment of the transient signal at 1720 cm^{-1} can be given by exploiting the ^{13}C isotope effect. The steady-state infrared spectrum (Figure 5.22 (a)) of isotopically labelled ^{13}C-bicarbonate shows a frequency downshift by about

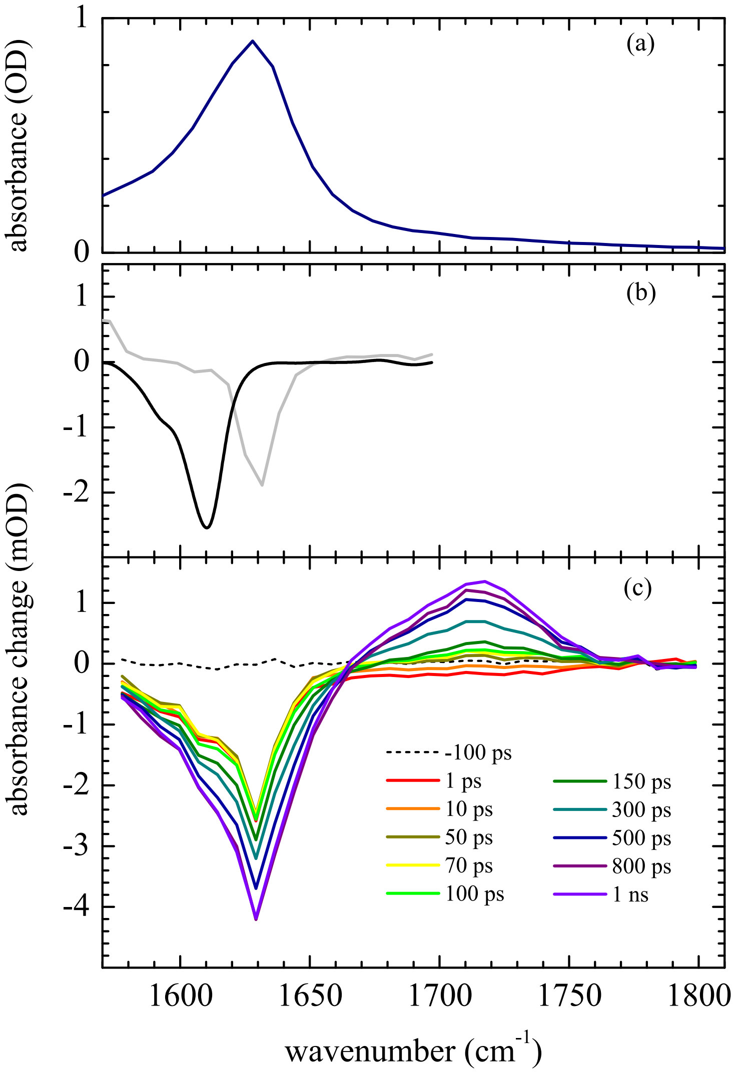

Figure 5.21: (a) Steady-state IR spectrum of DCO_3^-; (b) transient IR spectrum of 2N-6,8S in photoacid (grey line) and photobase (black line) configuration showing the bleach signals corresponding to photoacid or photobase species in the electronic ground state; (c) time-resolved experiment using 0.1 M bicarbonate showing the correlated increase of bleach signal at the DCO_3^- - marker mode frequency and the rise of D_2CO_3 C=O stretching marker band.

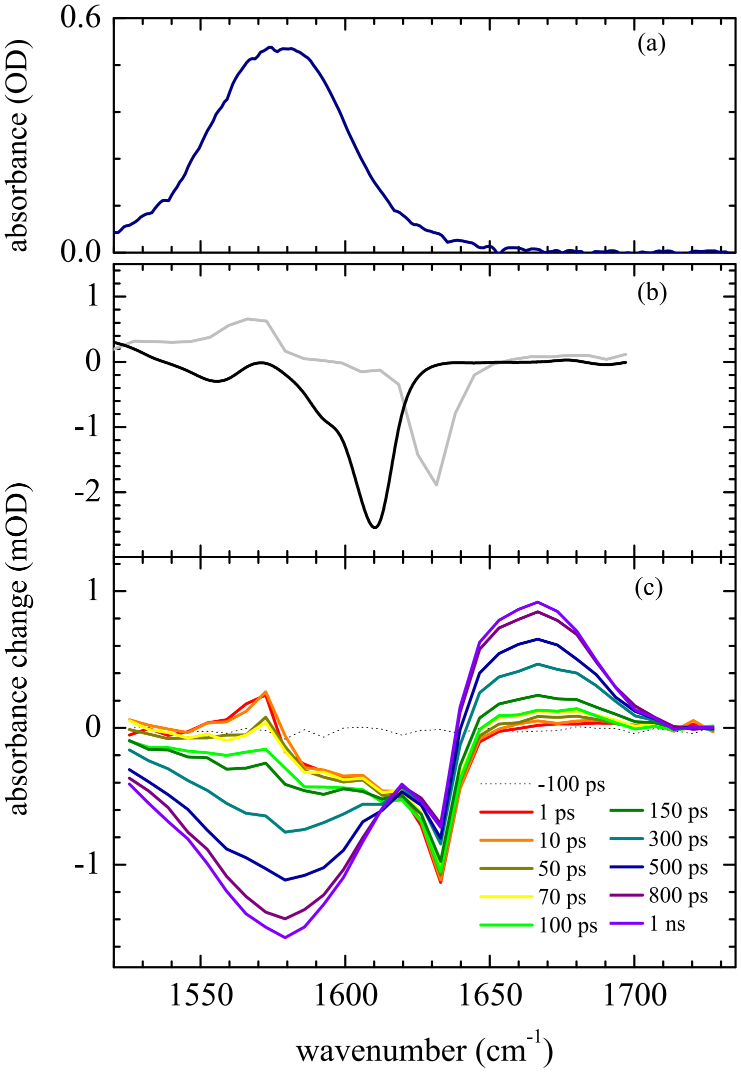

Figure 5.22: (a) Steady-state IR spectrum of $D^{13}CO_3^-$; (b) transient IR spectrum of 2N-6,8S in photoacid (grey line) and photobase (black line) configuration showing the bleach signals corresponding to photoacid or photobase species in the electronic ground state; (c) time-resolved experiment using 0.1 M $D^{13}CO_3^-$ showing the correlated increase of bleach signal at the $D^{13}CO_3^-$ -marker mode frequency and the rise of $D_2\,^{13}CO_3$ $^{13}C{=}O$ stretching marker band.

50 cm^{-1} compared to the ^{12}C-bicarbonate reducing thereby the spectral overlap with the ground state bleach signals of photoacid and conjugate photobase. The transient infrared spectra recorded for 0.1 M $D^{13}CO_3^-$ show directly after photoexcitation of the photoacid three signals: a small signal at 1572 cm^{-1} due to a vibrational mode of the photoacid in its electronic excited state and two ground state bleach signals, one due to the photoacid (1633 cm^{-1}) and the other one due to its conjugate photobase (1613 cm^{-1}). As time evolves a bleach signal grows in at 1578 cm^{-1} with the before mentioned photoacid signal on top. The shape of this bleach signal only evolves because of the vanishing photoacid signal. Both centre frequency and bandwidth correspond to the asymmetric C=O stretching band displayed in the steady-state infrared spectrum of the isotopically labelled bicarbonate. The rise of the signal at 1667 cm^{-1} correlates again with the dynamics on the ^{13}C-bicarbonate signal. Comparison of the centre frequency positions between transient $D_2\ ^{12}CO_3$ and $D_2\ ^{13}CO_3$ reveals the same isotope effect on the carbonyl stretching vibration as for DCO_3^-, a frequency downshift by about 50 cm^{-1}. With this it was proved possible to experimentally observe carbonic acid in aqueous solution.

To shed light on the mechanism of bimolecular deuteron transfer reaction between 2N-6,8S and bicarbonate transient measurements have been carried out as a function of bicarbonate concentration. For this study the time evolution of the three marker modes with centre frequencies at 1410 cm^{-1}, 1472 cm^{-1}, 1510 cm^{-1} corresponding to the photoacid and its conjugate base forms as well as the carbonyl stretching vibrational band of carbonic acid at 1720 cm^{-1} are monitored. To make sure that probing the three marker modes in the spectral range between 1400 and 1550 cm^{-1} reveals information on the first deuteron transfer step and that no additional vibrational modes of D_2CO_3 allocated in this range modulate the observed dynamics the transient spectra with and without base are compared in Figure 5.23 (a) and (b). The upper transient infrared spectra were taken after electronic excitation of solely the photoacid at a *pD* of about 5 without bicarbonate added. At 1ns when deuteron transfer to solvent is completed and all excited molecules exist in the photobase configuration the transient spectrum shows two marker modes, at 1410 and 1510 cm^{-1}, with similar band intensities. At a sample *pD* of about 8.2 both photoacid and conjugate photobase configurations are present and excited. Excitation of a mixture of photoacid and photobase leads to additional vibrational bands in the fingerprint region of the photoacid at 1406 cm^{-1}, 1428 cm^{-1}, 1503 cm^{-1} due to excited state vibrational modes of the photobase and a bleach signal at 1492 cm^{-1} due to a photobase ground state mode (Figure 5.23 (b)). The assignment of these vibrational bands to the photobase configuration has been confirmed measuring the transient infrared spectrum of the photobase after its electronic excitation using a sample of 2N-6,8S at a *pD* of about 12 (Figure 5.23 (c)). Comparing the signal intensities of the excited photobase band at 1406 cm^{-1} with that at 1503 cm^{-1} at early time delays it is possible to conclude that after complete deuteron transfer from the fraction of excited photoacid molecules the signal at 1510 cm^{-1} should be larger in intensity than the signal at 1410 cm^{-1}. It is obvious that the opposite is the case. The reason is that a vibrational mode of D_2CO_3 contributes to the signal at this frequency. Further support for this explanation can be given by a comparison of the kinetic traces at 1410 cm^{-1} with that at 1510 cm^{-1}, and the photoacid signal at 1472 cm^{-1} inverted to aid in the comparison as shown in the panels (d) - (e) of Figure 5.23. The signal at 1510 cm^{-1} follows identical kinetics as the 1472 cm^{-1} photoacid band, and as such

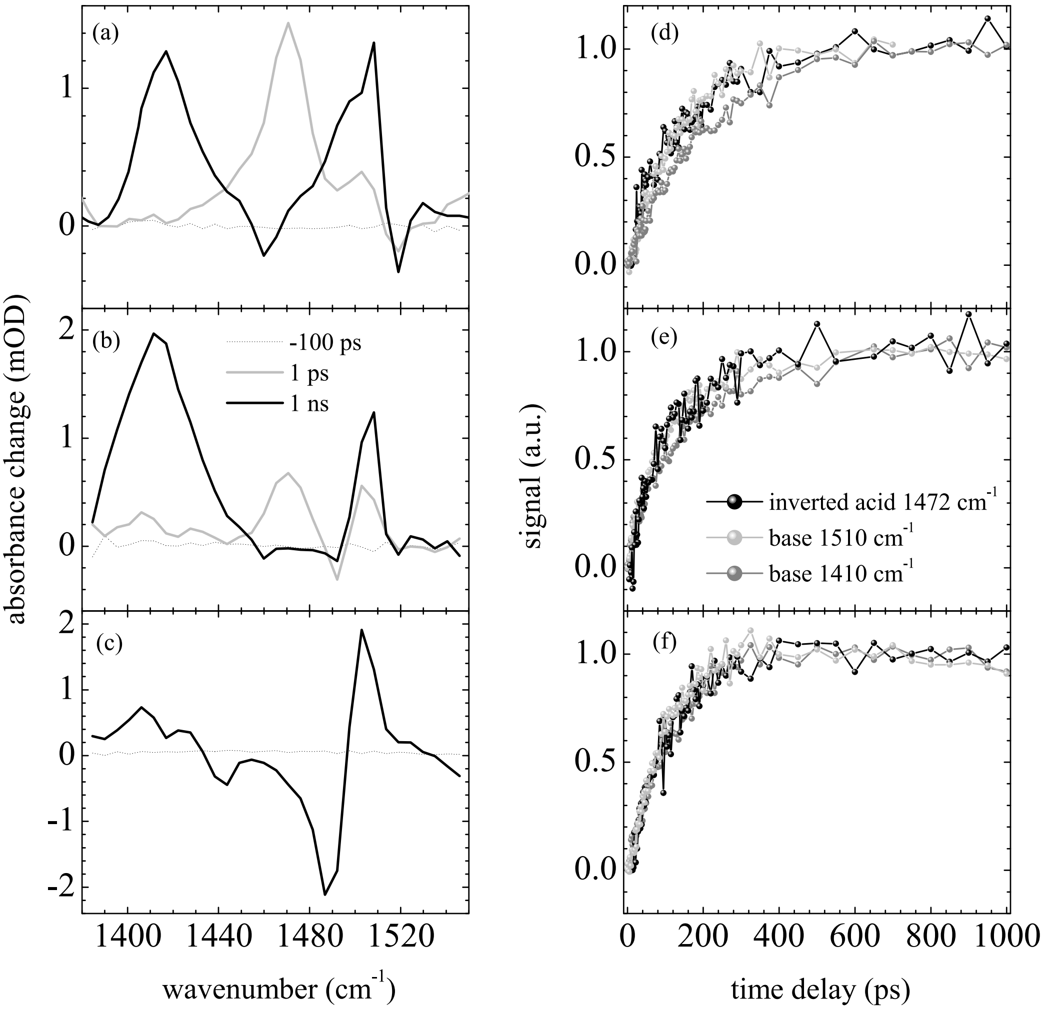

Figure 5.23: The transient IR spectra of 2N-6,8S in D_2O without base (a) showing the marker modes of electronic excited state 2N-6,8S in ROD and RO^- forms, at 1472 (grey line) and 1410 / 1510 cm^{-1} (black line) respectively. The time-resolved experiment using 0.5 M DCO_3^- (b) displays a pronounced difference in the vibrational band pattern due to excitation of the photobase and a fingerprint mode of D_2CO_3 at about 1410 cm^{-1}. Excitation of a sample of 2N-6,8S at *pD* of about 12 reveals the transient spectrum of the photobase (c). The kinetic traces of the three fingerprint modes of photoacid and base for the three bicarbonate concentrations 0.25 M, 0.5 M and 0.8 M are shown in (d) - (e) ordered from low to higher concentration.

these two transitions are genuine marker bands for the first deuteron transfer step. In contrast, the rise of the total signal at 1410 cm^{-1} is obviously slower at low base concentrations, indicative of an additional delayed increase due to D_2CO_3 being generated. Increasing the base concentration the time evolution of the 1410 cm^{-1} signal appears more and more to be the same as the other two genuine marker bands. This hints at a deuteron transfer mechanism consisting of two pathways: deuteron transfer through solvent which leads to a delayed generation of carbonic acid and on-contact deuteron transfer with the second pathway becoming more important the higher the base concentration. Thus the kinetics of the 1472 cm^{-1} photoacid, the 1510 cm^{-1} photobase and the 1720 cm^{-1} D_2CO_3 bands are used as input in the diffusion-assisted reaction model to reveal the deuteron transfer mechanism. The time-dependent decay of the photoacid 1472 cm^{-1} band, the rise of the photobase band at 1510 cm^{-1} and of the carbonyl stretching band of D_2CO_3 at 1720 cm^{-1} for the three concentrations used along with the result of the fitting procedure as solid lines is shown in Figure 5.24 (a) - (c). The values for the fitting parameters are given in Table 5.3. For the best fit of the calculated curves a bimolecular time-independent reaction rate constant of $5.0 \cdot 10^{10}$ $M^{-1}s^{-1}$ for

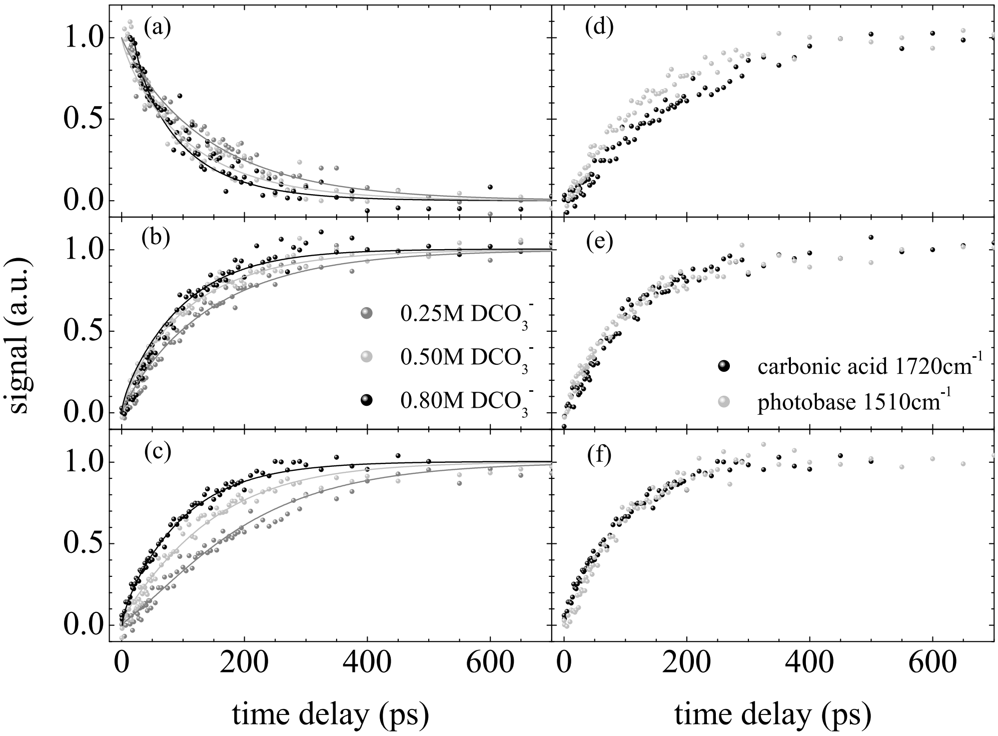

Figure 5.24: Kinetics of the photoacid marker mode at 1472 cm^{-1} (a), the photobase transition at 1510 cm^{-1} (b) and the D_2CO_3 carbonyl stretching vibration at 1720 cm^{-1} (c) for three concentrations of DCO_3^- base: 0.25 M (grey dots), 0.5 M (light grey dots) and 0.8 M (black dots). Solid lines are fits using the diffusion-assisted bimolecular reaction model described in the appendix 5.6. Comparison between the rise of the photobase band (light grey dots) and of the carbonic acid band (black dots) for increasing bicarbonate concentration: 0.25 M (d), 0.5 M (e) and 0.8 M (f).

c (M)	σ_{eff} (Å)	σ'_{eff} (Å)	D $[10^{-9}\mathrm{m}^2\mathrm{s}^{-1}]$	D' $[10^{-9}\mathrm{m}^2\mathrm{s}^{-1}]$	k_w $[10^9\mathrm{s}^{-1}]$	k_a $[10^{10}\mathrm{M}^{-1}\mathrm{s}^{-1}]$
0.25	4.5	7.03	1.8	8	5	7
0.5	4.84	6.84	1.7	7	5	7
0.8	5.10	6.72	1.6	6	4.5	7

Table 5.3: c is the concentration of DCO_3^-. σ_{eff} is the effective contact distance (including the screened Coulomb interaction with $\sigma = 5.5$ Å) and D is the mutual diffusion constant for 2N-6,8S and DCO_3^-. σ'_{eff} is the effective contact distance and D' is the mutual diffusion constants for D^+ and DCO_3^-. k_w is the deuteron dissociation rate of 2N-6,8S in D_2O, and k_a the on-contact bimolecular reaction rate between 2N-6,8S and DCO_3^-.

the deuteron transfer reaction was used, similar to the value of $4.7 \cdot 10^{10}$ $\mathrm{M}^{-1}\mathrm{s}^{-1}$ found for proton transfer from *pH*-change measurements published by Eigen and co-workers [Eigen, 1964; Eigen et al., 1961]. For the on-contact deuteron transfer rate k_a for the intrinsic deuteron transfer reaction between acid and base, a value of $7.0 \cdot 10^{10}$ $\mathrm{M}^{-1}\mathrm{s}^{-1}$ was found. The non-exponential rising behaviour of the marker bands as well as the decay of the photoacid band at 1472 cm^{-1} is a consequence of the time-dependent reaction rate as discussed in chapter 1. Several conclusions can be drawn from the measured dynamics: the absence of the carbonyl stretching band of D_2CO_3 and the photobase band at early times allows to exclude the presence of tight complexes. On the contrary, the rise of the carbonic acid signal is obviously slower than the rise of the photobase signal for low bicarbonate concentrations with a diminishing difference in the observed kinetics when going to higher base concentrations (Figure 5.24 (d) - (f)). In addition, as anticipated the deuteron transfer proceeds faster to bicarbonate with increasing bicarbonate concentration, based on the decreased average diffusion times required for bicarbonate scavenger to encounter a solvated deuteron. These dynamics are governed by the deuteron transfer from photoacid to solvent and subsequent pick up by the base after mutual diffusion to form an encounter complex. However, the fact that concentration-dependent kinetics can be observed on the photoacid and photobase signals reveals a second deuteron transfer pathway. After mutual diffusion of photoacid and base to form the encounter complex the acid-base neutralisation reaction occurs with the on-contact reaction rate. The time-dependent kinetics is based on the decreased average diffusion times required for the formation of the encounter complex between 2N-6,8S and bicarbonate with increasing bicarbonate concentration. The importance of one pathway over the other is determined by their relative time constants for diffusion and for the on-contact reaction. The higher the base concentration is the higher is the importance of the second pathway, namely the on-contact deuteron transfer without the intermediate stage of a solvated deuteron as can be seen in the identical kinetics of carbonic acid and photobase band for high base concentrations (Figure 5.24 (f)). Insight into the structure of the reactive complexes can not be gained. The first pathway leads to a hydrated deuteron in deuterated water that exchanges between different hydration configurations at ultrafast time scales which makes it impossible to monitor vibrational marker bands of the hydrated deuteron at designated frequencies. The encounter complex between photoacid and base likely contains several water solvation shells that stabilise the reaction complex while the deuteron transfer occurs on picosecond time scales. No direct experimental evidence can be given for this suggestion. Only the contact distance of the reactive complex hints at the involvement of several water molecules. Unlike the loose complex which has been observed before by the transient occurence of a hydrated deuteron band at 1850 cm^{-1} spectrally separated from solvent bands the detection of other hydrated deuteron configurations is hampered by the nearby D_2O bending and stretching vibrations. For the present photoacid - base pair no signal in the spectral range between 1800 to 1900 cm^{-1} was detected indicating that loose complexes are of minor importance.

It is worth mentioning that no signals located in the range for the asymmetric stretching marker mode of CO_2 around 2364 cm^{-1} were detected, indicating that significant dehydration of D_2CO_3 into CO_2 does not occur on subnanosecond time scales. Instead, D_2CO_3 appears to be a kinetically stable compound with a lifetime extending way beyond 1 ns.

5.6 Free energy correlation

Section 1.4 introduced the semi-empiric correlation between the proton transfer rate and the free energy of reaction. The general correlation between differences in acid strengths and reaction rates is found for a large class of aqueous photoacid dissociation and photoacid-base neutralisation [Pines and Pines, 2002, 2007; Pines et al., 1997; Pines and Fleming, 1991]. The bimolecular on-contact reaction rate constant k_a used in the Szabo-Collins-Kimball description for diffusion-assisted bimolecular reaction dynamics has been converted into the first-order rate constant k_r for proton transfer within the encounter complex using the relation [Rini et al., 2004]:

$$k_r = \frac{4}{3}\pi \cdot \sigma^3 \cdot N_A \cdot k_a. \tag{5.22}$$

For $\sigma = 6.2$ Å it follows that $k_r = 1.67$ M $\cdot\, k_a = 1.2 \cdot 10^{11}$ s^{-1} for the reaction between 2N-6,8S and DCO_3^- in D_2O. After correction for the H/D isotope effect, k_r is found to amount to $1.7 \cdot 10^{11}$ s^{-1} for the reaction between 2N-6,8S and HCO_3^- in H_2O. In aqueous acid-base neutralisation reactions the isotope effect has been found to have a value of $k_{H^+}/k_{D^+} = (m_{D^+}/m_{H^+})^{1/2} = 1.45$, with m_{H^+} (m_{D^+}) the mass of the proton (deuteron) [Mohammed et al., 2007b]. k^* and $\lambda/4$ have been fitted to the experimental results, obtained on proton transfer between HPTS and the carboxylate bases $CH_{3-x}Cl_xCOO^-$ (x = 0 to 3) and $HCOO^-$ [Rini et al., 2004; Mohammed et al., 2007b], resulting in $k^* = (1\text{ ps})^{-1}$ and $\lambda/4 = 2.5$ kcal mol^{-1} for the activation energy when $\Delta pK_a = 0$. These values are close to those found for photoacid dissociation to water [Pines and Pines, 2002, 2007]. Figure 5.25 shows the overall proton transfer rate in the encounter complex, k_r, as a function of the difference between the pK_a^* of the excited photoacid and the pK_a of the conjugate acid of the base for different photoacid - base pairs. The triangles in Figure 5.25 indicate the result for HPTS ($pK_a(S_1) = 1.1$) reacting with acetate, monochloroacetate, dichloroacetate and trichloroacetate (with pK_a = 4.7, 2.85, 1.35 and 0.7, respectively). The black square is the result obtained for the reaction of HPTS with formate ($pK_a = 3.7$). The grey square depicts the result of the reaction between 2N-6,8S ($pK_a(S_1) = 0.3$) and bicarbonate ($pK_a = 3.45 \pm 0.15$). All pK_a-values correspond to the proton transfer reaction in H_2O. The deuteron transfer reaction typically has pK_a-values that are 0.4 to 0.5 units higher [Pines, 2006]. One finds that the correlation holds for a carbonic acid pK_a of 3.45 ± 0.15, as opposed to the first apparent pK_a of 6.35 for $CO_2(aq)/H_2O$. This result follows naturally from the real time observation of proton transfer to bicarbonate on the picosecond time scale, without interfering effects from slower reversible deprotonation or dehydration reactions of carbonic acid. Furthermore, the experimental results demonstrate that D_2CO_3 is kinetically stable in aqueous solution compared to its formation rate. The dehydration rate of D_2CO_3 is relatively slow. Taking into account the combined effects of mutual diffusion and the proton transfer within the encounter complex [Pines et al., 1997], the deprotonation reaction rate constant of D_2CO_3 at room temperature may be estimated from the measured overall deuteration rate of DCO_3^- and the equilibrium constant of

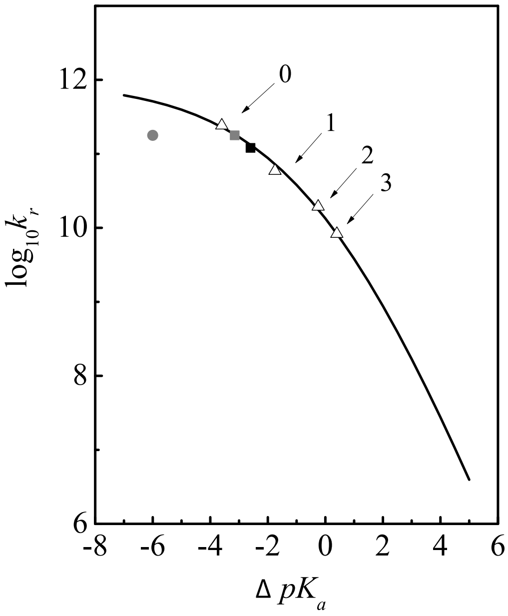

Figure 5.25: The free energy correlation connecting ΔpK_a (photoacid-base) to the overall proton transfer in the encounter complex k_r: the free-energy vs. reaction-rate curves are calculated using (1.69) (solid line). Triangles: proton transfer between HPTS and different carboxylate bases $CH_{3-x}Cl_xCOO^-$ (x = 0 to 3); black square: proton transfer between HPTS and formate; grey square/grey dot: proton transfer between HPTS and bicarbonate.

D_2CO_3:

$$k_{off} = K_{eq} \cdot k_{on} = 10^{-pK_a}\mathrm{M} \cdot \frac{k_d k_r}{k_{-d} + k_r}\mathrm{M}^{-1}\mathrm{s}^{-1}$$

$$= 10^{-4}\mathrm{M} \cdot 3.3 \cdot 10^{10}\mathrm{M}^{-1}\mathrm{s}^{-1} = 3.3 \cdot 10^{6}\mathrm{s}^{-1}. \tag{5.23}$$

k_d and k_{-d} are the forward and backward diffusion-controlled rates, k_r and k_{br} are the forward and backward on contact reaction rates and k_{off} denotes the deprotonation reaction rate constant. Please note that the measured overall deuteration rate of DCO_3^- is scaled to zero ionic strength. The relation $pK_a(D_2CO_3) \approx pK_a(H_2CO_3) + 0.5$ has been used [Bell, 1973]. This rate constant corresponds to a lifetime of about 300 ns for D_2CO_3 before deuteron dissociation ensues. From a kinetic point of view the main cause of instability of D_2CO_3 over short times under aqueous conditions is therefore acid dissociation (deprotonation), rather than decomposition into CO_2 and H_2O, which takes place with an effective rate constant of $1.8 \cdot 10^1$ s^{-1} [Pocker and Bjorkquist, 1977]. This conclusion also holds for H_2CO_3. Carbonic acid acts like an ordinary carboxylic acid on nanosecond time scales with an acidity comparable to that of formic acid. This considerable acidity of carbonic acid should henceforth be considered in the context of CO_2-rich aqueous environments. The proton transfer reaction between bicarbonate and the photoacid proceeds along two reaction paths: on the one hand, the photoacid dissociates and the proton is transferred to solvent, H_2O (protolysis pathway). After

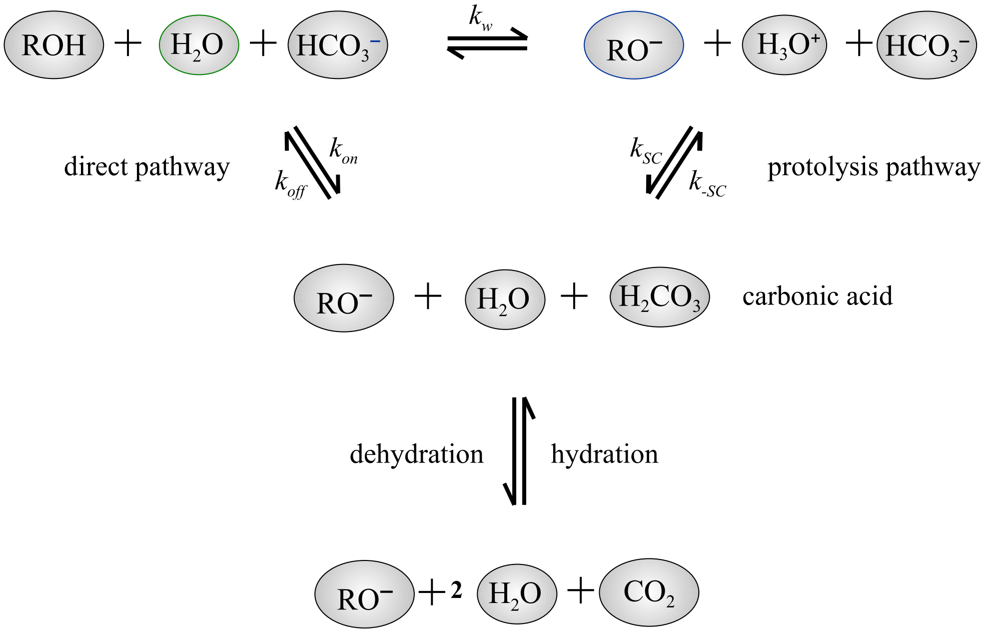

Figure 5.26: Reaction pathways between the photoacid and bicarbonate adapted from Eigen's scheme for acid-base neutralisation [Eigen, 1964]. The hydrolysis and the hydroxide addition pathways are omitted here for greater clarity as these do not play a significant role under the experimental conditions.

mutual diffusion hydrated proton and base encounter and proton transfer occurs. On the other hand, photoacid and base can directly form an encounter complex in order to transfer the proton (direct pathway). The importance of one proton transfer pathway to another depends on the relative time constants for diffusion and intrinsic reaction within an encounter complex (Figure 5.26).

Relation between the anisotropy and the angle between transition dipoles

In order to derive a general expression for a fixed angle α between the electronic $\vec{\mu}_{el}$ and vibrational $\vec{\mu}_{vib}$ transition dipole moments two coordinate systems are defined: $[\mathbf{n}_i]$, the lab coordinate system, defines the pump light to be polarised parallel to the $\mathbf{n}_3$-axis and the probe light is detected along the $\mathbf{n}_1$-axis, using polarisations in two directions, parallel to the $\mathbf{n}_3$-axis and parallel to the $\mathbf{n}_2$-axis whereas the orientation of the transition dipole moments is defined in a molecule-internal coordinate system, $[\mathbf{e}_i]$. The electronic transition dipole moment $\vec{\mu}_{el}$ is parallel to $\mathbf{e}_3$:

$$\vec{\mu}_{el} = \mu_{el}\mathbf{e}_3 \tag{24}$$

and the vibrational transition dipole moment $\vec{\mu}_{vib}$ lies in the plane spanned by $\mathbf{e}_1$ and $\mathbf{e}_3$ according to:

$$\vec{\mu}_{vib} = \mu_{vib}\sin\alpha\mathbf{e}_1 + \mu_{vib}\cos\alpha\mathbf{e}_3. \tag{25}$$

Figure 27 illustrates the two coordinate systems: $[\mathbf{n}_i]$ and $[\mathbf{e}_i]$, indicated as grey and black circles, is spanned by $\mathbf{n}_1$ and $\mathbf{n}_2$ and by $\mathbf{e}_1$ and $\mathbf{e}_2$, respectively. θ denotes the angle between the direction of the polarisation of the pump light and the excitation dipole $\vec{\mu}_{el}$. ψ indicates the rotation of the molecule around $\vec{\mu}_{el}$ or in other words the orientation of the plane spanned by $\vec{\mu}_{el}$ and $\vec{\mu}_{vib}$ in respect to $\vec{\mu}_{el}$. And ϕ parametrises

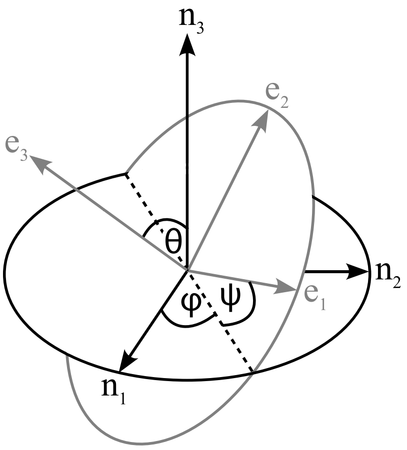

Figure 27: Transformation of two rectangular and right-handed coordinate systems using Euler‘s method.

the rotation of $\vec{\mu}_{el}$ around the $\mathbf{n}_3$-axis.
First, the molecule-internal coordinate system has to be transformed into the lab coordinate system. This can be done by three rotations:

1. $[\mathbf{n}_i]$ is rotated around the $\mathbf{n}_3$-axis by an angle ϕ so that the new vector $\mathbf{n}'_1$ corresponds with the intersection line of the two circles.

2. $[\mathbf{n}'_i]$ is rotated around the new axis $\mathbf{n}'_1$ by an angle θ so that the new axis of the laboratory coordinate system $\mathbf{n}''_3$ equals the $\mathbf{e}_2$-axis of the molecule-internal coordinate system. This rotation tilts the $\mathbf{n}_1$-$\mathbf{n}_2$-plane into the $\mathbf{e}_1$-$\mathbf{e}_2$-plane.

3. $[\mathbf{n}''_i]$ is rotated around the new axis $\mathbf{n}''_3$ by an angle ψ so that the two coordinate systems are identical, $[\mathbf{n}'''_i] = [\mathbf{e}_i]$.

The transformation matrix for the three rotations is given by the matrix multiplication of the three individual transformation matrices:

$$D(\psi,\theta,\phi) = \begin{pmatrix} \cos\psi & \sin\psi & 0 \\ -\sin\psi & \cos\psi & 0 \\ 0 & 0 & 1 \end{pmatrix} \begin{pmatrix} 1 & 0 & 0 \\ 0 & \cos\theta & \sin\theta \\ 0 & -\sin\theta & \cos\theta \end{pmatrix} \begin{pmatrix} \cos\phi & \sin\phi & 0 \\ -\sin\phi & \cos\phi & 0 \\ 0 & 0 & 1 \end{pmatrix} \tag{26}$$

$$= \begin{pmatrix} \cos\psi\cos\phi - \sin\psi\cos\theta\sin\phi & \cos\psi\sin\phi + \sin\psi\cos\theta\cos\phi & \sin\psi\sin\theta \\ -\sin\psi\cos\phi - \cos\psi\cos\theta\sin\phi & -\sin\psi\sin\phi + \cos\psi\cos\theta\cos\phi & \cos\psi\sin\theta \\ \sin\theta\sin\phi & -\sin\theta\cos\phi & \cos\theta \end{pmatrix}. \tag{27}$$

$[\mathbf{e}_i]$ can be expressed by $[\mathbf{n}_i]$ as:

$$\mathbf{e}_i = \sum_{j=1}^{3} d_{ij}\mathbf{n}_j, \tag{28}$$

using the elements d_{ij} of the transformation matrix $D(\psi,\theta,\phi)$. The electronic and the vibrational dipole transition moments are then given by:

$$\vec{\mu}_{el} = \mu_{el} \sum_{j=1}^{3} d_{3j}(\psi,\theta,\phi)\mathbf{n}_j \tag{29}$$

and

$$\vec{\mu}_{vib} = \mu_{vib} \sum_{j=1}^{3} \left[d_{1j}(\psi,\theta,\phi)\sin\alpha + d_{3j}(\psi,\theta,\phi)\cos\alpha\right]\mathbf{n}_j. \tag{30}$$

The overall probability of detecting a photon in one of the two directions when exciting a molecule oriented in space according to ψ, θ and ϕ is proportional to the product of the probability of exciting the molecule P_{ex} and the probability of detecting a photon P_{det} emitted by an excited molecule. The probabilities of detecting a photon with the corresponding polarisation are:

$$
\begin{aligned}
P_{det}(\mathbf{n}_3) \propto I(\mathbf{n}_3) &= E_0^2 \left[d_{13}(\psi,\theta,\phi)\sin\alpha + d_{33}(\psi,\theta,\phi)\cos\alpha\right]^2 \\
&= E_0^2 \left[\sin\psi\sin\theta\sin\alpha + \cos\theta\cos\alpha\right]^2,
\end{aligned} \tag{31}
$$

$$
\begin{aligned}
P_{det}(\mathbf{n}_2) \propto I(\mathbf{n}_2) &= E_0^2 \left[d_{12}(\psi,\theta,\phi)\sin\alpha + d_{32}(\psi,\theta,\phi)\cos\alpha\right]^2 \\
&= E_0^2 \left[(\cos\psi\sin\phi + \sin\psi\cos\theta\cos\phi)\sin\alpha - \sin\theta\cos\phi\cos\alpha\right]^2,
\end{aligned} \tag{32}
$$

being the projections of the “intensity-vector” onto the $\mathbf{n}_2$- and $\mathbf{n}_3$-axis, respectively. Similarly, the probability of exciting a molecule is given by:

$$
P_{ex} \propto E_0^2 d_{33}(\psi,\theta,\phi) = E_0^2 \cos^2\theta. \tag{33}
$$

In order to determine the overall detection probability not only for a single molecule but for the sample it has be integrated over all molecules. The number of molecules dn is proportional to:

$$
dn = \sin\theta d\phi d\theta d\psi. \tag{34}
$$

Finally, for detection along the $\mathbf{n}_3$-axis the probability is given by:

$$
\begin{aligned}
P(\mathbf{n}_3) \propto \int_0^{2\pi}\int_0^{\pi/2}\int_0^{2\pi} &\cos^2\theta\sin\theta(\sin\psi\sin\theta\sin\alpha \\
&+ \cos\theta\cos\alpha)^2 d\phi d\theta d\psi.
\end{aligned} \tag{35}
$$

The integration over ϕ from 0 to 2π yields a constant factor 2π. By integrating over ψ from 0 to 2π the cross term of the bracket will vanish:

$$
P(\mathbf{n}_3) = 2\pi^2 \int_0^{\pi/2} \left(\cos^2\theta\sin^3\theta\sin^2\alpha + 2\cos^4\theta\sin\theta\cos^2\alpha\right) d\theta. \tag{36}
$$

Note that:

$$
\int \sin x dx = -\cos x \qquad \text{and} \qquad \int \sin^2 x dx = \frac{1}{2}\left(x - \sin x\cos x\right). \tag{37}
$$

Using $\sin^2\theta = 1 - \cos^2\theta$ the probability becomes:

$$P(\mathbf{n}_3) = 2\pi^2 \int_0^{\pi/2} \sin\theta \left[\cos^4\theta\left(2\cos^2\alpha - \sin^2\alpha\right) + \cos^2\theta\sin^2\alpha\right] d\theta \tag{38}$$

$$= -2\pi\left[\frac{1}{5}\left(2\cos^2\alpha - \sin^2\alpha\right)\cos^5\theta + \frac{1}{3}\sin^2\alpha\cos^3\theta\right]_0^{\pi/2} \tag{39}$$

$$= \frac{4}{5}\pi^2\cos^2\alpha + \frac{4}{15}\pi^2\sin^2\alpha \tag{40}$$

$$= \frac{4}{15}\pi^2\left(2\cos^2\alpha + 1\right), \tag{41}$$

where following integral had to be used:

$$\int \cos^n x \sin x dx = -\frac{1}{n+1}\cos^{(n+1)} x. \tag{42}$$

For the detection along the $\mathbf{n}_2$-axis the probability is given by:

$$P(n_2) \propto \int_0^{2\pi}\int_0^{\pi/2}\int_0^{2\pi} \cos^2\theta\sin\theta[(\cos\psi\sin\phi + \sin\psi\cos\theta\cos\phi)\sin\alpha$$

$$- \sin\theta\cos\phi\cos\alpha]^2 d\phi d\theta d\psi. \tag{43}$$

The integration over ψ is again easily performed as ψ occurs only in the first term of the square bracket. Therefore the cross term vanishes when integrating from 0 to 2π:

$$P(n_2) = \pi \int_0^{\pi/2}\int_0^{2\pi} \cos^2\theta\sin\theta[(\sin^2\phi\sin^2\alpha + \cos^2\theta\cos^2\phi\sin^2\alpha$$

$$+2\sin^2\theta\cos^2\phi\cos^2\alpha) d\theta d\phi. \tag{44}$$

$$P(n_2) = \pi^2 \int_0^{\pi/2} \cos^2\theta\sin\theta[(\sin^2\alpha + \cos^2\theta\cos^2\phi\sin^2\alpha$$

$$+2\sin^2\theta\cos^2\alpha) d\theta \tag{45}$$

$$P(n_2) = \frac{4}{15}\pi^2\left(\sin^2\alpha + 1\right). \tag{46}$$

The final expression for the anisotropy is therefore:

$$r(\alpha) = \frac{P(\mathbf{n}_3) - P(\mathbf{n}_2)}{P(\mathbf{n}_3) + 2P(\mathbf{n}_2)} = \frac{2\cos^2\alpha + 1 - \sin^2\alpha - 1}{2\cos^2\alpha + 1 + 2\sin^2\alpha + 2} = \frac{3\cos^2\alpha - 1}{5}. \tag{47}$$

Modelling aqueous bimolecular proton transfer

In the first chapter the different pathways of aqueous bimolecular proton transfer has been briefly summarized. The proton transfer dynamics between a photoacid and a base in aqueous solution is obviously a theoretically challenging problem, where besides the proton dissociation from the photoacid, and the proton association with the base, also proton transfer through water molecules and mutual diffusion between the photoacid and the base may play a key role. In the case that proton dissociation to water without a base around does not occur on the relevant time scales, proton transfer may then only occur to the base when the photoacid and the base react while constituting a contact complex formed after mutual diffusion. In this case the description can be based on molecular diffusion obeying the DSE which is described in more detail in chapter 1. On the other hand, when proton transfer from the photoacid to the base proceeds via several relevant pathways, including free diffusion through water, and proton shuttling via water bridges of different lengths, one should rather use a set of coupled rate equations to describe the reaction dynamics. For this approach which offers a profound insight into the proton transfer dynamics it is necessary to have detailed kinetics of the different transient species available. Unfortunately, this is not the case but in order to have a first understanding of the reaction dynamics between the photoacid 2N-6,8S and different bases following fitting routine has been used.
The survival probability, $S_{ROH}(t)$, of an excited proton donor, ROH*, surrounded by an equilibrium distribution of proton acceptor molecules with the initial condition S(0)=1, may be approximated according to the following kinetic equation:

$$\frac{dS_{ROH}(t)}{dt} = -ck_r(t)S_{ROH}(t) - k_w S_{ROH}(t), \tag{48}$$

where c is the bulk concentration of the proton acceptor, k_w is the first order dissociation constant of the proton donor to the solvent and $k_r(t)$ is the time-dependent rate coefficient of the proton donor to the base within the encounter complex that can be derived from the Debye-von Smoluchowski Szabo-Collins-Kimball description (1.46, 1.47). Integrating, the survival probability of the acid is given by:

$$S_{ROH}(t) = exp\left(-k_w t - \int_0^t ck_r(t')dt'\right). \tag{49}$$

The proton donor is a doubly negatively charged molecule and the base has a negative charge as well. The overall solution is electrically neutral as it contains the counterions, Na$^+$, of photoacid and base, respectively. The potential between the photoacid and the base is described by the Debye-Hückel ionic screening law (1.39, 1.44). In order to describe the kinetics of the base it is assumed that any excited photoacid will ultimately transfer its proton either to the solvent (water) or to the base, where any proton released to the solvent eventually will be picked up by the base (proton scavenging by the base). The survival probability of the released proton following acid dissociation to the solvent is given by:

$$\frac{dS_{H+}}{dt} = k_w S_{ROH}(t) - k_{dl} c S_{H+}. \tag{50}$$

At high concentration of base the largest fraction of photoacid transfers its proton directly to the base. Here direct means any form of encounter complex consisting of ROH$\cdot\cdot\cdot$(H$_2$O)$_n$ $\cdot\cdot\cdot$B$^-$ (n = 0,1,2,...). The small fraction of proton transfer via the indirect route of acid dissociation to the solvent and then proton pick-up by the base in a diffusion limited reaction may be approximated by the diffusion limited rate constant of the reaction, k_{dl}:

$$k_{dl} = 4\pi D' \sigma'_e N, \tag{51}$$

where σ'_e is given by 1.47 and D' is the relative diffusion coefficient between the base and the solvated proton. Finally, the survival probability of the protonated base is given by:

$$\frac{dS_{HB}}{dt} = c k_r(t) S_{ROH}(t) + c k_{dl} S_{H+}. \tag{52}$$

The differential equations for the survival probabilities S_{H+} and S_{HB} (50, 52) may be solved analytically:

$$S_{H+} = exp\left(-c k_{dl} t\right) \int_0^t S_{ROH}(t') k_w exp\left(c k_{dl} t'\right) dt', \tag{53}$$

$$S_{HB} = \int_0^t \left(c k_r(t') S_{ROH}(t') + c k_{dl} S_{H+}\right) dt'. \tag{54}$$

Using the expression for survival probability of S$_{ROH}(t)$, 49, it is possible to integrate 53 and 54 numerically to find the population kinetics for the conjugate acid HB.

The diffusion coefficient of DCO$_3^-$ was calculated from its known value for mobility, obtained by conductivity measurements of the ions in H$_2$O [Dean, 1999; Vanysek, 2002], corrected for changes in viscosity, and was varied for best fit in the range of ± 10 %. The contact radius parameter, σ, was searched in the range of 5 - 6.5 Å, covering the accepted range for this parameter in typical acid-base reactions [Kosower and Huppert, 1986; Pines et al., 1988; Agmon et al., 1988; Rini et al., 2003, 2004; Mohammed et al., 2005b, 2007b]. For the contact separation distance between 2N-6,8S and D$_3$O$^+$ we used a value of σ = 6.2 Å[Solntsev et al., 2001]. The effective radius σ_{eff} includes the interaction potential between acid and base, and depends on ionic strength of the solution [Szabo, 1989].

Bibliography

K. Adamczyk, J. Dreyer, D. Pines, E. Pines, and E. T. J. Nibbering. Ultrafast protonation of cyanate anion in aqueous solution. *Isr. J. Chem.*, 49:217, 2009a.

K. Adamczyk, M. Prémont-Schwarz, D. Pines, E. Pines, and E. T. J. Nibbering. Real-time observation of carbonic acid formation in aqueous solution. *Science*, 326:1690, 2009b.

N. Agmon, E. Pines, and D. Huppert. Geminate recombination in excited-state proton transfer reactions. II. Comparison of diffusional and kinetic schemes. *J. Chem. Phys.*, 88(9):5631, 1988.

H. A. Al-Hosney and V. H. Grassian. Carbonic acid: An important intermediate in the surface chemistry of calcium carbonate. *J. Am. Chem. Soc.*, 126:8068, 2004.

P. Albers, E. Stark, and G. Huber. Continuous-wave laser operation and quantum efficiency of titanium-doped sapphire. *J. Opt. Soc. Am. B*, 3:134, 1986.

A. N. Alexandrova and W. L. Jorgensen. Why urea eliminates ammonia rather than hydrolyzes in aqueous solution. *J. Phys. Chem. B*, 111(4):720, 2007.

A. R. Amell. Kinetics of the hydrolysis of cyanic acid. *J. Am. Chem. Soc.*, 78(24):6234, 1956.

K. Ando and J. T. Hynes. Acid-base proton transfer and ion pair formation in solution. *Adv. Chem. Phys.*, 110:381, 1999.

J. A. Armstrong. Measurement of picosecond laser pulse width. *Appl. Phys. Lett.*, 10: 16, 1967.

T. Asahi and N. Mataga. Charge recombination process of ion pair state produced by excitation of charge-transfer complex in acetonitrile solution. Essentially different character of its energy gap dependence from that of geminate ion pair formed by encounter between fluorescer and quencher. *J. Phys. Chem.*, 93(18):6575, 1989.

T. Asahi and N. Mataga. Femtosecond-picosecond laser photolysis studies on the dynamics of excited charge-transfer complexes: Aromatic hydrocarbon-acid anhydride, -tetracyanoethylene, and -tetracyanoquinodimethane systems in acetonitrile solutions. *J. Phys. Chem.*, 95:1956, 1991.

P. W. Atkins. *Physical Chemistry.* Oxford University Press, Oxford Melbourne Tokyo, 1990.

J. M. Barnola, D. Raynaud, Y. S. Korotkevic, and C. Lorius. Vostock ice core provides 160,000-year record of atmospheric CO_2. *Nature*, 329:408, 1987.

A. D. Becke. Density-functional thermochemistry. III. The exact role of exchange. *J. Chem. Phys.*, 98:5648, 1993.

J. V. Beitz and J. R. Miller. Exothermic rate restrictions on electron transfer in a rigid medium. *J. Chem. Phys.*, 71(11):4579, 1979.

R. P. Bell. *The proton in chemistry.* Chapman and Hall, London, 2 edition, 1973.

R. P. Bell. *The tunnel effect in chemistry.* Chapman and Hall, London, 1980.

D. J. Belson and A. N. Strachan. Preparation and properties of isocyanic acid. *Chem. Soc. Rev.*, 11:41, 1982.

M. N. Berberan-Santos and J. M. G. Martinho. Diffusion-influenced excimer formation kinetics. *J. Chem. Phys.*, 95(3):1817, 1991.

N. Bloembergen. *Nonlinear Optics.* World Scientific, 1996.

V. E. Bondybey, J. H. English, C. W. Mathews, and R. J. Contolini. Infrared spectra and isomerization of CHNO species in rare gas matrices. *J. Mol. Spectrosc.*, 92:431, 1982.

J. H. Boughton and R. N. Keller. Dissociation constants of hydropseudohalic acids. *J. Inorg. Nucl.Chem.*, 28:2851, 1966.

R. W. Boyd. *Nonlinear Optics.* Academic Press, London, U.K., 1993.

S. Bratos, J.-C. Leicknam, G. Gallot, and H. Ratajczak. *Infra-red spectra of hydrogen bonded systems: Theory and experiment*, volume 23 of *Understanding chemical reactivity*, pages 5–30. Kluwer Academic Publishers, Dordrecht, The Netherlands, 2002.

M. H. Brooker and N. Wen. Raman studies of cyanate: Fermi resonance, hydration and hydrolysis to urea. *Can. J. Chem.*, 71:1764, 1993.

J. R. Brucato, M. E. Palumbo, and G. Strazzulla. Carbonic acid by ion implantation in water/carbon dioxide ice mixtures. *Icarus*, 125:135, 1997.

B. S. Brunschwig, S. Ehrenson, and N. Sutin. Distance dependence of electron-transfer reactions: Rate maxima and rapid rates at large reactant separations. *J. Am. Chem. Soc. 1984*, 106:6858, 1984.

A. D. Buckingham, N. C. Handy, J. E. Rice, K. Somasundram, and C. Dijkgraaf. Reactions involving CO_2, H_2O, and NH_3: The formation of (i) carbamic acid, (ii) urea, and (iii) carbonic acid. *J. Comput. Chem.*, 7:283, 1986.

A. I. Burshtein. Unified theory of photochemical charge separation. *Adv. Chem. Phys.*, 114:419, 2000.

J. A. Ciezak, J. B. Leão, and B. S. Hudson. Vibrational analysis of the inelastic neutron scattering spectra of electron donor-acceptor complexes. II. Tetracyanoethylene-perylene by electronic structure calculations. *J.Mol. Struct. THEOCHEM*, 767:23, 2006.

A. O. Cohen and R. A. Marcus. On the slope of free energy plots in chemical kinetics. *J. Phys. Chem.*, 72(12):4249, 1968.

B. Cohen, D. Huppert, and N. Agmon. Non-exponential Smoluchowski dynamics in fast acid-base reaction. *J. Am. Chem. Soc.*, 122(40):9838, 2000.

B. Cohen, D. Huppert, and N. Agmon. Diffusion-limited acid-base nonexponential dynamics. *J. Phys. Chem. A*, 105(30):7165, 2001.

F. C. Collins and G. E. Kimball. Diffusion-controlled reaction rates. *J. Colloid Sci.*, 4: 425, 1949.

M. J. Cox and H. J. Bakker. Parallel proton transfer pathways in aqueous acid-base reactions. *J. Chem. Phys.*, 128:174501, 2008.

J. A. Dean. *Lange's handbook of chemistry.* McGraw-Hill, New York, 1999.

P. Debye. Reaction rates in ionic solutions. *J. Electrochem. Soc.*, 82:265, 1942.

P. Debye and E. Hückel. Zur Theorie der Elektrolyte. *Phys. Zeitschrift*, 24(9):185, 1923.

J. L. Derissen. A reinvestigation of the molecular structure of acetic acid monomer and dimer by gas electron diffraction. *J. Mol. Struct.*, 7:67, 1971.

J.-C. Diels, E. V. Stryland, and G. Benedict. Generation and measurement of 200 femtosecond optical pulses. *Opt. Comm.*, 25:93, 1978.

V. G. Dmitriev, G. G. Gurzadyan, and D. N. Nikogosyan. *Handbook of nonlinear optical crystals.* Springer-Verlag, Berlin & Heidelberg, Germany, 2 edition, 1997.

J. Dreyer. Hydrogen-bonded acetic acid dimers: Anharmonic coupling and linear infrared spectra studied with density-functional theory. *J. Chem. Phys.*, 122:184306, 2005.

J. Dreyer. Unraveling the structure of hydrogen bond stretching mode infrared absorption bands: An anharmonic density functional theory study on 7-azaindole dimers. *J. Chem. Phys.*, 127:054309, 2007.

J. D. Dunitz, K. D. M. Harris, R. L. Johnston, B. M. Kariuki, E. J. MacLean, K. Psallidas, W. B. Schweizer, and R. R. Tykwinski. New light on an old story: The solid-state transformation of ammonium cyanate into urea. *J. Am. Chem. Soc.*, 120(50):13274, 1998.

G. Duvanel, N. Banerji, and E. Vauthey. Excited-state dynamics of donor-acceptor bridged systems containing a boron-dipyrromethene chromophore: Interplay between charge separation and reorientational motion. *J. Phys. Chem. A*, 111:5361, 2007.

J. E. W. Castner, D. Kennedy, and R. J. Cave. Solvent as electron donor: donor/acceptor electronic coupling is a dynamical variable. *J. Phys. Chem. A*, 104: 2869, 2000.

D. D. Eads, B. G. Dismer, and G. R. Fleming. A subpicosecond, subnanosecond and steady-state study of diffusion-influenced fluorescence quenching. *J. Chem. Phys.*, 93 (2):1136, 1990.

M. Eigen. Proton transfer, acid-base catalysis, and enzymatic hydrolysis. *Angew. Chem. Int. Ed.*, 3(1):1, 1964.

M. Eigen, K. Kustin, and G. Maass. Die Geschwindigkeit der Hydratation von SO_2 in wäßriger Lösung. *Z. Phys. Chem. N.F.*, 30:130, 1961.

M. Eigen, W. Kruse, and L. D. Maeyer. Rate constants of protolytic reactions in aqueous solution. *Prog. React. Kinet.*, 2:287, 1964.

A. Einstein. Über die von der molekularkinetischen Theorie der Wärme geforderte Bewegung von in ruhenden Flüssigkeiten suspendierten Teilchen. *Annalen der Physik*, 17:549, 1905.

A. Einstein. Zur Theorie der Brownschen Bewegung. *Annalen der Physik*, 19:371, 1906.

A. Einstein. Zur Quantentheorie der Strahlung. *Physik. Z.*, 18:121, 1917.

J. W. Ellms and J. C. Beneker. The estimation of carbonic acid in water. *J. Am. Chem. Soc.*, 23:405, 1901.

G. Estiu and K. M. Merz. Competitive hydrolytic and elimination mechanisms in the urease catalyzed decomposition of urea. *J. Phys. Chem. B*, 111(34):10263, 2007.

H. Eyring. The activated complex in chemical reactions. *J. Chem. Phys.*, 3:107, 1935.

A. Fick. Ueber Diffusion. *Annalen der Physik*, 170(1):59, 1855.

G. R. Fleming. *Chemical applications of ultrafast spectroscopy*, chapter 6: Relaxation processes in liquids and solutions. Oxford University Press, New York, 1986.

R. L. Fork, B. I. Greene, and C. V. Shank. Generation of optical pulses shorter than 0.1 psec by colliding pulse mode locking. *Appl. Phys. Lett.*, 38:674, 1981.

T. Förster. Fluoreszenzspektrum und Wasserstoffionenkonzentration. *Naturwissenschaften*, 36(6):186, 1949.

T. Förster. Elektrolytische Dissoziation angeregter Moleküle. *Z. Elektrochem.*, 54(1): 42, 1950.

T. Förster. Diabatic and adiabatic processes in photochemistry. *Pure & Appl.Chem.*, 24(3):443, 1970.

M. J. Frisch, G. W. Trucks, H. B. Schlegel, G. E. Scuseria, M. A. Robb, J. R. Cheeseman, V. G. Zakrzewski, J. A. Montgomery, R. E. Stratmann, J. C. Burant, S. Dapprich, J. M. Millam, A. D. Daniels, K. N. Kudin, M. C. Strain, O. Farkas, J. Tomasi, V. Barone, M. Cossi, R. Cammi, B. Mennucci, C. Pomelli, C. Adamo, S. Clifford, J. Ochterski, G. A. Petersson, P. Y. Ayala, Q. Cui, K. Morokuma, D. K. Malick, A. D. Rabuck, K. Raghavachari, J. B. Foresman, J. Cioslowski, J. V. Ortiz, B. B.

Stefanov, G. Liu, A. Liashenko, P. Piskorz, I. Komaromi, R. Gomperts, R. L. Martin, D. J. Fox, T. Keith, M. A. Al-Laham, C. Y. Peng, A. Nanayakkara, C. Gonzalez, M. Challacombe, P. M. W. Gill, B. G. Johnson, W. Chen, M. W. Wong, J. L. Andres, M. Head-Gordon, R. E. S., and J. A. Pople. *Gaussian 98 (Revision A.2)*. Gaussian, Inc., Pittsburgh PA, 1998.

Y. Fujii, H. Yamada, and M. Mizuta. Self-association of acetic acid in some organic solvents. *J. Phys. Chem.*, 92:6768, 1988.

R. M. Fuoss and C. A. Kraus. Properties of electrolytic solutions. III. The dissociation constant. *J. Am. Chem. Soc.*, 55:1019, 1933.

V. Ganesan, S. V. Rosokha, and J. K. Kochi. Isolation of the latent precursor complex in electron-transfer dynamics. Intermolecular association and self-exchange with acceptor anion radicals. *J. Am. Chem. Soc.*, 125:2559, 2003.

L. Genosar, B. Cohen, and D. Huppert. Ultrafast direct photoacid-base reaction. *J. Phys. Chem. A*, 104:6689, 2000.

P. A. Gerakines, M. H. Moore, and R. L. Hudson. Carbonic acid production in H_2O:CO_2 ices. *Astron. Astrophys.*, 357:793, 2000.

E. D. German and A. M. Kuznetsov. Dependence of the hydrogen kinetic isotope effect on the reaction free energy. *J. Chem. Soc., Faraday Trans. 1*, 77:397, 1981.

E. D. German, A. M. Kuznetsov, and R. R. Dogonadze. Theory of the kinetic isotope effect in proton transfer reactions in a polar medium. *J. Chem. Soc., Faraday II*, 76: 1128, 1980.

V. Gladkikh, A. I. Burshtein, S. V. Feskov, A. I. Ivanov, and E. Vauthey. Hot recombination of photogenerated ion pairs. *J. Chem. Phys.*, 123:244510, 2005.

J. L. Goodman and K. S. Peters. Picosecond decay dynamics of the trans-stilbene-olefin contact ion pair: Electron-transfer vs. ion-pair separation. *J. Am. Chem. Soc.*, 107: 6459, 1985.

J. P. Gordon, H. J. Zeiger, and C. H. Townes. Molecular microwave oscillator and new hyperfine structure in the microwave spectrum of NH_3. *Phys. Rev.*, 95:282, 1954.

I. R. Gould and S. Farid. Dynamics of bimolecular photoinduced electron-transfer reactions. *Acc. Chem. Res.*, 29:522, 1996.

I. R. Gould, R. H. Young, R. E. Moody, and S. Farid. Contact and solvent-separated geminate radical ion pairs in electron-transfer photochemistry. *J. Phys. Chem.*, 95: 2068, 1991.

D. M. Guldi and K.-D. Asmus. Electron transfer from C_{76} ($C_{2\nu}$‘) and C_{78} (D_2) to radical cations of various arenes: Evidence for the Marcus inverted region. *J. Am. Chem. Soc.*, 119:5744, 1997.

W. Hage, A. Hallbrucker, and E. Mayer. Carbonic acid: Synthesis by protonation of bicarbonate and FTIR spectroscopic characterization via a new cryogenic technique. *J. Am. Chem. Soc.*, 115:8427, 1993.

W. Hage, A. Hallbrucker, and E. Mayer. Metastable intermediates from glassy solutions Part 5: FTIR spectroscopic characterization of isolated α- and β-carbonic acid. *J. Mol. Struct.*, 408/409:527, 1997.

W. Hage, K. R. Liedl, A. Hallbrucker, and E. Mayer. Carbonic acid in the gas phase and its astrophysical relevance. *Science*, 279:1332, 1998.

P. Hamm. Coherent effects in femtosecond infrared spectroscopy. *Chem. Phys.*, 200: 415, 1995.

P. Hamm, S. M. Ohline, and W. Zinth. Vibrational cooling after ultrafast photoisomerization of azobenzene measured by femtosecond infrared spectroscopy. *J. Chem. Phys.*, 106(2):519, 1997.

N. C. Handy and A. Willetts. Anharmonic constants for benzene. *Spectrochim. Acta A*, 53:1169, 1997.

P. Hänggi, P. Talkner, and M. Borkovec. Reaction-rate theory: Fifty years after Kramers. *Rev. Mod. Phys.*, 62:251, 1990.

T. T. Harding and S. C. Wallwork. The structures of molecular compounds exhibiting polarization bonding. II. The crystal structure of the chloranil-hexamethylbenzene complex. *Acta Cryst.*, 8:787, 1955.

L. E. Hargrove, R. L. Fork, and M. A. Pollack. Locking of He-Ne laser modes induced by synchronous intracavity modulation. *Appl. Phys. Lett.*, 5(1):4, 1964.

J. M. Headrick, E. G. Diken, R. S. Walters, N. I. Hammer, R. A. Christie, J. Cui, E. M. Myshakin, M. A. Duncan, M. A. Johnson, and K. D. Jordan. Spectral signatures of hydrated proton vibrations in water clusters. *Science*, 308:1765, 2005.

H. Heitele. Dynamic solvent effects on electron-transfer reactions. *Angew. Chem. Int. Ed.*, 32:359, 1993.

A. Henseler and E. Vauthey. Determination of the free ion yield in photoinduced electron transfer processes using transient thermal phase grating spectroscopy. *J. Photochem. Photobiol. A*, 91:7, 1995.

R. H. Hertwig and W. Koch. On the parameterization of the local correlation functional. What is Becke-3-LYP? *Chem. Phys. Lett.*, 268:345, 1997.

G. Herzberg. *Molecular spectra and molecular structure*, volume II. Infrared and raman spectra of polyatomic molecules. Van Nostrand Reinhold Company, 1945.

G. Herzberg and C. Reid. Infrared spectrum and structure of the HNCO molecule. *Discuss. Faraday Soc.*, 9:92, 1950.

S. Hogiu, W. Werncke, M. Pfeiffer, J. Dreyer, and T. Elsaesser. Mode-specific vibrational excitation and energy redistribution after ultrafast intramolecular electron transfer. *J. Chem. Phys.*, 113(4):1587, 2000.

F. Holtzberg, B. Post, and I. Fankuchen. The crystal structure of formic acid. *Acta Cryst.*, 6:127, 1953.

J. T. Hynes, T. H. Tran-Thi, and G. Granucci. Intermolecular photochemical proton transfer in solution: New insights and perspectives. *J. Photochem. Photobiol. A*, 154: 3, 2002.

I. Ikemoto, K. Yakushi, and H. Kuroda. The refinement of the crystal structure of the perylene-tetracyanoethylene complex. *Acta Cryst.*, B26:800, 1970.

E. P. Ippen and C. V. Shank. Dynamic spectroscopy and subpicosecond pulse compression. *Appl. Phys. Lett.*, 27:488, 1975.

M. Iwaki, S. Kumazaki, K. Yoshihara, T. Erabi, and S. Itoh. ΔG^0 dependence of the electron transfer rate in the photosynthetic reaction center of plant photosystem I: Natural optimization of reaction between chlorophyll a (A_0) and quinone. *J. Phys. Chem.*, 100:10802, 1996.

M. E. Jacox and D. E. Milligan. Low-temperature infrared study of intermediates in the photolysis of HNCO and DNCO. *J. Chem. Phys.*, 40(9):2457, 1964.

N. D. Jones and R. E. Marsh. On the crystal structure of the chloranil-hexamethylbenzene complex. *Acta Cryst.*, 15:809, 1962.

R. E. Jones and D. H. Templeton. The crystal structure of acetic acid. *Acta Cryst.*, 11: 484, 1958.

R. A. Kaindl, M. Wurm, K. Reimann, P. Hamm, A. M. Weiner, and M. Woerner. Generation, shaping, and characterization of intense femtosecond pulses tunable from 3 to 20 μm. *J. Opt. Soc. Am. B*, 17:2086, 2000.

T. Kakitani, A. Yoshimori, and N. Mataga. Effects of the donor-acceptor distance distribution on the energy gap laws of charge separation and charge recombination reactions in polar solutions. *J. Phys. Chem.*, 96:5385, 1992.

T. Kakitani, N. Matsuda, A. Yoshimori, and N. Mataga. Present and future perspectives of theoretical aspects of photoinduced charge separation and charge recombination reactions in solution. *Prog. React. Kinet.*, 20:347, 1995.

J. Karle and L. O. Brockway. An electron diffraction investigation of the monomers and dimers of formic, acetic and trifluoroacetic acids and the dimer of deuterium acetate. *J. Am. Chem. Soc.*, 66:574, 1944.

P. A. Karplus, M. A. Pearson, and R. P. Hausinger. 70 years of crystalline urease: What have we learned? *Acc. Chem. Res.*, 30(8):330, 1997.

G. J. Kavarnos and N. J. Turro. Photosensitization by reversible electron transfer: Theories, experimental evidence, and examples. *Chem. Rev.*, 86:401, 1986.

M. S. Khatkale and J. P. Devlin. Infrared spectra of the di- and trianion salts of tetracyanoethylene. Assignments and vibronic effects. *J. Phys. Chem.*, 83(12):1636, 1979.

P. Kiefer and J. T. Hynes. *Theoretical aspects of proton transfer reactions in a polar environment*, volume 1 of *Physical and Chemical Aspects I-III*, chapter 10, pages 303–348. WILEY-VCH, Weinheim, 2007.

P. M. Kiefer and J. T. Hynes. *Proton transfer reactions and hydrogen bonding in solution*, volume 23 of *Understanding chemical reactivity*, chapter 4, pages 73–92. Kluwer Academic Publishers, Dordrecht, The Netherlands, 2002.

K. Kikuchi, T. Niwa, Y. Takahashi, H. Ikeda, T. Miyashi, and M. Hoshi. Evidence of exciplex formation in acetonitrile. *Chem. Phys. Lett.*, 173:421, 1990.

K. Kikuchi, Y. Takahashi, M. Hoshi, T. Niwa, T. Katagiri, and T. Miyashi. Free enthalpy dependence of free-radical yield of photoinduced electron transfer in acetonitrile. *J. Phys. Chem.*, 95:2378, 1991.

K. Kikuchi, T. Niwa, Y. Takahashi, H. Ikeda, and T. Miyashi. Quenching mechanism in a highly exothermic region of the Rehm-Weller relationship for electron-transfer fluorescence quenching. *J. Phys. Chem.*, 97:5070, 1993.

R. B. King, editor. *Encyclopedia of inorganic chemistry*, volume 10. Wiley, 2nd edition, 2005. Page 556.

R. Knochenmuss, I. Fischer, D. Luhrs, and Q. Lin. Intermolecular excited-state proton transfer in clusters of 1-naphthol with water and with ammonia. *Isr. J. Chem.*, 39 (3-4):221, 1999.

I. Kohl, K. Winkel, M. Bauer, K. R. Liedl, T. Loerting, and E. Mayer. Raman spectroscopic study of the phase transition of amorphous to crystalline β-carbonic acid. *Angew. Chem. Int. Ed.*, 48:2690, 2009.

E. M. Kosower and D. Huppert. Excited state electron and proton transfers. *Annu. Rev. Phys. Chem.*, 37:127, 1986.

V. Kozich, W. Werncke, J. Dreyer, K.-W. Brzezinka, M. Rini, A. Kummrow, and T. Elsaesser. Vibrational excitation and energy redistribution after ultrafast internal conversion in 4-nitroaniline. *J. Chem. Phys.*, 117(2):719, 2002.

V. Kozich, J. Dreyer, S. Ashihara, W. Werncke, and T. Elsaesser. Mode-selective O-H stretching relaxation in a hydrogen bond studied by ultrafast vibrational spectroscopy. *J. Chem. Phys.*, 125:074504, 2006.

V. Kozich, Ł. Szyc, E. T. J. Nibbering, W. Werncke, and T. Elsaesser. Ultrafast redistribution of vibrational energy after excitation of NH stretching modes in DNA oligomers. *Chem. Phys. Lett.*, 473:171, 2009.

I. Z. Kozma, P. Baum, S. Lochbrunner, and E. Riedle. Widely tunable sub-30 fs ultraviolet pulses by chirped sum frequency mixing. *Opt. Express*, 11:3110, 2003.

H. A. Kramers. Brownian motion in a field of force and the diffusion model of chemical reactions. *Physica*, 7(4):284, 1940.

K. Kulinowski, I. R. Gould, and A. B. Myers. Absorption, fluorescence, and resonance raman spectroscopy of the hexamethylbenzene/ tetracyanoethylene charge-transfer complex: Toward a self-consistent model. *J. Phys. Chem.*, 99:9017, 1995.

A. Kummrow, M. Wittmann, F. Tschirschwitz, G. Korn, and E. T. J. Nibbering. Femtosecond ultraviolet pulses generated using noncollinear optical parametric amplification and sum frequency mixing. *Appl. Phys. B*, 71:885, 2000.

M. G. Kuzmin. Exciplex mechanism of excited state electron transfer reactions in polar media. *J. Photochem. Photobiol. A*, 102:51, 1996.

A. M. Kuznetsov and J. Ulstrup. *Electron transfer in chemistry and biology.* Wiley Series in Theoretical Chemistry. John Wiley & Sons, 1999.

L. Landau. On the theory of transfer of energy at collisions II. *Phys. Z. Sowjetunion*, 2:46, 1932a.

L. Landau. On the theory of transfer of energy at collisions I. *Phys. Z. Sowjetunion*, 1: 88, 1932b.

W. M. Latimer and W. H. Rodebush. Polarity and ionization from the standpoint of the lewis theory of valence. *J. Am. Chem. Soc.*, 42:1419, 1920.

C. Lee and R. G. Yang, W. Parr. Development of the Colle-Salvetti correlation-energy formula into a functional of the electron density. *Phys. Rev. B*, 37:785, 1988.

J. Liebig and F. Wöhler. Untersuchungen über die Cyansäure. *Annalen der Physik und Chemie*, 96:369, 1830.

M. Lim, T. A. Jackson, and P. A. Anfinrud. Binding of CO to myoglobin from a heme pocket docking site to form nearly linear Fe-C-O. *Science*, 269:962, 1995.

T. Loerting, C. Tautermann, R. T. Kroemer, I. Kohl, A. Hallbrucker, E. Mayer, and K. R. Liedl. On the surprising kinetic stability of carbonic acid (H_2CO_3). *Angew. Chem. Int. Ed. Engl.*, 39(5):891, 2000.

K. R. Lynn. Kinetics of base-catalyzed hydrolysis of urea. *J. Phys. Chem.*, 69(2):687, 1965.

B. Z. Magnes, N. V. Strashnikova, and E. Pines. Evidence for L-1(a), L-1(b) dual state emission in 1-naphthol and 1-methoxynaphthalene fluorescence in liquid solutions. *Isr. J. Chem.*, 39(3-4):361, 1999.

T. H. Maiman. Stimulated optical radiation in ruby. *Nature*, 187:4736, 1960.

R. A. Marcus. Electrostatic free energy and other properties of states having nonequilibrium polarization. I. *J. Chem. Phys.*, 24(5):979, 1956a.

R. A. Marcus. On the theory of oxidation-reduction reactions involving electron transfer. I. *J. Chem. Phys.*, 24(5):966, 1956b.

R. A. Marcus. On the theory of oxidation-reduction reactions involving electron transfer. II. Applications to data on the rates of isotopic exchange reactions. *J. Chem. Phys.*, 26(4):867, 1957a.

R. A. Marcus. On the theory of oxidation-reduction reactions involving electron transfer. III. Applications to data on the rates of organic redox reactions. *J. Chem. Phys.*, 26 (4):872, 1957b.

R. A. Marcus. Theoretical relations among rate constants, barriers, and Brønsted slopes of chemical reactions. *J. Phys. Chem.*, 72(3):891, 1968.

R. A. Marcus. Energetic and dynamical aspects of proton transfer reactions in solution. *Faraday Symp. Chem. Soc.*, 10:60, 1975.

R. A. Marcus. Electron, proton and related transfers. *Faraday Discuss. Chem. Soc.*, 74: 7, 1982.

R. A. Marcus and N. Sutin. Electron transfers in chemistry and biology. *Biochim. Biophys. Acta*, 811:265, 1985.

J. M. G. Martinho, J. P. Farinha, M. N. Berberan-Santos, J. Duhamel, and M. A. Winnik. Test of a model for reversible excimer kinetics: Pyrene in cyclohexanol. *J. Chem. Phys.*, 96(11):8143, 1992.

D. Marx, M. E. Tuckerman, J. Hutter, and M. Parrinello. The nature of the hydrated excess proton in water. *Nature*, 397:601, 1999.

J. M. Masnovi and J. K. Kochi. Direct observation of ion-pair dynamics. *J. Am. Chem. Soc.*, 107:7880, 1985.

N. Mataga, T. Asahi, Y. Kanda, T. Okada, and T. Kakitani. The bell-shaped energy gap dependence of the charge recombination reaction of geminate radical ion pairs produced by fluorescence quenching reaction in acetonitrile solution. *Chem. Phys.*, 127:249, 1988.

N. Mataga, H. Chosrowjan, and S. Taniguchi. Ultrafast charge transfer in excited electronic states and investigations into fundamental problems of exciplex chemistry: Our early studies and recent developments. *J. Photochem. Photobiol. C*, 6:37, 2005.

F. J. McClung and R. W. Hellwarth. Giant optical pulsations from ruby. *J. Appl. Phys.*, 33:828, 1962.

G. E. McManis, A. Gochev, and M. J. Weaver. Solvent dynamical effects in electron transfer: The solvent inertial limit and the predicted influence of quantum effects. *Chem. Phys.*, 152:107, 1991.

B. Miehlich, A. Savin, H. Stoll, and H. Preuss. Results obtained with the correlation energy density functionals of Becke and Lee, Yang and Parr. *Chem. Phys. Lett.*, 157: 200, 1989.

J. R. Miller. Intermolecular electron transfer by quantum mechanical tunneling. *Science*, 189:221, 1975.

J. R. Miller. Intramolecular long-distance electron transfer in radical anions. The effects of free energy and solvent on the reaction rates. *J. Am. Chem. Soc.*, 106:3047, 1984.

J. S. Miller. Tetracyanoethylene (TCNE): The characteristic geometries and vibrational absorptions of its numerous structures. *Angew. Chem. Int. Ed.*, 45:2508, 2006.

F. J. Millero and R. N. Roy. A chemical equilibrium model for the carbonate system in natural waters. *Croatia Chem. Acta*, 70:1, 1997.

M. Mladenović and M. Lewerenz. Equilibrium structure and energetics of CHNO isomers: Steps towards ab initio rovibrational spectra of quasi-linear molecules. *Chem. Phys.*, 343:129, 2008.

O. F. Mohammed and E. Vauthey. Simultaneous generation of different types of ion pairs upon charge-transfer excitation of a donor-acceptor complex revealed by ultrafast transient absorption spectroscopy. *J. Phys. Chem. A*, 112:5804, 2008.

O. F. Mohammed, J. Dreyer, B.-Z. Magnes, E. Pines, and E. T. J. Nibbering. Solvent-dependent photoacidity state of pyranine monitored by transient mid-infrared spectroscopy. *ChemPhysChem*, 6:625, 2005a.

O. F. Mohammed, D. Pines, J. Dreyer, E. Pines, and E. T. J. Nibbering. Sequential proton transfer through water bridges in acid-base reactions. *Science*, 310:83, 2005b.

O. F. Mohammed, N. Banerji, B. Lang, E. T. J. Nibbering, and E. Vauthey. Photoinduced bimolecular electron transfer investigated by femtosecond time-resolved infrared spectroscopy. *J. Phys. Chem. A*, 110:13676, 2006.

O. F. Mohammed, D. Pines, E. T. J. Nibbering, and E. Pines. Base-induced solvent switches in acid-base reactions. *Angew. Chem. Int. Ed.*, 46:1458, 2007a.

O. F. Mohammed, D. Pines, E. Pines, and E. T. J. Nibbering. Aqueous bimolecular proton transfer in acid-base neutralization. *Chem. Phys.*, 341:240, 2007b.

O. F. Mohammed, K. Adamczyk, N. Banerji, J. Dreyer, B. Lang, E. T. J. Nibbering, and E. Vauthey. Direct femtosecond observation of tight and loose ion pairs upon photoinduced bimolecular electron transfer. *Angew. Chem. Int. Ed.*, 47:9044, 2008.

O. F. Mohammed, K. Adamczyk, N. Banerji, J. Dreyer, B. Lang, E. T. J. Nibbering, and E. Vauthey. Direct femtosecond observation of tight and loose ion pairs upon photoinduced bimolecular electron transfer. In P. Corkum, S. D. Silvestri, K. A. Nelson, E. Riedle, and R. W. Schoenlein, editors, *Ultrafast Phenomena XVI*, volume 92 of *Springer Ser. Chem. Phys.*, pages 613–615, Berlin & Heidelberg, Germany, 2009a. Springer-Verlag.

O. F. Mohammed, K. Adamczyk, D. Pines, E. Pines, and E. T. J. Nibbering. Aqueous proton transfer pathways in bimolecular acid-base neutralization. In P. Corkum, S. D. Silvestri, K. A. Nelson, E. Riedle, and R. W. Schoenlein, editors, *Ultrafast Phenomena XVI*, volume 92 of *Springer Ser. Chem. Phys.*, pages 622–624, Berlin & Heidelberg, Germany, 2009b. Springer-Verlag.

M. H. Moore and R. K. Khanna. Infrared and mass spectral studies of proton irradiated $H_2O + CO_2$ ice: Evidence for carbonic acid. *Spectrochim. Acta*, 47A(2):255, 1991.

A. Morandeira, L. Engeli, and E. Vauthey. Ultrafast charge recombination of photogenerated ion pairs to an electronic excited state. *J. Phys. Chem. A*, 106:4833, 2002.

A. Morandeira, A. Fürstenberg, J.-C. Gumy, and E. Vauthey. Fluorescence quenching in electron-donating solvents. 1. Influence of the solute-solvent interactions on the dynamics. *J. Phys. Chem. A*, 107:5375, 2003.

P. F. Moulton. Spectroscopic and laser characteristics of Ti:Al_2O_3. *J. Opt. Soc. Am. B*, 3:125, 1986.

S. Mukamel. *Principles of nonlinear optical spectroscopy.* Oxford University Press, New York, U.S.A., 1995. chapter 8.

P.-A. Muller, C. Högemann, X. Allonas, P. Jacques, and E. Vauthey. Deuterium isotope effect on the charge recombination dynamics of contact ion pairs formed by electron-transfer quenching in acetonitrile. *Chem. Phys. Lett.*, 326:321, 2000.

I. Nahringbauer. Hydrogen-bond studies .39. Reinvestigation of crystal structure of acetic acid (at +5°C and -190°C). *Acta Chem. Scand.*, 24:453, 1970.

J. Nelson. Hydrogen-bonded complexes of iso-cyanic acid: Infrared spectra and thermodynamic measurements. *Spectrochim. Acta*, 26A:109, 1970.

T. L. Nemzek and W. R. Ware. Kinetics of diffusion-controlled reactions: Transient effects in fluorescence quenching. *J. Chem. Phys.*, 62(2):477, 1975.

E. T. J. Nibbering. Principles of nonlinear spectroscopy. *Ph.D. student lecture at the Max-Born-Institute*, 2005.

E. T. J. Nibbering, H. Fidder, and E. Pines. Ultrafast chemistry: Using time-resolved vibrational spectroscopy for interrogation of structural dynamics. *Annu. Rev. Phys. Chem.*, 56:337, 2005.

O. Nicolet and E. Vauthey. Ultrafast nonequilibrium charge recombination dynamics of excited donor-acceptor complexes. *J. Phys. Chem. A*, 106:5553, 2002.

O. Nicolet and E. Vauthey. Heavy atom effect on the charge recombination dynamics of photogenerated geminate ion pairs. *J. Phys. Chem. A*, 107:5894, 2003.

O. Nicolet, N. Banerji, S. Pagés, and E. Vauthey. Effect of the excitation wavelength on the ultrafast charge recombination dynamics of donor-acceptor complexes in polar solvents. *J. Phys. Chem. A*, 109:8236, 2005.

H. H. Nielsen. The vibration-rotation energies of molecules. *Rev. Mod. Phys.*, 23(2):90, 1951.

S. Nishikawa, T. Asahi, T. Okada, N. Mataga, and T. Kakitani. Determination of the bimolecular rate constant of photoinduced charge separation in the energy gap region where the reaction is diffusion controlled - analysis of the transient effect in the course of fluorescence quenching reaction. *Chem. Phys. Lett.*, 185:237, 1991.

R. M. Noyes. Effects of diffusion rates on chemical kinetics. *Prog. React. Kinet.*, 1:129, 1961.

R. K. Pachauri and A. Reisinger, editors. *Climate change 2007 synthesis report - Contribution of working groups I, II and III to the fourth assessment report of the intergovernmental panel on climate change.* IPCC, 2007.

S. Pagés, B. Lang, and E. Vauthey. Ultrafast spectroscopic investigation of the charge recombination dynamics of ion pairs formed upon highly exergonic bimolecular electron-transfer quenching: Looking for the normal region. *J. Phys. Chem. A*, 108:549, 2004.

A. N. Pankratov and S. S. Khmelev. Acidity of HOCN, HSCN, HNCO, HNCS: A treatment from the viewpoint of ab initio approach. *J. Serb. Chem. Soc.*, 70(10): 1183, 2005a.

A. N. Pankratov and S. S. Khmelev. Protolytic properties of cyanic and thiocyanic acids and their isoforms. *J. Struct. Chem.*, 46(3):404, 2005b.

H. S. Park, Y. M. Jung, J. K. You, W. H. Hong, and J.-N. Kim. Analysis of the CO_2 and NH_3 reaction in an aqueous solution by 2D IR COS: Formation of bicarbonate and carbamate. *J. Phys. Chem. A.*, 112(29):6558, 2008.

J. Y. Park and D. E. Woon. Theoretical investigation of OCN-charge-transfer complexes in condensed-phase media: Spectroscopic properties in amorphous ice. *J. Phys. Chem. A.*, 108(31):6589, 2004.

L. Pauling. The shared-electron chemical bond. *Proc. Natl. Acad. Sci. USA*, 14:359, 1928.

L. Pauling and L. O. Brockway. The structure of the carboxyl group. II. The crystal structure of basic beryllium acetate by the diffraction of electrons. *Proc. Natl. Acad. Sci. USA*, 20:340, 1934.

K. S. Peters and J. Lee. Role of contact and solvent-separated radical ion pairs in the diffusional quenching of trans-stilbene excited singlet state by fumaronitrile. *J. Phys. Chem.*, 96:8941, 1992.

D. Pines and E. Pines. *Solvent assisted photoacidity*, volume 1 of *Physical and Chemical Aspects I-III*, chapter 12, pages 377–415. WILEY-VCH, Weinheim, 2007.

E. Pines. *Isotope effects in chemistry and biology*, page 451. CRC Taylor & Francis, Boca Raton, 2006.

E. Pines and G. R. Fleming. Proton transfer in mixed water-organic solvent solutions: Correlation between rate, equilibrium constant, and the proton free energy of transfer. *J. Phys. Chem.*, 95:10448, 1991.

E. Pines and D. Huppert. Observation of geminate recombination in excited state proton transfer. *J. Chem. Phys.*, 84(6):3576, 1986.

E. Pines and D. Huppert. Salt effect in photoacid quantum yield measurements: A demonstration of the geminate recombination role in deprotonation reactions. *J. Am. Chem. Soc.*, 111(11):4096, 1989.

E. Pines and D. Pines. *Proton dissociation and solute-solvent interactions following electronic excitation of photoacids.*, volume 23 of *Understanding chemical reactivity*, chapter 7, pages 155–184. Kluwer Academic Publishers, Dordrecht, The Netherlands, 2002.

E. Pines, D. Huppert, and N. Agmon. Geminate recombination in excited-state proton transfer reactions: Numerical solution of the Debye-Smoluchowski equation with backreaction and comparison with experimental results. *J. Chem. Phys.*, 88(9):5620, 1988.

E. Pines, D. Huppert, and N. Agmon. Salt effects on steady-state quantum yields of ultrafast, diffusion-influenced, reversible photoacid dissociation reactions. *J. Phys. Chem.*, 95:666, 1991.

E. Pines, B. Z. Magnes, M. J. Lang, and G. R. Fleming. Direct measurement of intrinsic proton transfer rates in diffusion-controlled reactions. *Chem. Phys. Lett.*, 281:413, 1997.

N. Pinnavaia, M. J. Bramley, M.-D. Su, W. H. Green, and N. C. Handy. A study of the ground electronic state of the isomers of CHNO. *Mol. Phys.*, 78(2):319, 1993.

Y. Pocker and D. W. Bjorkquist. Stopped-flow studies of carbon dioxide hydration and bicarbonate dehydration in H_2O and D_2O. Acid-base and metal ion catalysis. *J. Am. Chem. Soc.*, 99:6537, 1977.

B. Proctor, E. Westwig, and F. Wise. Characterization of a Kerr-lens mode-locked Ti:sapphire laser with positive group-velocity dispersion. *Opt. Lett.*, 18:1654, 1993.

B. R. Ramachandran, A. M. Halpern, and E. D. Glendening. Kinetics and mechanism of the reversible dissociation of ammonium carbamate: Involvement of carbamic acid. *J. Phys. Chem. A.*, 102(22):3934, 1998.

V. Ramanathan. The greenhouse theory of climate change: A test by an inadvertent global experiment. *Science*, 240:293, 1988.

S. Raunier, T. Chiavassa, A. Allouche, F. Marinelli, and J. P. Aycard. Thermal reactivity of HNCO with water ice: An infrared and theoretical study. *Chem. Phys.*, 288:197, 2003a.

S. Raunier, T. Chiavassa, F. Marinelli, A. Allouche, and J. P. Aycard. Reactivity of HNCO with NH_3 at low temperature monitored by FTIR spectroscopy: Formation of $NH_4^+OCN^-$. *Chem. Phys. Lett.*, 368:594, 2003b.

S. Raunier, T. Chiavassa, F. Marinelli, A. Allouche, and J. P. Aycard. An infrared and theoretical study about the “ XCN ” band formation: Reactivity of HNCO with NH_3 astrophysical ice laboratory analogues and the spontaneous production of OCN^-. *J. Phys. Chem. A*, 107(44):9335, 2003c.

S. Raunier, T. Chiavassa, F. Marinelli, and J. P. Aycard. Experimental and theoretical study on the spontaneous formation of OCN^- ion: Reactivity between HNCO and NH_3/H_2O environment at low temperature. *Chem. Phys.*, 302:259, 2004.

D. Rehm and A. Weller. Kinetics of fluorescence quenching by electron and H-atom transfer. *Isr. J. Chem.*, 8:259, 1970.

S. A. Rice. *Diffusion-limited reactions*, volume 25 of *Comprehensive Chemical Kinetics*. Elsevier, Amsterdam, Oxford, New York, Tokyo, 1985.

M. Rini. *Femtosecond mid-infrared spectroscopy of elementary photoinduced reactions*. PhD thesis, Humboldt-Universität zu Berlin, 2005.

M. Rini, B. Z. Magnes, E. Pines, and E. T. J. Nibbering. Real-time observation of bimodal proton transfer in acid-base pairs in water. *Science*, 301(5631):349, 2003.

M. Rini, D. Pines, B. Z. Magnes, E. Pines, and E. T. J. Nibbering. Bimodal proton transfer in acid-base reactions in water. *J. Chem. Phys.*, 121(19):9593, 2004.

R. A. Robinson and R. H. Stokes. *Electrolyte solutions*. Butterworths Scientific Publications, London, U.K., 2nd edition, 1959. Chapter 4.

W. Schneider and W. Thiel. Anharmonic force fields from analytic second order derivatives: Method and application to methyl bromide. *Chem. Phys. Lett.*, 157:367, 1989.

W. A. Schutte and R. K. Khanna. Origin of the 6.85μm band near young stellar objects: The ammonium ion (NH_4^+) revisited. *Astron. Astrophys.*, 398:1049, 2003.

M. S. Schuurman, S. R. Muir, W. D. Allen, and H. F. Schaefer III. Toward subchemical accuracy in computational thermochemistry: Focal point analysis of the heat of formation of NCO and [H,N,C,O] isomers. *J. Chem. Phys.*, 120(24):11586, 2004.

C. F. Shannon and D. D. Eads. Diffusion-controlled electron transfer reactions: Subpicosecond fluorescence measurements of coumarin 1 quenched by aniline and N,N-dimethylaniline. *J. Chem. Phys.*, 103(13):5208, 1995.

Y. R. Shen. *The principles of nonlinear optics*. John Wiley & Sons, New York, USA, 1984.

T. Shida. *Electronic absorption spectra of radical ions*. Number 34 in physical sciences data. Elsevier, Amsterdam, 1988.

M. Sikorski, E. Krystkowiak, and R. P. Steer. The kinetics of fast fluorescence quenching processes. *J. Photochem. Photobiol. A*, 117:1, 1998.

D. N. Silverman. Marcus rate theory applied to enzymatic proton transfer. *Biochim. Biophys. Acta*, 1458:88, 2000.

B. J. Siwick and H. J. Bakker. On the role of water in intermolecular proton-transfer reactions. *J. Am. Chem. Soc.*, 129:13412, 2007.

B. J. Siwick, M. J. Cox, and H. J. Bakker. Long-range proton transfer in aqueous acid-base reactions. *J. Phys. Chem. B*, 112:378, 2008.

K. M. Solntsev, D. Huppert, and N. Agmon. Challenge in accurate measurement of fast reversible bimolecular reaction. *J. Phys. Chem. A*, 105(24):5868, 2001.

D. E. Spence, P. N. Kean, and W. Sibbet. 60-fsec pulse generation from a self-mode-locked Ti:sapphire laser. *Opt. Lett.*, 16:42, 1991.

D. B. Spry and M. D. Fayer. Charge redistribution and photoacidity: Neutral versus cationic photoacids. *J. Chem. Phys.*, 128:084508, 2008.

G. G. Stokes. On the friction of fluid in motion and the equilibrium and motion of elastic solids. *Philos. Trans. Cambridge Soc.*, 8:297, 1849.

D. Strickland and G. Mourou. Compression of amplified chirped optical pulses. *Opt. Comm.*, 56:219, 1985.

A. Szabo. Theory of diffusion-influenced fluorescence quenching. *J. Phys. Chem*, 93: 6929–6939, 1989.

M. Tachiya and S. Murata. New explanation for the lack of the inverted region in charge separation reactions. *J. Phys. Chem.*, 96:8441, 1992.

J. H. Teles, G. Maier, J. B. A. Hess, L. J. Schaad, M. Winnewisser, and B. P. Winnewisser. The CHNO isomers. *Chem. Ber.*, 122:753, 1989.

J. K. Terlouw, C. B. Lebrilla, and H. Schwarz. Thermolysis of NH_4HCO_3 - A simple route to the formation of free carbonic acid (H_2CO_3) in the gas phase. *Angew. Chem. Int. Ed. Engl.*, 26:354, 1987.

H.-J. Teuteberg. *Geschichte des Konsums.* Franz Steiner Verlag, 2003.

S. J. M. Thomas, P. P. Edwards, and V. L. Kuznetsov. Sir Humphrey Davy: Boundless chemist, physicist, poet and man of action. *ChemPhysChem*, 9:59, 2008.

J. A. Tossell. H_2CO_3 and its oligomers: Structures, stabilities, vibrational and NMR spectra, and acidities. *Inorg. Chem.*, 45:5961, 2006.

T. H. Tran-Thi, T. Gustavsson, C. Prayer, S. Pommeret, and J. T. Hynes. Primary ultrafast events preceding the photoinduced proton transfer from pyranine to water. *Chem. Phys. Lett.*, 329:421, 2000.

T. H. Tran-Thi, C. Prayer, P. H. Millié, P. Uznanski, and J. T. Hynes. Substituent and solvent effects on the nature of the transitions of pyrenol and pyranine. Identification of an intermediate in the excited-state proton transfer reaction. *J. Phys. Chem. A*, 106:2244, 2002.

C. A. Tsipis and P. A. Karipidis. Mechanism of a chemical classic: Quantum chemical investigation of the autocatalyzed reaction of the serendipitous Wöhler synthesis of urea. *J. Am. Chem. Soc.*, 125(8):2307, 2003.

C. E. Vanderzee and R. A. Myers. Thermochemistry of the acid hydrolysis of potassium cyanate. *J. Phys. Chem.*, 65(1):153, 1961.

P. Vanysek. *Ionic conductivity and diffusion at infinite dilution.* CRC Handbook of Chemistry and Physics. CRC Press, Boca Raton, 2002.

E. Vauthey. Effect of steric hindrance on the dynamics of charge recombination within geminate ion pairs. *J. Phys. Chem. A*, 104:1804, 2000.

E. Vauthey. Direct measurements of the charge-recombination dynamics of geminate ion pairs formed upon electron-transfer quenching at high donor concentration. *J. Phys. Chem. A*, 105:340, 2001.

E. Vauthey. Investigations of bimolecular photoinduced electron transfer reactions in polar solvents using ultrafast spectroscopy. *J. Photochem. Photobiol. A*, 179:1, 2006.

E. Vauthey, P. Suppan, and E. Haselbach. Free-energy dependence of the ion yield of photo-induced electron-transfer reactions in solution. *Helv. Chim. Acta*, 71:93, 1988.

E. Vauthey, D. Pilloud, E. Haselbach, P. Suppan, and P. Jacques. The reliability of free ion yield in photoinduced electron transfer reactions. The model system 9,10-dicyanoanthracene/biphenyl in acetonitrile. *Chem. Phys. Lett.*, 215:264, 1993.

M. von Raumer, P. Suppan, and P. Jacques. Photoinduced charge transfer processes of triplet benzophenone in acetonitrile. *J. Photochem. Photobiol. A*, 105:21, 1997.

M. von Smoluchowski. Versuch einer mathematischen Theorie der Koagulationskinetik kolloider Lösungen. *Z. Phys. Chem.*, 92:129, 1917.

M. R. Wasielewski, M. P. Niemczyk, W. A. Svec, and E. B. Pewitt. Dependence of rate constants for photoinduced charge separation and dark charge recombination on the free energy of reaction in restricted-distance porphyrin-quinone molecules. *J. Am. Chem. Soc.*, 107:1080, 1985.

A. Weller. Protolytische Reaktionen angeregter Oxyverbindungen. *Z. Phys. Chem. (Leipzig)*, 17:224, 1958.

A. Weller. Fast reactions of excited molecules. *Prog. React. Kinet.*, 1:187, 1961.

A. Weller. Exciplex and radical pairs in photochemical electron transfer. *Pure & Appl.Chem.*, 54(10):1885, 1982.

C. A. Wight and A. I. Boldyrev. Potential energy surface and vibrational frequencies of carbonic acid. *J. Phys. Chem.*, 99:12125, 1995.

G. Wilemski and M. Fixman. General theory of diffusion-controlled reactions. *J. Chem. Phys.*, 58(9):4009, 1973.

T. Wilhelm, J. Piel, and E. Riedle. Sub-20-fs pulses tunable across the visible from a blue-pumped single-pass noncollinear parametric converter. *Opt. Lett.*, 22:1494, 1997.

A. Willetts and N. C. Handy. The anharmonic constants for a symmetric top. *Chem. Phys. Lett.*, 235:286, 1995.

K. Winkel, W. Hage, T. Loerting, S. L. Price, and E. Mayer. Carbonic acid: From polyamorphism to polymorphism. *J. Am. Chem. Soc.*, 129:13863, 2007.

S. Winstein, E. Clippinger, A. H. Fainberg, and G. C. Robinson. Salt effects and ion-pairs in solvolysis. *J. Am. Chem. Soc.*, 76:2597, 1954.

K. F. Wissbrun, D. M. French, and A. Patterson, Jr. The true ionization constant of carbonic acid in aqueous solution from 5 to 45°. *J. Phys. Chem.*, 58:693, 1954.

F. Wöhler. Ueber künstliche Bildung des Harnstoffs. *Annalen der Physik und Chemie*, 87:253, 1828.

C. Zener. Non-adiabatic crossing of energy levels. *Proc. R. Soc. London A*, 137:696, 1932.

C. Zener. Dissociation of excited diatomic molecules by external perturbations. *Proc. R. Soc. London A*, 140:660, 1933.

C. Zhong, J. Zhou, and C. L. Braun. Solvent-separated radical ion pairs and free ion yields. 1. Effect of temperature on free ion formation in solution. *J. Phys. Chem. A*, 108:6842, 2004.

J. Zhou, R. P. Shah, B. R. Findley, and C. L. Braun. Long distance photoinduced electron transfer in solutions: A mechanism for producing large yields of free ions by electron transfer quenching. *J. Phys. Chem. A*, 106:12, 2002.

List of Figures

List of Tables

Selbständigkeitserklärung

Hiermit erkläre ich, die Dissertation selbständig und nur unter Verwendung der angegebenen Hilfen und Hilfsmittel angefertigt zu haben.

Ich habe mich anderweitig nicht um einen Doktorgrad beworben und besitze keinen entsprechenden Doktorgrad.

Ich erkläre die Kenntnisnahme der dem Verfahren zugrunde liegenden Promotionsordnung der Mathematisch-Naturwissenschaftlichen Fakultät I der Humboldt-Universität zu Berlin.

Berlin, den 26.10.2009 Katrin Adamczyk